Development of Liquid Scintillator for A Large Size Neutrino Detector

Master thesis

by

TAJIMA Osamu
Department of Physics, Tohoku University
Sendai 980-8578, Japan

Jan 25, 2000

Contents

Chapter 1

Introduction

1.1 Present Status of Neutrino Mass

Discovery of Neutrino Oscillation

In 1998, $\nu_\mu \rightarrow \nu_\tau$ oscillation[1] was reported by the Super-Kamiokande group[16, 21]. Neutrino oscillation is the phenomenon that neutrino flavor changes to another flavor with time propagation because the flavor eigenstates and mass eigenstates are no identical (Section 1.2). This phenomenon cannot be observed if neutrino masses are 0. Neutrino oscillation is characterized by two parameters, $\sin^2 2\theta$ and Δm^2, if neutrino flavors mixed between two generation. $\sin^2 2\theta$ is the intensity of the mixing between two flavors, and $\Delta m^2 \left(= |m^2_{\nu_1} - m^2_{\nu_2}|\right)$ is the mass square difference between different flavor neutrinos. The result of Super-Kamiokande group is shown in Figure 1.1, Δm^2 is $\sim 3 \times 10^{-3}\mathrm{eV}^2$ and $\sin^2 2\theta$ is about 1. This result denotes that **neutrinos have small masses and their masses are different among three generations**.

Neutrino Mass in the Standard Model [25, 24]

The standard model, which is the theory of elementary particles and of their interactions, explains almost all of the experimental results at present. Neutrino masses are treated as 0 in this model. The helisity of the massive particle is able to inverse because the velocity of the massive particle is less than c(light velocity). So, there must be right-handed neutrino($\nu_{_R}$) if neutrino masses are not 0. The right-handed particle doesn't have $\mathrm{SU}(2)_L$ interaction, that is the same for $\nu_{_R}$. Moreover, the hyper charge of $\nu_{_R}$ is 0 from Q=I_3+Y because the charge(Q) and the iso-spin(I_3) is 0, so that $\nu_{_R}$ doesn't have $\mathrm{U}(1)_\mathrm{Y}$ interaction. To sum up, $\nu_{_R}$ is the sterile particle which cannot be detected, and neutrino masses are treated as 0 for simplicity in the standard model. Therefore, **there is no theoretical derivation that neutrino masses have to be 0 and**

[1] $\nu_\mu \rightarrow \nu_s$ oscillation was disfavored in [21].

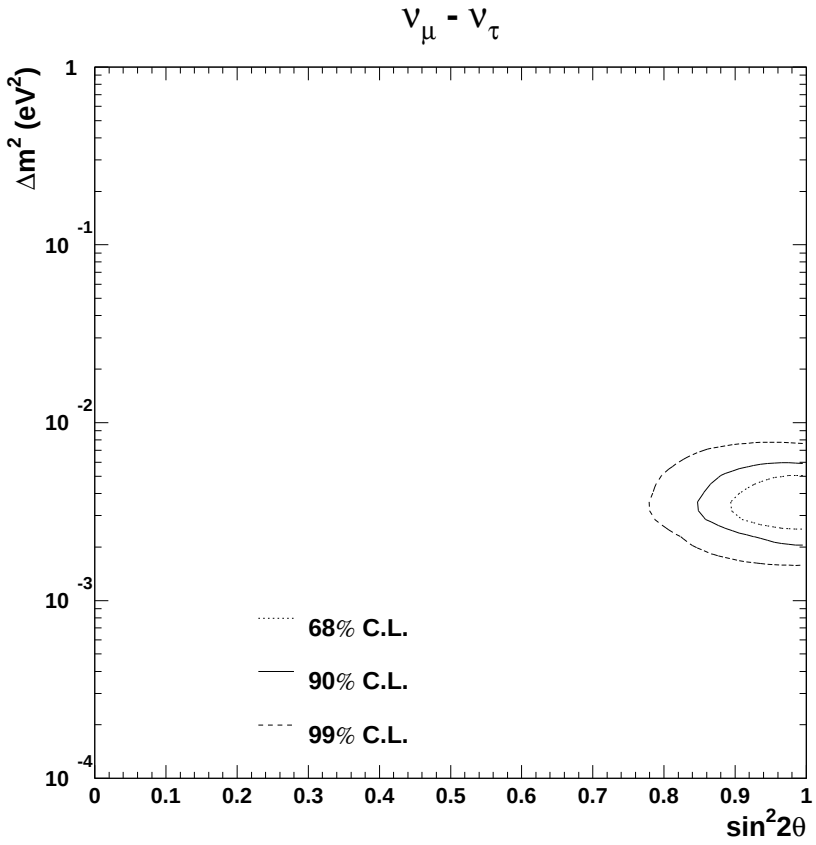

Figure 1.1: The 68%, 90% and 99% confidence intervals of $\nu_\mu \to \nu_\tau$ oscillation obtained by Super-Kamiokande are shown for $\sin^2 2\theta$ and Δm^2 parameter space.

the existence of ν_R. For example, $L \sim g\bar{\nu_L}\nu_R\phi$ type interaction is permitted in the $SU(2)_L \times U(1)_Y$ gauge theory, here ϕ is the Higgs field and g is the coupling constant. It is the same reason particle, u-quark, d-quark, $\cdots$, have mass. The meaning ν_R exists and the meaning neutrino mass is not 0 is same. The strength of this interaction is proportional to the mass of the individual particle because it is mediated by the higgs particle. Therefore, it is very difficult to know which ν_R is exist or not when ν_R mass is very small. This imply that **neutrinos are able to have very small mass in the standard model**(Figure 1.2-(a)). But, it is impossible to explain why neutrino masses are very small compared with other lepton or quark within the limits of the standard model. In other words, there is a possibility that the discovery of the neutrino mass is the discovery of the phenomenon beyond the standard model.

Is Massive neutrino Dirac-Neutrino or Majorana-Neutrino ?

Following to above lines, the existence of Dirac-neutrino is allowed in the standard model although there is a problem why neutrino masses are very small. The mechanism that this type neutrinos have masses are shown in Figure 1.2-(a).

On the other hand, there is some possibility that neutrinos are Majorana-neutrino because neutrinos do not have charge. Majorana-particle is the particle that there is no difference between particle and anti-particle. The existence of massive Majorana-neutrino means beyond standard model, the reason is written in follow lines.

It is assumed that Majorana-neutrino is only left-handed[24], this neutrino cannot interact with the normal higgs particle(iso-spin 1/2) in the standard model. So, there must be the another higgs particle whose iso-spin is 1(Figure 1.2-(b)) or the another charged particle whose iso-spin is 1(Figure 1.2-(c)) if neutrinos have masses. Here, iso-spin 1 charged particle violates the lepton flavor conservation and iso-spin 1 higgs particle does not exist in the standard model.

Moreover, assuming that Majorana-neutrino are left-handed and right-handed, sea-saw mechanism model[34, 23, 24, 36] explain that neutrinos has very small mass(Figure 1.2-(d)). In this model, the relation of the masses of left-hand neutrino(m_{ν_L}), right-hand neutrino(m_{ν_R}) and lepton(m_l) is;

$$m_{\nu_L} \cdot m_{\nu_R} = m_l^2$$

m_{ν_L} can be very small if m_{ν_R} is very big $\sim 10^{16}$GeV[36], this is beyond the standard model scale, although iso-spin 1 higgs etc. are not needed in this model.

As the mentioned above, the explanation why neutrinos have small masses is much more easy if neutrinos are Majorana-neutrinos than if neutrinos are Dirac-neutrinos. In either case, the discovery of lepton flavor violation or double beta decay or the exclusion them are needed to decide the type of neutrinos.

Upper Limits of Neutrino Mass

Currently, direct neutrino mass measurement only give upper limits as following;

$$\begin{aligned} m(\nu_e) &< \sim 2.5\text{eV } [13,\ 5] \\ m(\nu_\mu) &< 170\text{keV } [9] \\ m(\nu_\tau) &< 18.2\text{MeV } [17] \end{aligned}$$

Recently, the cosmology also suggest upper limits for all neutrino flavors because neutrino as dark matter does not need[12].

$$\begin{aligned} m(\nu_j) &\leq 0.9\text{eV } [12] \\ \Sigma m(\nu_j) &\leq 8\text{eV } [14] \end{aligned}$$

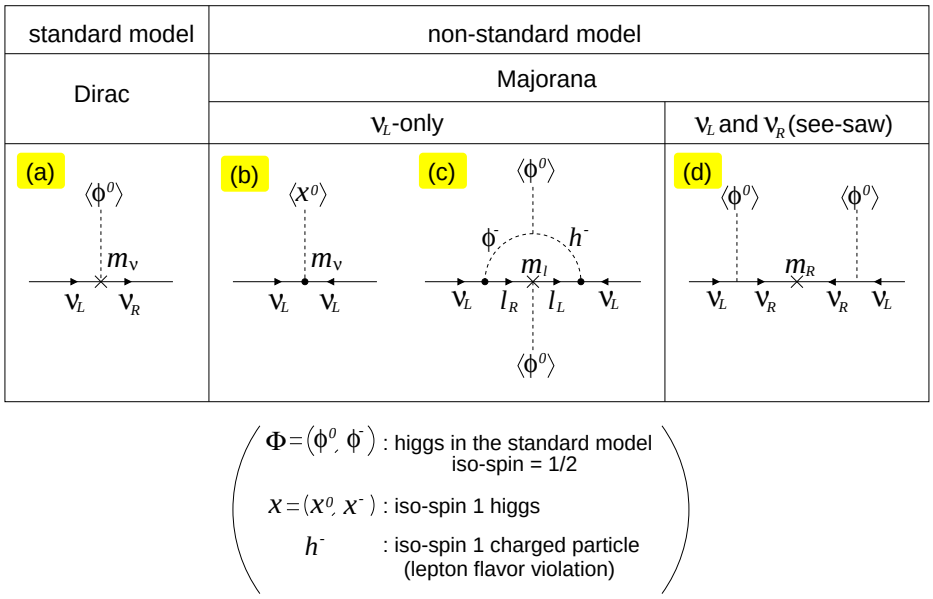

Figure 1.2: Mechanisms that neutrinos have masses are shown in. (a) denotes that Dirac-neutrinos coupled with higgs particle(ϕ^0) and have masses. There must be iso-spin 1 higgs particle(χ^0) or iso-spin 1 charged particle(h^-) because only left-handed Majorana-neutrinos have masses. Those interactions are shown in (b) and (c). In (d), it is shown that the interaction of see-saw mechanism [34, 23, 24, 36].

here, $j = e, \mu, \tau$. Combine the limits, from direct measurement and from cosmology, mass of 3 neutrino flavor[2] is less than 0.9eV.

Next Subject of Neutrino Oscillation Experiment

Direct measurement of neutrino masses and cosmology only give the upper limits of neutrino masses. On the other hand, neutrino oscillation experiment give the mass square difference(Δm^2) and mixing angle($\sin^2 2\theta$). From this experiment, lower limits of neutrino masses are known. Moreover, assumed that $m_{\nu_2} \gg m_{\nu_1}$ in $\nu_1 \leftrightarrow \nu_2$ oscillation, m_{ν_2} can be measured. From above features, neutrino oscillation experiment is the best way to measure neutrino masses at the present time.

Last year, $\nu_\mu \leftrightarrow \nu_\tau$ oscillation was observed, however $\nu_e \leftrightarrow \nu_x$ oscillation($x = \mu$ or τ, s $\cdots$) have not been observed. And, the discovery of $\nu_e \leftrightarrow \nu_x$ oscillation is looked forward to in the world.

[2]The number of neutrino flavor is 3 on the condition that neutrinos masses are less than 45GeV. This is the result from the measurement of the Z^0's decay width at LEP[24]

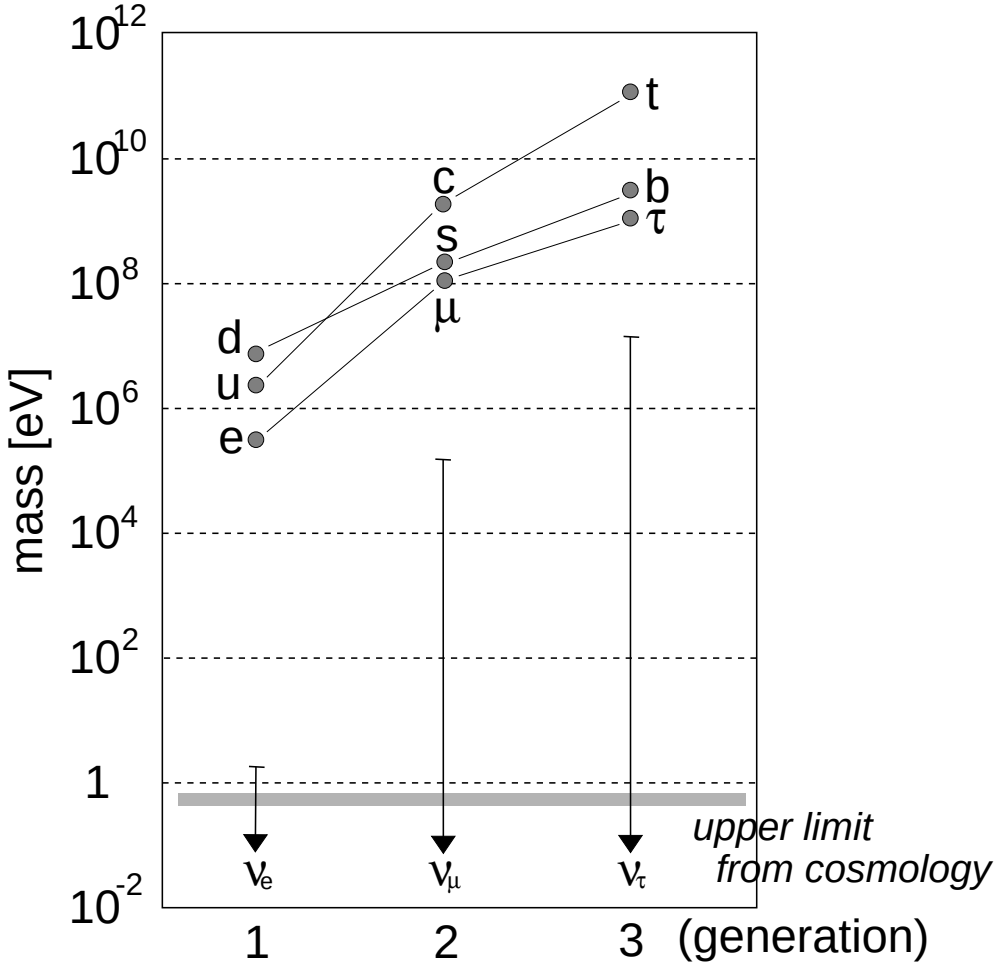

Figure 1.3: Mass of leptons and quarks. For neutrino mass, direct measurements only give upper limits. Recently, the cosmology suggests the upper limit of the neutrino mass because neutrino as dark matter does not need[12].

1.2 Neutrino Oscillation

A neutrino flavor changes to another flavor with time propagation if neutrinos have masses. This phenomenon is called "Neutrino Oscillation".

For massive neutrinos, the flavor eigenstates, ν_e, ν_μ, ν_τ, are not the same as the mass eigenstates, ν_1, ν_2, ν_3, and its relation is written by the mixing matrix which is the same matrix as the CKM matrix for quarks.

$$|\nu_\alpha\rangle = U_{\alpha j}|\nu_j\rangle \qquad (\alpha = e, \mu, \tau;\ \ j = 1, 2, 3) \tag{1.1}$$

From this relation, it is possible that one neutrino(ν_α) converts to another flavor(ν_β).

Time evolution of states obey the Shrödinger equation,

$$i\frac{d}{dt}|\nu_j\rangle = E_j|\nu_j\rangle \tag{1.2}$$

here E_j is the energy of ν_j, and the wave function can be written as

$$|\nu_j(t)\rangle = \mathrm{e}^{-iE_jt}|\nu_j(0)\rangle. \tag{1.3}$$

For flavor eigenstates, using Eq.1.1, 1.2 and 1.3,

$$\begin{aligned} i\frac{d}{dt}|\nu_\alpha\rangle &= U_{\alpha j}E_jU^\dagger_{j\alpha}|\nu_\alpha\rangle & (1.4)\\ |\nu_\alpha(t)\rangle &= U_{\alpha j}\mathrm{e}^{-iE_jt}U^\dagger_{j\alpha}|\nu_\alpha(0)\rangle. & (1.5)\end{aligned}$$

If ν_α is produced at $t = 0$, the probability of detecting this neutrino at $t = t$ is

$$\begin{aligned} P(\nu_\alpha \to \nu_\alpha) &= |\langle\nu_\alpha(t)|\nu_\alpha(0)\rangle|^2 & (1.6)\\ &= \left|\langle\nu_\alpha(t)|U_{\alpha j}\mathrm{e}^{-iE_jt}U^\dagger_{j\alpha}|\nu_\alpha(0)\rangle\right|^2 & (1.7)\end{aligned}$$

To simplify the problem, we consider only two flavors,

$$U = \begin{pmatrix} \cos\theta_V & \sin\theta_V \\ -\sin\theta_V & \cos\theta_V \end{pmatrix} \tag{1.8}$$

here θ_V is the mixing angle in vacuum between ν_e and ν_x. Therefore, the survival probability($P_{\nu_e\to\nu_e}$) of ν_e and oscillation probability($P_{\nu_e\to\nu_x}$) are;

$$\begin{aligned} P_{\nu_e\to\nu_e}(l, E; \Delta m^2, \sin^2 2\theta) &= 1 - \sin^2 2\theta_V \sin^2\left(\frac{\Delta m^2 t}{4p}\right) & (1.9)\\ &= 1 - \sin^2 2\theta_V \sin^2\left(\frac{1.27\Delta m^2[\mathrm{eV}^2]l[\mathrm{m}]}{4E[\mathrm{MeV}]}\right) & (1.10)\\ P_{\nu_e\to\nu_x}(l, E; \Delta m^2, \sin^2 2\theta) &= 1 - P_{\nu_e\to\nu_e} & (1.11)\\ &= \sin^2 2\theta_V \sin^2\left(\frac{1.27\Delta m^2[\mathrm{eV}^2]l[\mathrm{m}]}{4E[\mathrm{MeV}]}\right) & (1.12)\end{aligned}$$

here Δm^2 is the mass square difference between ν_e and $\nu_x(\Delta m^2 = \left|m_2^2 - m_1^2\right|)$, l is the propagation length in the time interval of t For $\bar{\nu_e} \to \bar{\nu_x}$ oscillation, these can be written similar expression.

From above equations, it is clear that $P_{\nu_e\to\nu_e} < 1$, so the number of observed $\nu_e(\bar{\nu_e})$ events are less than that of generated $\nu_e(\bar{\nu_e})$ events if $\nu_e(\bar{\nu_e})$ and $\nu_x(\bar{\nu_x})$ have finite different masses and there is a non-zero mixing angle between them.

1.3 Solar Neutrino Problem

First phenomenon which have implied $\nu_e \leftrightarrow \nu_x$ oscillation is **"solar neutrino problem"**. And this problem have not been solved for about 30 years.

The first measurement of the solar neutrino has been performed by Davis and his associates using a chlorine(^{37}Cl) radiochemical detector starting in 1968. However, the observed rate(2.6±0.2 SNU) is much less than the predicted rate(7.9±2.6 SNU) based on the Standard Solar Model(SSM)[1]. Here, SNU is the solar neutrino unit, [10^{-36}neutrino capture/atom/sec]. The value is the product of solar neutrino flux($cm^{-2}s^{-1}$) and cross section of the atom(cm^2). This is the "solar neutrino problem". Is the solar neutrino problem caused by unknown properties of neutrinos or by a lack of understanding of the interior of the Sun? In other words, is this a case of new physics or faulty astrophysics?

Standard Solar Models are the end product of a sequence of models. The calculation of a model begins with the description of a main sequence star that has a homogeneous composition. Hydrogen burns in the stellar core, supplying both the radiated luminosity and the thermal pressure that supports the star against the force of gravity. Successive models are calculated by allowing for composition changes caused by nuclear reactions, as well as the mild evolution of other tribution inside the star. A satisfactory solar model is a solution of the evolutionary equations that satisfies boundary conditions in both space and time. The Standard Solar Model gives a satisfactory account of what is known about the Sun from photons.

Helioseismology[1], like terrestrial seismology, provides information about the interior of the body under study by using observations of slight motions on the surface. The comparison between observed and calculated helioseismological sound speeds is precise($\sim 0.1\% RMS$)[20]. Figure 1.4 shows the fractional differences between the most accurate available sound speeds measured by helioseismology and sound speeds calculated with our best solar model(with no free parameters). The horizontal line corresponds to the hypothetical case in which the model predictions exactly match the observed values. The RMS fractional difference between the calculated and the measured sound speeds is 1.1×10^{-3} for the entire region over which the sound speeds are measured, $0.05R_\odot < R < 0.95R_\odot$. In the solar core, $0.05R_\odot < R < 0.25R_\odot$ (in which about 95% of the solar energy and neutrino flux is produced in a Standard Solar Model), the RMS fractional difference between measured and calculated sound speeds is 0.7×10^{-3}. Consider with this result, **the most popular explanation of a lack of solar neutrino is the neutrino oscillation**.

The inconsistency between theoretical calculation and observation has recently

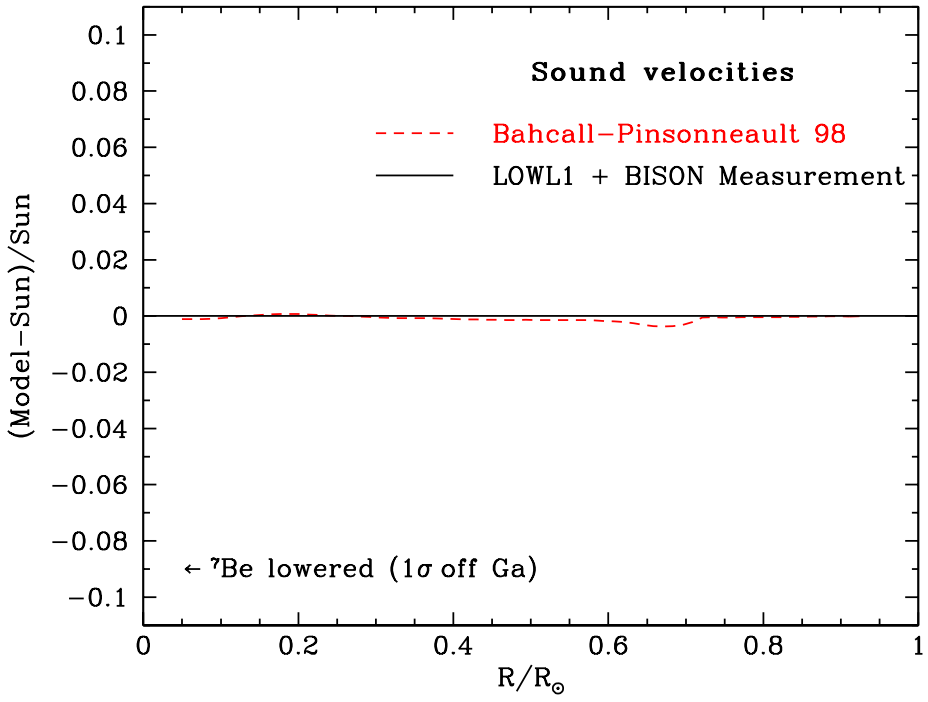

Figure 1.4: Predicted versus Measured Sound Speeds. This figure shows the excellent agreement between the calculated(Solar Model Bahcall-Pinsonneault98) and the measured(Sun) sound speeds, a fractional difference of 0.001 RMS for all speeds measured between $0.05R_{\odot}$ and $0.95R_{\odot}$.

been confirmed by an independent technique using the Japanese detector of neutrino-electron scattering, Kamiokande(II, III) and Super-Kamiokande. The flux ratio to the SSM(R) at Kamiokande is R=0.54±0.07, and R=0.475±0.015 at Super-Kamiokande. In addition, the results of ^{71}Ga experiments at Gran Sasso(it R=0.52±0.07) and at Baksan(R=0.59±0.06) is inconsistent to the calculation based on the SSM, the observed flux is much less than calculated value[35].

Above measurement results give four neutrino oscillation solutions. **VAC, LMA, SMA, LOW**(Figure1.5). **VAC** means the **vacuum oscillation** and is sometimes called as **just-so**. In that case, the oscillation length is comparable to the Sun-Earth distance. Assuming the MSW mechanism(chapterA.2), three possibilities are refered to as **large mixing angle solution(LMA), small mixing angle solution(SMA), and low Δm^2 solution(LOW)**.

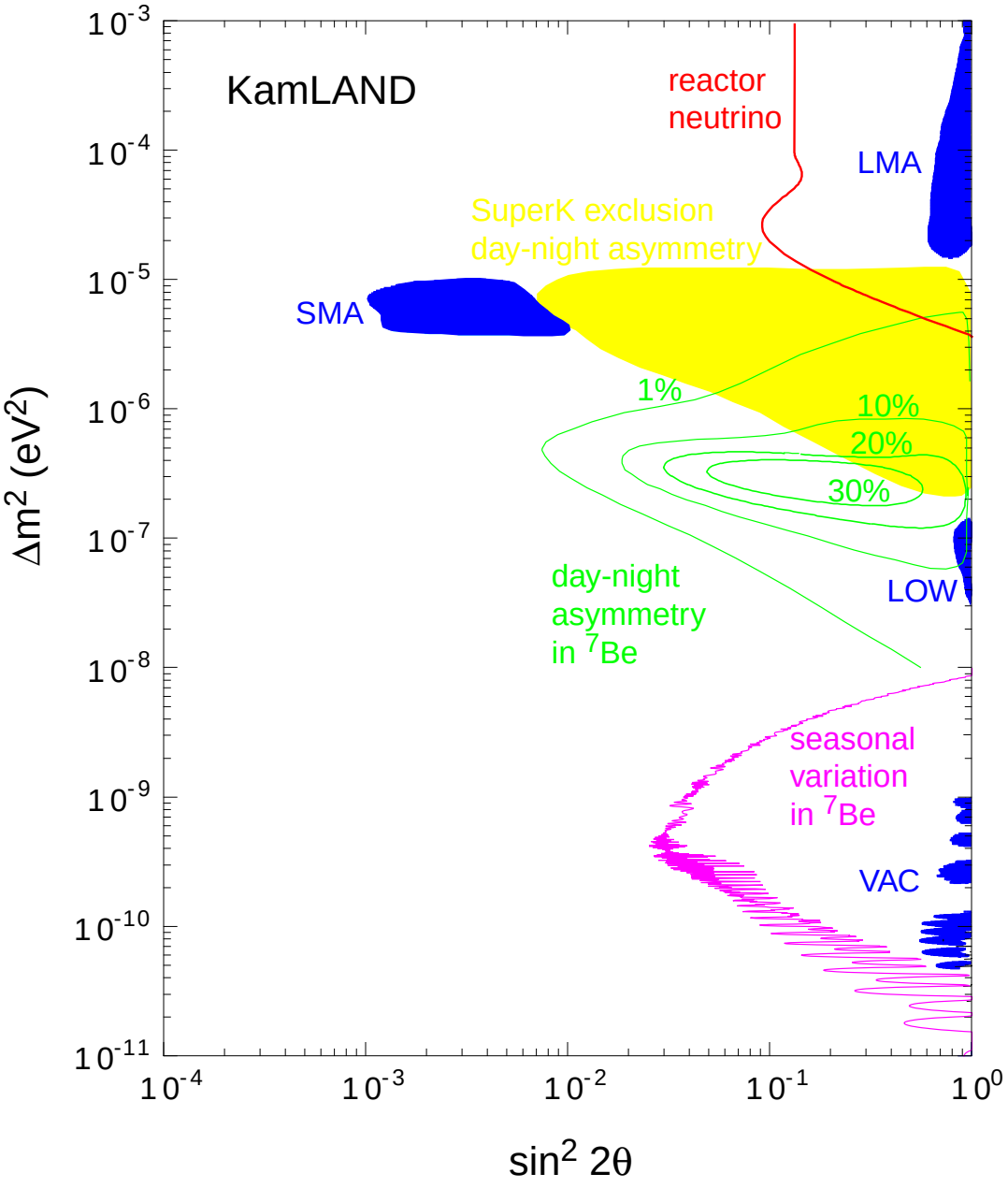

Figure 1.5: Four solutions, LMA, SMA, LOW and VAC, of the solar neutrino problem and the sensitivity of KamLAND experiment to them from the reactor neutrino study and the ^{7}Be solar neutrino studies. The LMA(Large Mixing Angle) solution is covered by the reactor neutrino study, the LOW(Low Δm^2) solution is covered by the day-night asymmetry of ^{7}Be neutrino flux, and VAC(Vacuum) solution is covered by the seasonal variation of ^{7}Be neutrino flux. Moreover, the SMA(Small Mixing Angle) solution can be recognized by essentially null flux of ^{7}Be neutrino.

1.4 KamLAND Experiment

KamLAND experiment is the $\nu_e \to \nu_x$ oscillation experiment, aiming at solving the solar neutrino problem. As described in Section 1.2, neutrino oscillation probability can be written as,

$$\mathrm{P}\left(\bar{\nu_e} \to \bar{\nu_x}\right) = \sin^2 2\theta \sin^2\left(\frac{1.27\Delta m^2[\mathrm{eV}^2]L[\mathrm{m}]}{E[\mathrm{MeV}]}\right) \tag{1.13}$$

here, L is the distance from a neutrino source to the detector, and E is the neutrino energy. From the formula, low energy neutrino detection and long baseline experiment give good sensitivity to low $\Delta m^2 \sim \frac{E}{L}$. KamLAND is relevant to the situation. It detects low energy anti-neutrinos(E:1.8MeV$\sim$10MeV) coming from long distant reactors(L $\geq$150km). It also aims at observing low energy solar neutrino, ^{7}Be(E=861keV) etc.

Figure1.6 shows the E/L[MeV/km] dependence of the survival probability(P $(\nu_x \to \nu_x)$), here $\Delta m^2 = 2 \times 10^{-5}[\mathrm{eV}^2]$ and $\sin^2 2\theta$=0.7(LMA solution) are assumed. "KamLAND Reactor Neutrino" shows the sensitive region of the KamLAND reactor anti-neutrino study. On the other hand, in Figure1.5, the right side of the line "reactor neutrino" is the sensitive region by reactor anti-neutrino at 90% CL, $\Delta m^2 \geq 6 \times 10^{-6}[\mathrm{eV}^2]$,$\sin^2 2\theta \geq 0.7$, based on 3k-ton·year data with 78% power. Here, it is assumed that there is no background. KamLAND is the most sensitive detector about Δm^2 in the world, and can examine the LMA solution directly for the first time in the world.

By observing solar neutrinos, especially ^{7}Be, KamLAND can explore the LOW solution with a possible day-night asymmetry, the VAC solution with a seasonal variation and the SMA solution can be recognized by essentially null flux of ^{7}Be neutrinos. Moreover, ^{7}Be neutrino flux and to compare other experiments, SNO, results will search the SMA solution.

The other various neutrinos, terrestrial anti-neutrino, supernova, relic anti-neutrino from the past supernova search for are also the subject of KamLAND experiment. And new knowledge to the geo physics, cosmology and so on will be brought by KamLAND.

KamLAND experiment will solve the solar neutrino problem and new physics is aiming at opening.

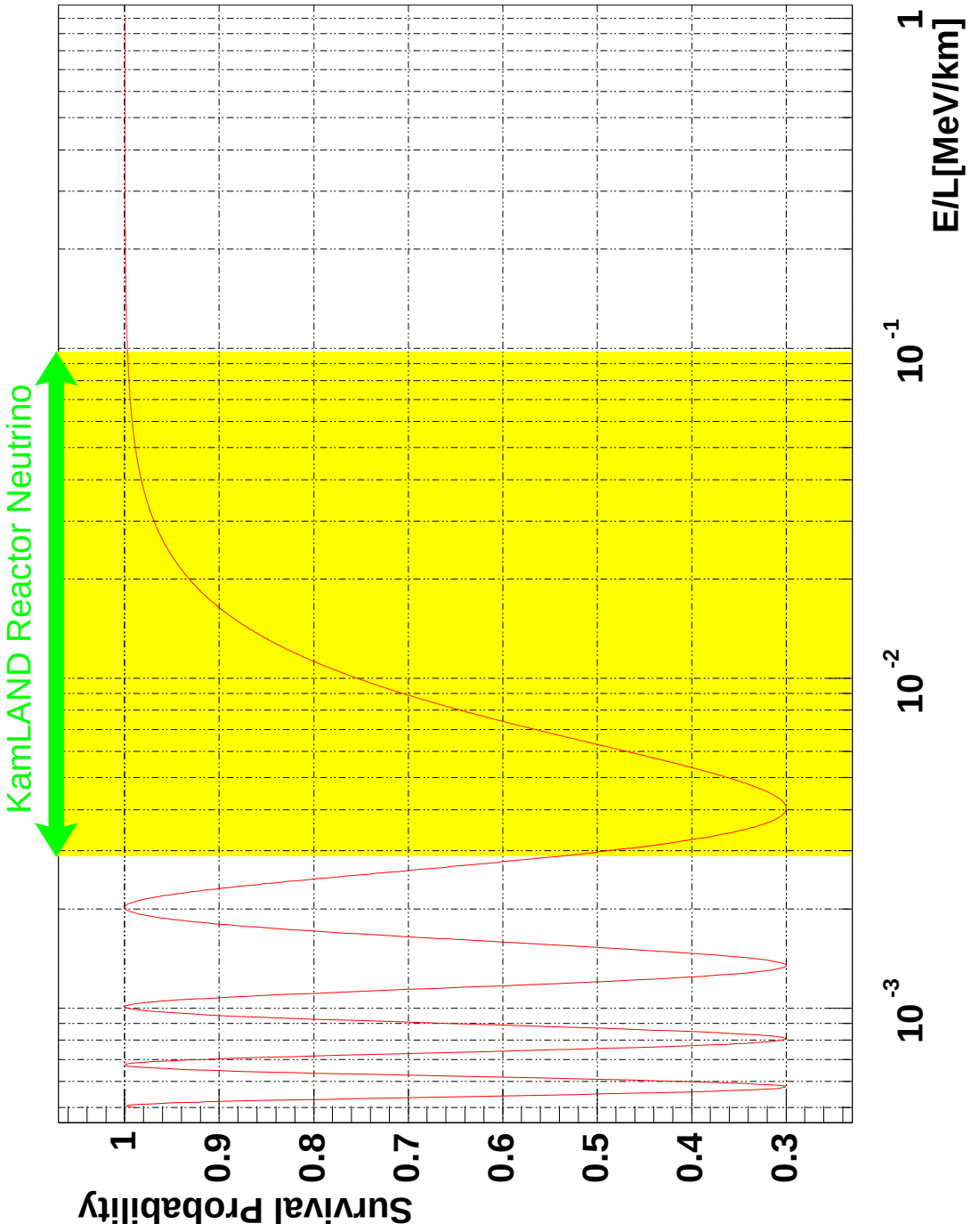

Figure 1.6: The E/L[MeV/km] dependence of the survival probability(P ($\nu_x \to \nu_x$)), here it is assumed that $\Delta m^2 = 2 \times 10^{-5}$[eV^2] and $\sin^2 2\theta$=0.7 which are LMA solution values. "KamLAND Reactor Neutrino" shows the sensitive region of the KamLAND reactor anti-neutrino study.

1.5 KamLAND Detector

The KamLAND detector is sited in the old Kamiokande cavity under the summit of Mt. Ikenoyama. The site is ∼50km south of Toyama city. At this location the rock overburden in any direction is more than 1,000meters. With an average rock density of 2.7g/cm^3 the minimum surface energy required for a muon to reach the detector is 1.3TeV. The total muon rate in KamLAND is estimated 0.2∼0.4Hz.

Figure 1.7 shows the KamLAND detector. The primary detector target consists of 1,200m^3 of ultra-pure liquid scintillator located at the center of the detector, and this is put in the transparent sevenfold layer film, EVOH[3] and fivefold nylon and EVOH, sphere(balloon) whose diameter is 13m. This liquid scintillator consists of normal paraffin oil N12[4](80%), pseudocumene(20%) and PPO(1.5g/l), optimized to obtain good light output and transparency(Chapter4, 5). Surrounding the scintillator vessel(balloon) is a spherical shielding shell with 2.5m thick of ultra-pure paraffin oil buffer and acrylic resin sheet(thickness 3mm) against γ-rays which comes from the PMT-glass and so on. The density of this buffer oil is as same as the density of the scintillator(difference 0∼0.3%) so that the safety of the balloon is secured.

The scintillator is viewed by an array of photomultipier tubes (17" and 20"PMT) supported on a 18m diameter stainless steel spherical vessel. The 17"PMT is developed for the KamLAND experiment, and 20"PMT has been used for the old KAMIOKANDE. 17"PMT improved from the 20"PMT used at Super-Kamiokande. By limiting the photon acceptance area to the central 17inches and replacing original Venetian-blind dinode to a line-focus type(Figure1.8), so that the transit time spread(TTS) and peak-to-valley(P/V ratio) are significantly improved. Details of 17"PMT are described in 1.5.2. The number of 17"PMT is 1,295 and that of 20"PMT is 590, resulting the coverage to be the about 30%. TTS of the 17"PMT is ∼3nsec(FWHM) which is much better than that of the Super-Kamiokande 20"PMT, ∼5.5nsec(FWHM) and the old KAMIOKANDE 20"PMT, ∼7nsec(FWHM). The vertex reconstruction will be carried out using timing information of only 17"PMTs, and the energy measurement will be done using charge information of both the 17"PMTs and the 20"PMTs.

The stainless sphere is surrounded with the ultra-pure water. This water absorbs much of the radioactivity coming from rock walls and moderates fast neutrons produced in the rock. Moreover, this is the cosmic-ray veto counter, detecting Cherenkov photons with old KAMIOKANDE 20"PMTs.

We estimate that the background rate of the anti-neutrino event is about 0.07

[3]This is the effective material to suppress Rn permeation.

[4]This is made by Cosmo Petrolium Company, Japan.

events/day[31]. On the other hand, the event rate of the anti-neutrino from the nuclear reactor is estimated about 2events/day.

The detected photon is converted to the electric analog signal by the PMT. Using the KamLAND electronics[5], this analog signal is converted to digital information, detected time, charge and waveform of each PMT. The event trigger will created using some information of PMTs, the number of hit, charge, time and so on. When trigger signal is created, these information are edited to a lump of data for recording on magnetic tape mediated the data acquisition system, kinoko[29]. 'kinoko' stands for "Kinoko Is Network distributed Object oriented KamLAND Online system", and there are many fresh features, network distributed parallel processing, object oriented design and so on. Finally, the data will be recorded on the magnetic tape using the storage system[6] and will be analyzed using it. Figure 1.9 shows signal and data stream in KamLAND.

[5]This electronics is developed by KamLAND LBL-electronics group.

[6]Data storage system is now developing based on object oriented design

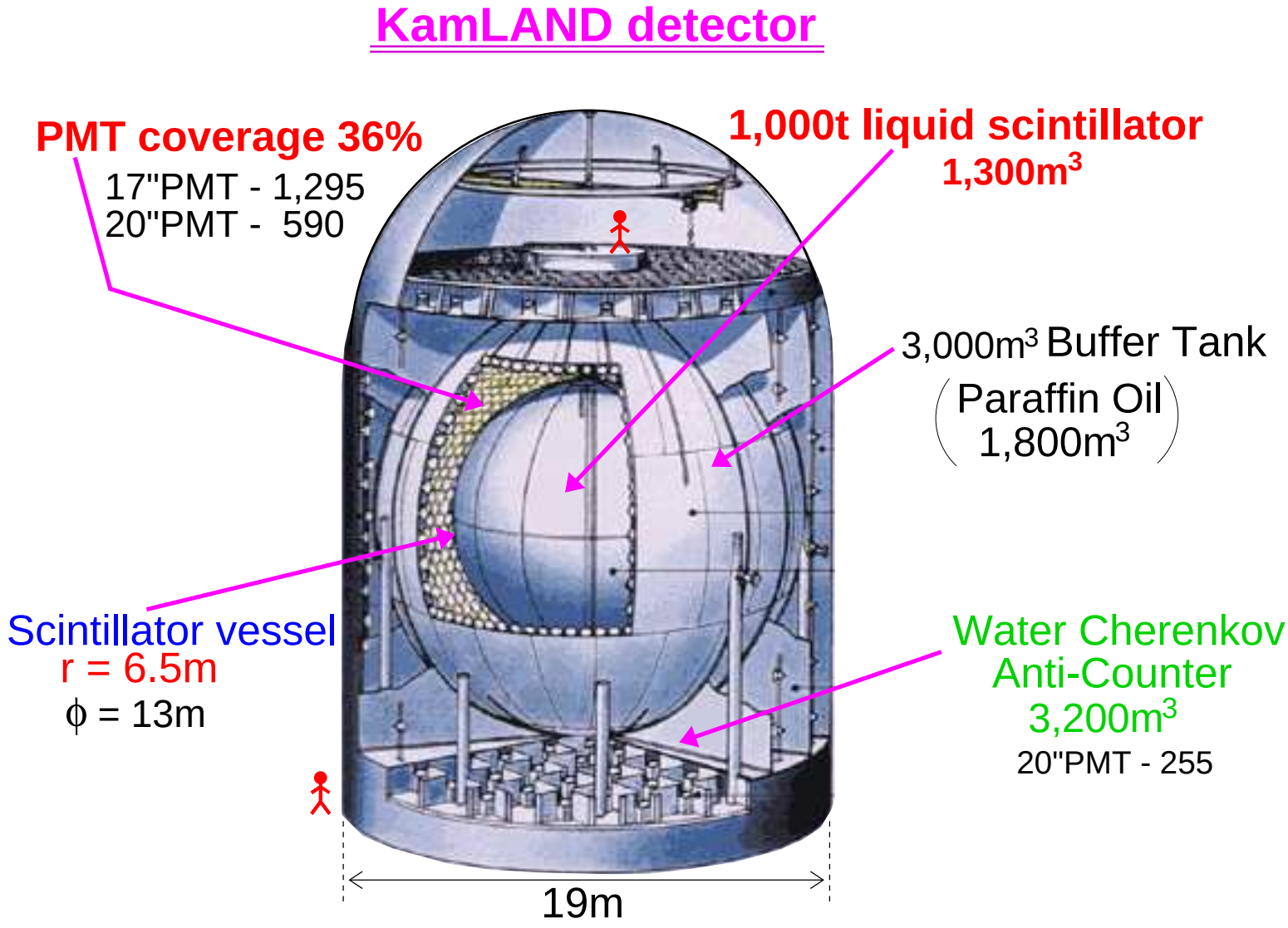

Figure 1.7: KamLAND detector

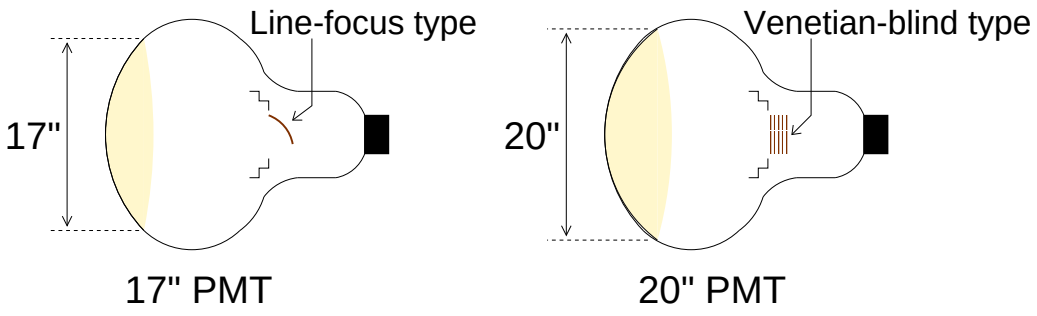

Figure 1.8: Mechanical differences between 17"PMT and 20"PMT are shown in this figure. The diameter of the photon acceptance area are 17" and 20", dinode are line-focus type or Venetian-blind type, respectively.

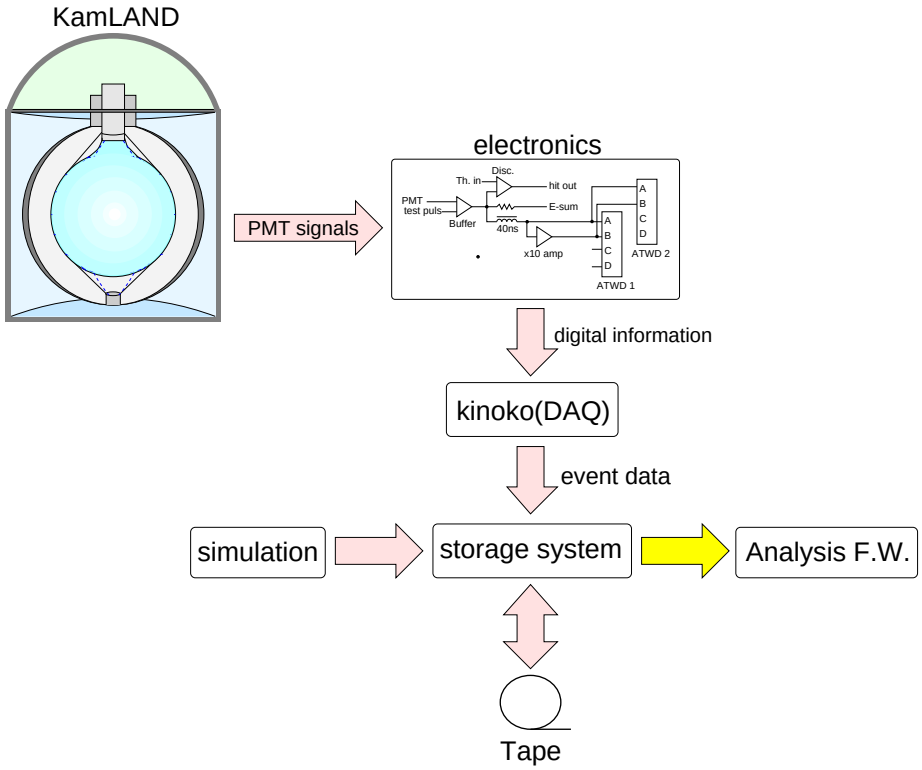

Figure 1.9: Signal and data stream in KamLAND. PMT signals are converted to digital information using electronics, and digital information are edited to the event data by kinoko. Finally, the data is recorded on the magnetic tape using the storage system.

1.5.1 Liquid Scintillator & Buffer Oil

The amount of the liquid scintillator for KamLAND is about 1,200m^3. Light attenuation length of commercially available liquid scintillators is not long enough for the large KamLAND, and these scintillators costs too much.

Following features are required to make the KamLAND experiment feasible.

1. Light output and the transparency need to be good.
   The radius of the scintillator vessel is very long(6.5m), and the good transparency and the high light output($\sim$ 50%Angthracen[7]) are necessary.

2. U, Th and K contamination should be low(U, Th$\leq 10^{-16}$g/g, K$\leq 10^{-14}$g/g).
   Internal background needs to be very low for super low energy experiment[8].

3. PSD[9] efficiency among γ-ray and α, neutron should be high
   PSD is very effective to suppress backgrounds. Fast neutrons and α from Rn can will be suppressed using this method.

4. Quenching factor for α needs to be high.
   Light emission of scintillators in response to α particle irradiation is strongly suppressed in comparison with electron irradiation of the same energy. It is very effective to suppress the background events from α particles in the decay chain of the ^{238}U, ^{232}Th and ^{222}Rn.

5. H/C ratio of the scintillator material is high.
   Anti-neutrino is detected via the $\bar{\nu_e}$p interaction, and its event rate depends on the number of free proton in the scintillator.

6. Nonpoisonous and hight flash point for safety

Resulted from the R&D(Chapter4,5 and [31, 27, 26, 32]) considering above demands, the KamLAND liquid scintillator is paraffin oil(C_nH_{2n+2}) base,

$$\text{N12(80\%) + P.C.(20\%) + PPO(1.5g/l)},$$

here N12[10] is the paraffin oil($C_{12}H_{26}$), and P.C., pseudocumen(1,2,4-Trimethyl Benzene) is one of the most popular solvents, and PPO(2,5-diphenyloxazole) is one of the most popular solute. Figure1.10, 1.11, 1.12 show the molecular formula of each components. Paraffin oil is a non-saturated compound, and non-circular structure, the

[7] 100%Anthracene = 17,000 p.e./MeV
[8] Ex. the recoil electron energy of the ^{7}Be solar neutrino is less than 670keV
[9] Pulse Shape Discrimination
[10] Normal Paraffin N12D, Cosmo Petrolium Company, Japan

transparency of it is very good(Chapter4 and [27]) and chemically stable. H/C-ratio of paraffin is large, ∼2.17.

Buffer oil is a mixture of paraffin oils,

$$\text{N12(60\%)} + \text{P250(40\%)}$$

here P250[11] is iso-paraffin oil(C_nH_{2n+2}, n∼14) which has the branches of CH_3. Density difference between the liquid scintillator and the buffer oil will be controlled at 0∼0.3%.

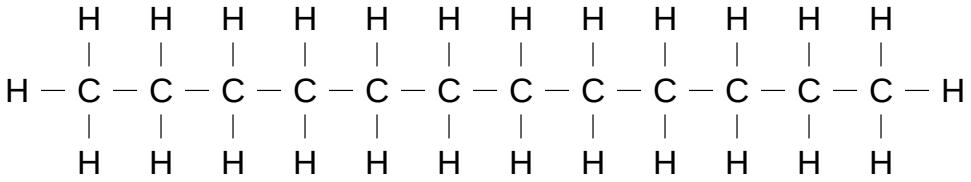

Figure 1.10: Molecular formula of N12.

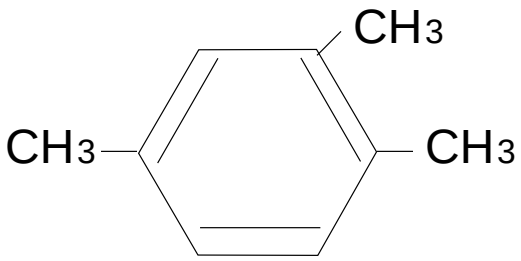

Figure 1.11: Molecular formula of Pseudocumene(P.C.).

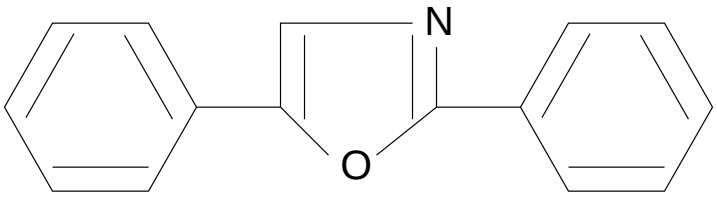

Figure 1.12: Molecular formula of PPO.

[11]Paraol 250, Showa Shell, Japan

1.5.2 Photomultiplier Tube(PMT)

KamLAND will detect low energy neutrinos and anti-neutrinos done to a few hundred keV. For better photon collection efficiency and vertex resolution, large photo-sensitive area and good timing resolution are necessary. We have developed new 17"PMT improved from the 20"PMT used at Super-Kamiokande. By limiting the photon acceptance area to the central 17inches and replacing original Venetian-blind dinode to a line-focus type, TTS(transit time spread) is significantly improved from ∼5.5nsec(FWHM) to ∼3nsec(FWHM), and P/V ratio(peak-to-valley) is improved from ∼1.5 to ∼3.

In Figure 1.14, qualities of 17"PMT and 20"PMT are compared. The shaded histogram denotes 17"PMT, and plain histogram denotes 20"PMT used at Super-Kamiokande. SKb(Sensitivity of Kathord to blue) of 17"PMT is a little better than 20"PMT. The supply voltage at 10^7 gain is a few hundred Volts higher. Dark current, dark pulse rate, TTS(Transit Time Spread) and P/V ratio get better. Especially, TTS and P/V ratio are much better than the old ones.

Magnetic field dependences almost negligible for the experiment. From the measurement, pulse hight at the magnetic field below 50mGauss is less than 20%. A set of compensating coils will be installed in the cavern to cancel the magnetic field of the earth(∼500mGauss) to a level well below the limit of 50mGauss necessary for a proper operation of the photomultipliers.

Quantum efficiency(Q.E.) of 17"PMT is shown in Figure 1.13. Wavelength dependence of Q.E. is decided by a material of photo-cathode, bialkali, although an individual difference exists because of the thickness of it. Therefore, Q.E. of 20"PMT is almost same.

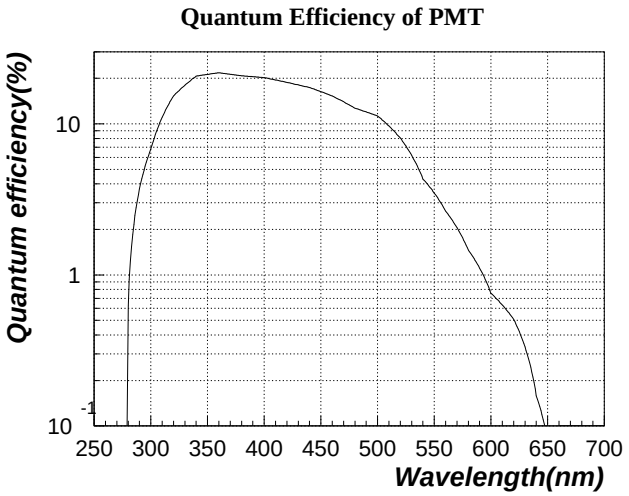

Figure 1.13: Quantum efficiency of PMT

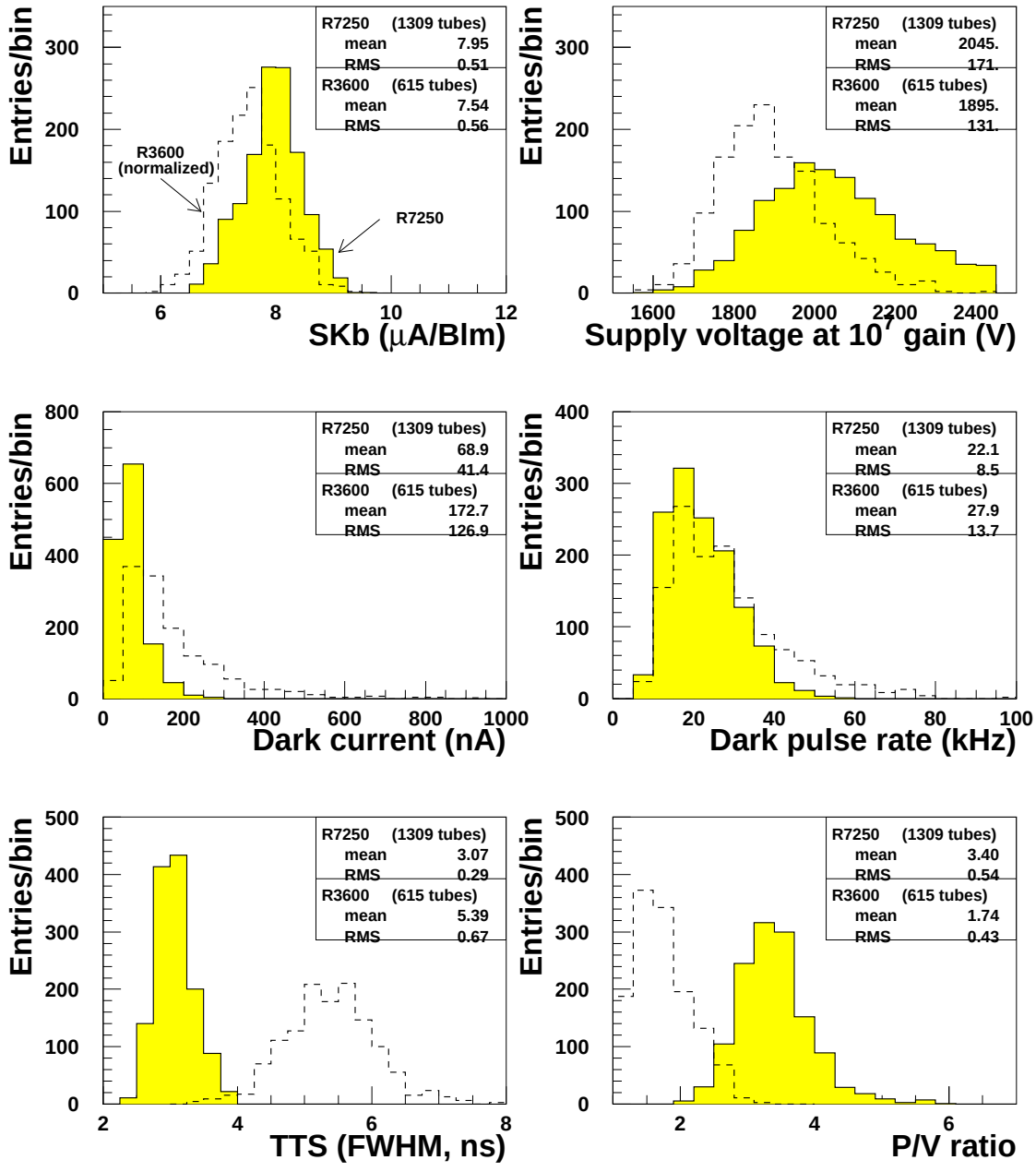

Figure 1.14: This figure shows some qualities of 17"PMT(shaded histogram) and 20"PMT. SKb(sensitivity of kathord to blue) of 17"PMT is a little better than that of 20"PMT. The supply voltage at 10^7 gain is a few hundred Volts higher. Dark current, dark pulse rate get little better. TTS and P/V ratio are much better than the old ones. Almost all qualities of 17"PMT are better than 20"PMT's without supply voltage.

Chapter 2

Neutrinos and Anti-Neutrinos Detection at KamLAND and Their Background

At first section, a delayed coincidence technique is described as am electron-anti-neutrino($\bar{\nu}_e$) detection method, and which is essential for the long baseline neutrino oscillation experiment using reactor anti-neutrinos. This technique provides not only a knowledge of $\bar{\nu}_e$ energy but also very strong background suppression. The $\bar{\nu}_e$ event rate from Japanese nuclear reactors are estimated to be about 2 events/day. And the background rate for the delayed coincidence signal is estimated as 0.07event/day assuming radioactive impurities of U, Th $\leq 10^{-16}$g/g, K$\leq 10^{-14}$g/g and Rn $\leq 1\mu$Bq/cm^3 at which we are aiming.

Next, we describe a neutrino detection(especially solar neutrino) with a neutrino-electron elastic scattering. Observation of ^{7}Be solar neutrino plays important role to explore the SMA, LOW and VAC solutions. Since the recoil electron has kinematically distributing spectrum, electron energy can not be translated to neutrino energy one by one. However, in case of monochromatic neutrino detection, 862keV ^{7}Be neutrino, as our subject, produces a sharp edge in its spectrum. The ^{7}Be solar neutrino can be observed quantitatively by recognizing this edge.

Moreover, we mention interactions between neutrinos and ^{12}C. These interactions are very important in a supernovae neutrinos detection.

2.1 Electron-Anti-Neutrino Detection

2.1.1 Delayed Coincidence Technique - Detection Process -

Electron-anti-neutrinos, $\bar{\nu}_e$, create **delayed coincidence signals** in KamLAND. In the inverse β-decay of $\bar{\nu}_e$ reaction a positron and a neutron are emitted;

$$\bar{\nu}_e \mathrm{p} \rightarrow \mathrm{n}e^+ \tag{2.1}$$

$$E_{threshold} = \Delta m_{\mathrm{np}} + m_e = 1.804\mathrm{MeV} \tag{2.2}$$

Here, Δm_{np}(=1.293MeV) is the mass difference of a proton and a neutron, and m_e(=0.511MeV) is the electron mass. This positron deposits its energy by ionization and then annihilates ($e^+e^- \rightarrow 2\gamma(511\mathrm{keV})$), here intensity of the scintillation by this prompt signal($E_{visible}$) reflects incident $\bar{\nu}_e$ energy($E_{\bar{\nu}_e}$);

$$E_{visible} = E_{\bar{\nu}_e} - \Delta m_{\mathrm{np}} + m_e \tag{2.3}$$

$$= E_{\bar{\nu}_e} - 0.782\mathrm{MeV} \tag{2.4}$$

On the other hand, the neutron is thermalized in the scintillator and captured by a proton in environment, and produces dutron associatedng 2.2MeV γ-ray;

$$\mathrm{np} \rightarrow \mathrm{d}^* \rightarrow \mathrm{d}\gamma(2.2\mathrm{MeV}) \tag{2.5}$$

Mean time from inverse β-decay to neutron capture is $\sim$175μsec,

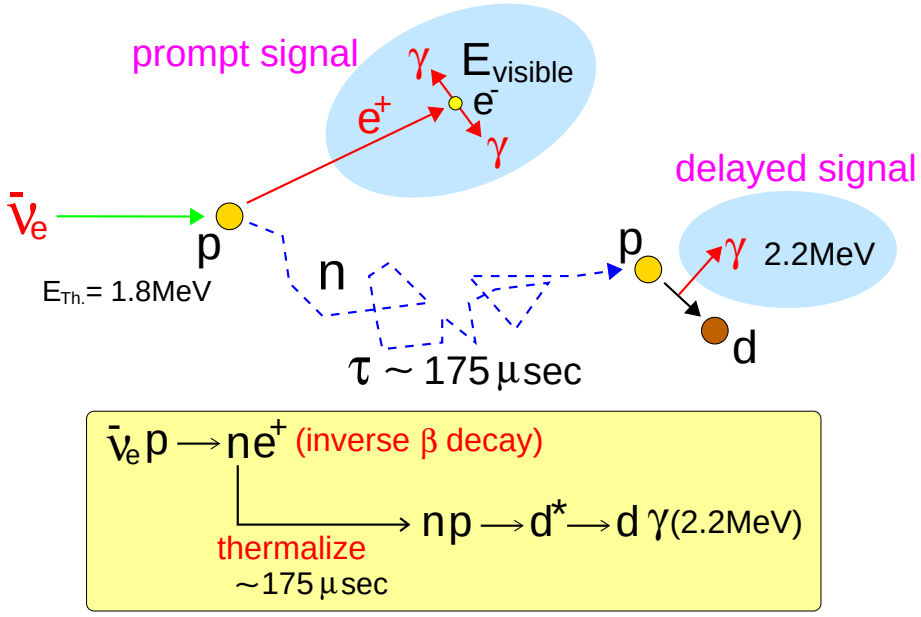

Figure 2.1: $\bar{\nu}_e$ - p interaction(inverse β-decay) and neutron capture process.

2.1.2 Cross Section of $\bar{\nu}_e \mathrm{p} \rightarrow \mathrm{n}e^+$[28, 22]

The lowest-order cross section for the $\bar{\nu}_e \mathrm{p} \rightarrow e^+ \mathrm{n}$ interaction is expressed by a following formula.

$$\begin{aligned}
\sigma_0\left(E_{\bar{\nu}}\right) &= \frac{2\pi^2}{m_e^5 f \tau_{\mathrm{n}}} P_e E_e & (2.6)\\
&= \frac{2\pi^2}{m_e^5 f \tau_{\mathrm{n}}} \left(E_{\bar{\nu}} - \Delta m_{\mathrm{np}}\right) \sqrt{\left(\mathrm{E}_{\bar{\nu}} - \Delta m_{\mathrm{np}}\right)^2 - m_e^2} & (2.7)\\
&= 9.55 \times 10^{-44} \left(E_{\bar{\nu}} - 1.293\right) \sqrt{\left(E_{\bar{\nu}} - 1.293\right)^2 - 0.511^2} \quad [\mathrm{cm}^2] & (2.8)
\end{aligned}$$

$$\begin{aligned}
f &= 1.6857 : \text{usual statistical function}\\
\tau_{\mathrm{n}} &= 886.7 \pm 1.9[\mathrm{sec}] : \text{neutron life time}\\
\Delta m_{\mathrm{np}} &= m_{\mathrm{n}} - m_{\mathrm{p}} = 1.293[\mathrm{MeV}]
\end{aligned}$$

Here, it is assumed that a neutron is infinitely heavy, and the unit of a $E_{\bar{\nu}}$ is [MeV]. The value, $f\tau_{\mathrm{n}}$, is obtained from a neutron β decay.

Further calculation has been provided by Vogel with several corrections to the above formula, δ_{WM} for the weak magnetism interference, δ_{rec} for the recoil, δ_{rad} for the radiative correction. The weak magnetism arising from difference in anomalous magnetic moments of neutrons and protons, $\mu = \mu_{\mathrm{n}} - \mu_{\mathrm{p}} = 4.71\mu_{\mathrm{N}}$(nuclear magneton). The radiative corrections includes a contribution from internal bremsstrahlung, and its order is α.

$$\sigma\left(E_{\bar{\nu}}\right) = \sigma_0\left(E_{\bar{\nu}}\right)\left(1 + \delta_{rec} + \delta_{WM} + \delta_{rad}\right) \quad (2.9)$$

From higher order calculation[28, 22],

$$\begin{aligned}
\delta_{WM} &= \frac{-2\mu(g_A/g_V)}{1 + 3(g_A/g_V)^2} \frac{E_{\bar{\nu}} + \beta\sqrt{\left(E_{\bar{\nu}} - \Delta m_{\mathrm{np}}\right)^2 - m_e^2}}{m_{\mathrm{p}}}\\
\delta_{rad} &= 11.7 \times 10^{-3} \left(E_{\bar{\nu}} - \Delta m_{\mathrm{np}} - m_e\right)^{-0.3}\\
\delta_{rec} &= \frac{1}{1 + (g_A/g_V)^2}\\
&\quad \times \left[\left((g_A/g_V)^2 - 1\right)\frac{\Delta m_{\mathrm{np}}}{m_{\mathrm{p}}} + (g_A/g_V - 1)^2 \frac{E_{\bar{\nu}}(E_{\bar{\nu}} - \Delta m_{\mathrm{np}})\sqrt{\left(E_{\bar{\nu}} - \Delta m_{\mathrm{np}}\right)^2 - m_e^2}}{m_{\mathrm{p}}(E_{\bar{\nu}} - \Delta m_{\mathrm{np}})}\right]
\end{aligned}$$

Here, $g_A/g_V = 1.2670 \pm 0.0035$ is the ratio of axial-vector and vector coupling constants, and $\beta = \sqrt{1 - m_e^2/(\mathrm{E}_{\bar{\nu}} - \Delta m_{\mathrm{np}})^2}$.

2.1.3 Event Rate[28, 22]

The event rate using lowest-order cross section is

$$Y_0\left(E_{\bar{\nu}}\right) \;=\; N_{\mathrm{p}}\sigma_0\left(E_{\bar{\nu}}\right)n\left(E_{\bar{\nu}}\right) \tag{2.10}$$

where, N_{p} is number of proton in a detector and $n\left(E_{\bar{\nu}}\right)$ is a $\bar{\nu}_e$-flux.

More correct estimation is using $\sigma\left(\mathrm{E}_{\bar{\nu}}\right)$ and another correction(δ_{spec}). When the recoil of neutron cannot be negligible, i.e. the energy of $\bar{\nu}_e$ is high, measured anti-neutrino energy $\mathrm{E}_{\bar{\nu}}(= E_{e^+} + \Delta m_{\mathrm{np}})$ is smaller than the true energy $E_{\bar{\nu}}^{(real)}$. That is to say, the real energy of anti-neutrino is bigger than detected energy which is calculated using visible energy. From the energy and momentum conservation, the relation[28, 22] of $\mathrm{E}_{\bar{\nu}}$ and $\mathrm{E}_{\bar{\nu}}^{(real)}$ is

$$E_{\bar{\nu}} = E_{\bar{\nu}}^{(real)} - \frac{1}{m_{\mathrm{p}}}\left[E_{e^+}\left(E_{e^+} + \Delta m_{\mathrm{np}}\right) + \frac{\Delta m_{\mathrm{np}}^2 - m_e^2}{2}\right] \tag{2.11}$$

and δ_{spec} is

$$\delta_{spec}\left(E_{\bar{\nu}}\right) \equiv \frac{n\left(E_{\bar{\nu}}^{(real)}\right) - n\left(E_{\bar{\nu}}\right)}{n\left(E_{\bar{\nu}}^{(real)}\right)} < 0 \tag{2.12}$$

To the end, corrected event rate is

$$\begin{aligned} Y\left(E_{\bar{\nu}}\right) &= N_{\mathrm{p}}\sigma\left(E_{\bar{\nu}}\right)n\left(E_{\bar{\nu}}\right)\left(1+\delta_{spec}\right) && (2.13)\\ &= Y_0\left(E_{\bar{\nu}}\right)\left(1+\delta_{rec}+\delta_{WM}+\delta_{rad}\right)\left(1+\delta_{spec}\right) && (2.14)\\ &= Y_0\left(E_{\bar{\nu}}\right)\left(1+\delta_{rec}+\delta_{WM}+\delta_{rad}+\delta_{spec}\right) && (2.15) \end{aligned}$$

2.2 Neutrino detection using Elastic Electron Scattering

2.2.1 Recoil Electron -Detection Process -

In the liquid scintillator, the electron which is scattered by a neutrino can be detected via the scintillation light. The electron recoil energy T_e is

$$T_e = \frac{\frac{2E_\nu^2}{m_e}\cos^2\theta}{\left(1+\frac{E_\nu}{m_e}\right)^2 - \left(\frac{E_\nu}{m_e}\right)^2\cos^2\theta} \tag{2.16}$$

$$\leq \frac{E_\nu}{1+m_e/2E_\nu} \equiv T_{max} \tag{2.17}$$

where, T_e and θ are electron kinetic energy and angle between incident neutrino and recoil electron, respectively. Although the recoil electron has kinematically distributing energy, monochromatic energy would give rise to a recoil electron spectrum characterized by a sharp edge at T_{max}(Figure 2.3).

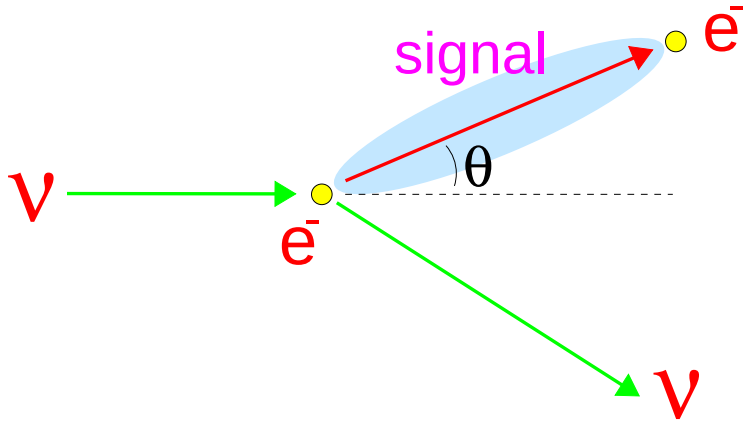

Figure 2.2: ν - e interaction.

2.2.2 Cross Section

Cross section in a laboratory system for $\nu_{\mu,\tau}e \to \nu_{\mu,\tau}e$ or $\nu^-_{\mu,\tau}e \to \nu^-_{\mu,\tau}e$ elastic scattering is

$$\frac{d\sigma_{\nu_{\mu,\tau},\nu^-_{\mu,\tau}}}{dy} = \frac{G_F^2 m_e E_\nu}{2\pi} \times \left[(g_V \pm g_A)^2 + (g_V \mp g_A)^2(1-y)^2 - \left(g_V^2 - g_A^2\right)^2 \frac{y m_e}{E_\nu}\right]$$

$$g_V = -\frac{1}{2} + 2\sin^2\theta_W, g_A = -\frac{1}{2}$$

here the upper(lower) sign refers to $\nu_{\mu,\tau}$ ($\nu^-_{\mu,\tau}$), and $y \equiv T_e/E_\nu$ (which) runs from 0 to $(1+m_e/2E_\nu)^{-1}$ is the ratio of the kinetic energy of the recoil electron to the incident

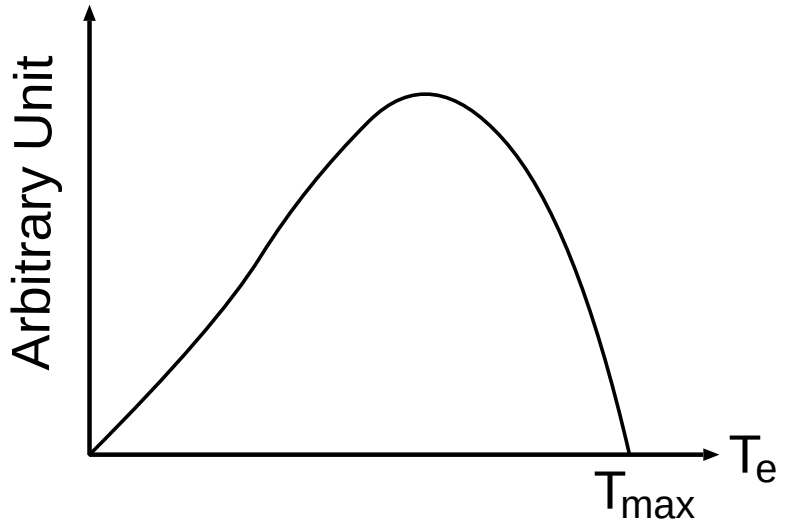

Figure 2.3: Recoil electron spectrum when neutrino energy is constant.

ν or $\bar{\nu}$ energy. And a total cross section[1] is;

$$\sigma_{\nu_{\mu,\tau},\nu_{\bar{\mu},\tau}} = \frac{G_F^2 m_e E_\nu}{2\pi}\left[(g_V \pm g_A)^2 + \frac{1}{3}(g_V \mp g_A)^2\right]. \quad (2.18)$$

The cross section for $\nu_e e$ and $\bar{\nu}_e e$ be obtained by replacing $g_{V,A}$ by $g_{V,A}+1$ in above equations, here 1 coming from a charged-current contribution.

$$\sigma_{\nu_e,\bar{\nu}_e} = \frac{G_F^2 m_e E_\nu}{2\pi}\left[((g_V+1) \pm (g_A+1))^2 + \frac{1}{3}((g_V+1) \mp (g_A+1))^2\right] \quad (2.19)$$

[1]The most accurate leptonic measurements of $\sin^2\theta_W$ are from the ratio $R \equiv \sigma_{\nu_{\mu,\tau}e}/\sigma_{\nu_{\bar{\mu},\tau}e}$ in which many of the systematic uncertainties cancel.

2.3 Other Detection Methods via ^{12}C Interaction

There are three relevant neutrino reactions on carbon, and they are particularly important for a supernova detection at KamLAND.

for ν_e:

$$\nu_e + {}^{12}C \rightarrow {}^{12}Ne^- \quad (E_{Th.} = 17.3MeV) \tag{2.20}$$

$$^{12}N \rightarrow {}^{12}Ce^+\nu_e \quad (T_{1/2} = 11.0msec) \tag{2.21}$$

for $\bar{\nu}_e$:

$$\bar{\nu}_e + {}^{12}C \rightarrow {}^{12}Be^+ \quad (E_{Th.} = 14.4MeV) \tag{2.22}$$

$$^{12}B \rightarrow {}^{12}Ce^-\bar{\nu}_e \quad (T_{1/2} = 20.4msec) \tag{2.23}$$

They can be recognized by observing both the corresponding $e^{\pm}$ and the delayed $\beta^{\pm}$ decay with half-lives of 11.0 and 20.4msec, respectively. Thus, signals from these reactions will be essentially background free.

The neutral current reaction;

$$\nu_{e,\mu,\tau}(\bar{\nu}_{e,\mu,\tau}) + {}^{12}C \rightarrow {}^{12}C^*\nu_{e,\mu,\tau}(\bar{\nu}_{e,\mu,\tau}) \quad (E_{Th.} = 15.11MeV) \tag{2.24}$$

$$^{12}C^* \rightarrow {}^{12}C\gamma(15.11MeV) \tag{2.25}$$

All neutrino flavors can excite ^{12}C; the cross section depends only on the neutrino energy.

2.4 Background Estimation in KamLAND

2.4.1 Background from Cosmic Ray Muons[7, 19]

Cosmic ray muon interacts with nuclei, muon capture and muon spallation, and many radioactive nuclei, pion and neutron are produced. Secondary interactions or decays of these new products are background sources which cannot be removed in preparation. The muon flux at the KamLAND site has been measured by the old Kamiokande[10], and the muon flux was $3.5\times10^{-8}\mathrm{cm}^{-2}\mathrm{sr}^{-1}\mathrm{s}^{-1}$. Assuming a $\cos^2\theta$ zenith angle distribution, this flux is translated to a muon rate of 0.44Hz in the central detector and 1.45Hz in the veto detector.

To remove background derived from cosmic ray muons, the veto condition is assumed, fiducial cut along with muon track space($\leq$ 1m) for 3sec when muon go through the detector. Under this veto condition, background events are limited following in two ways[7];

- Radioactive nuclei with life times of order 100msec or greater which are produced by muon spallation.
- Fast neutron which is generated in the rock outside of the KamLAND detector. This fast neutron can pass undetected through the veto counter and generate a background event in the central detector.

Table 2.1 shows major background from muon spallation in the detector. For single event($\nu e \rightarrow \nu e$), ^{11}C and ^{7}Be are serious background source which produced by muon spallation. These two isotopes cannot be removed by above veto-condition because of their long life-times, mean life-times are 1.76×10^3 for ^{11}C and 6.64×10^6 for ^{7}Be, respectively. Decay modes are $^{11}\mathrm{C}\rightarrow \beta^+(1.98\mathrm{MeV})$ and $^{7}\mathrm{Be}e^- \rightarrow ^{7}\mathrm{Li}\gamma(478\mathrm{keV})$. Thier production rates are estimated about 400/kt/day for ^{11}C and about 300/kt/day for ^{7}Be, respectively.

The ^{11}C minimum visible decay energy of 1.02MeV is above the endpoint of the ^{7}Be neutrino scattering spectrum(665keV), but it can still be a limiting background for the ^{7}Be neutrino experiment due to the limited energy resolution of the detector.

The ^{7}Be visible decay energy is a line spectrum at 478keV, broadened by the energy resolution of the detector. This is a potentially insidious background for the solar neutrino experiment.

On the other hand, we estimate that 12,400 neutrons per day are produced in the rock shell. For solar neutrino detection, background form this fast neutron is cut almost all due to a fiducial cut(fiducial volume is 300ton). Additionally, Number of fast neutrons whose deposited energy are above 3MeV in the detector is estimated 3

Background	τ[sec.]	Energy[MeV]	Production Method	Rate[day^{-1}]
^{11}C decay	1.76×10^{3}	1.98	^{12}C(γ,n)^{11}C	240
^{10}C decay	27.8	3.65	^{12}C(γ,2n)^{10}C	43
^{7}Be decay	6.64×10^{6}	0.478	^{12}C($\gamma, n\alpha$)^{7}Be	17
^{11}Be decay	19.9	11.5	^{12}C(π^{-},p)^{11}Be	0.5
^{8}Li decay	1.21	13.0	^{12}C(π^{-}, α)^{8}Li	7.7

Table 2.1: Major background from muon spallation interactions[30].

events/day. This is negligible compare to background rate from the natural radioactivity. For a delayed confidence event, background rate is estimated 0.07 events/day on the following trigger conditions;

- $E_{prompt} \geq$1MeV
- 1.8MeV$\leq E_{delayed} \leq$2.7MeV
- $|V(x,y,z)_{prompt} - V(x,y,z)_{delayed}| \leq$1m
- $10\mu\text{sec} \leq T_{delayed} - T_{prompt} \leq 500\mu\text{sec}$

Here, $V(x,y,z)$ denotes Vertex of each event. This is far less than reactor $\bar{\nu}_e$ event rate, 2 events/day.

2.4.2 Background from Natural Radioactivity in the Scintillator[7]

^{238}U, ^{232}Th, ^{40}K, ^{222}Rn and ^{14}C are background sources which dissolved in the scintillator. The U/Th concentration in the scintillator will be less than 10^{-16}g/g, which corresponds to 1.2×10^{-3}Bq/kt for U and 4.1×10^{-4}Bq/kt for Th, respectively. The content of K will be less than 10^{-14}g/g(3.1×10^{-4}Bq/kt), and the ratio ^{14}C/^{12}C = 10^{-18}(163Bq/kt). And noble gas Rn penetrates into the scintillator and decay there, its rate will be less than 1μBq/m^3(1.3×10^{-3}Bq/kt). Additionally, ^{7}Be and ^{11}C which are produced by cosmic-ray muons are also background sources, and their production rate are $\sim$400/kt/day and $\sim$3000/kt/day, respectively.

Since it is not possible to measure the background without the presence of the neutrino signal, alternative methods have to be envisaged to accurately infer the background rate. The most crucial U/Th and Rn contribution would be determined through Bi-Po coincidences. The decay tables of ^{238}U and ^{232}Th are shown in Appendix B. In case of U/Rn, ^{214}Bi β-decay is quickly followed by the ^{214}Po α-decay($T_{1/2} = 164\mu$sec). The ^{212}Bi-^{212}Po pair in the Th decay series has a correlation time of 0.30μsec. A tagged

background sample would also give the measured spectral shape of these components. Assuming to the tagging efficiency is 95%, β and γ of ^{214}Bi and the corresponding α of ^{214}Po are removed on the event by event basis for U. Similarly, the pair of decays β and γ of ^{212}Bi and α of ^{212}Po are also removed for Th.

Moreover, since the correlated Bi-Po rates will be accurately known, decays are necessarily in equilibrium with them can be accurately subtracted(so-called "statistical subtraction"). α of ^{222}Rn and ^{218}Po and $\beta+\gamma$ of ^{214}Pb will be subtracted in the U/Rn chain. In the Th chain the subtraction involves ^{224}Ra, ^{220}Rn, ^{216}Po and ^{212}Bi α and ^{212}Pb and ^{208}Tl $\beta+\gamma$. The shape of these decays can be independently determined.

α particle can be separated from $\beta^{\pm}$ and γ-ray by the pulse shape discrimination (PSD), these efficiency is estimated 90%(Section 4.1, and [31]). And the quenching factor to relate the α energy with the equivalent β, γ energy was measured at 13.8[32]. These technique and property are very effective to the background suppression.

In Figure 2.4, upper figure shows a energy spectra of the estimated background for a single event after the "statistical subtraction" with $\delta E/E = 10\%\sqrt{E(\mathrm{MeV})}$ of energy resolution. Lower figure shows recoil electron from solar neutrinos and the sum of background spectra as a function of the energy, here flux of solar neutrino is assumed SSM(Standard Solar Model). At this energy resolution, energy threshold for the solar neutrino detection will be 280keV(signal to noise ratio, S/N, is about $\sim$1 at this energy) because of the ^{14}C(Q_{β^-}=156.475keV) contamination.

Background rates of individual components in the relevant energy interval 280-800keV is shown in Table2.2. In that interval, the signal will be dominated by ^{7}Be solar neutrino, 466 events/kt/day at SSM.

On the other hand, accidental coincidences of single events make a false $\bar{\nu}_e$ signal. The single event rate above 1MeV from all natural radioactivities in the scintillator is estimated 936 events/day. On the condition of a delayed coincidence trigger, accidental rate is aproximatedly 0.005 events/day. Correlated background from ^{214}Bi-^{214}Po, $\beta+\gamma$ and $\alpha(6.9\mathrm{MeV})+\gamma(0.8\mathrm{MeV})$, pair event is estimated 0.0003 events/day, and correlated background from other Bi-Po, $\beta+\gamma$ and α, pair events are suppressed due to α-quenching. Because a event rate of reactor $\bar{\nu}_e$ is estimated 2 events/day, the background for a delayed coincidence signal from natural radioactitivities in the scintillator may be ignored.

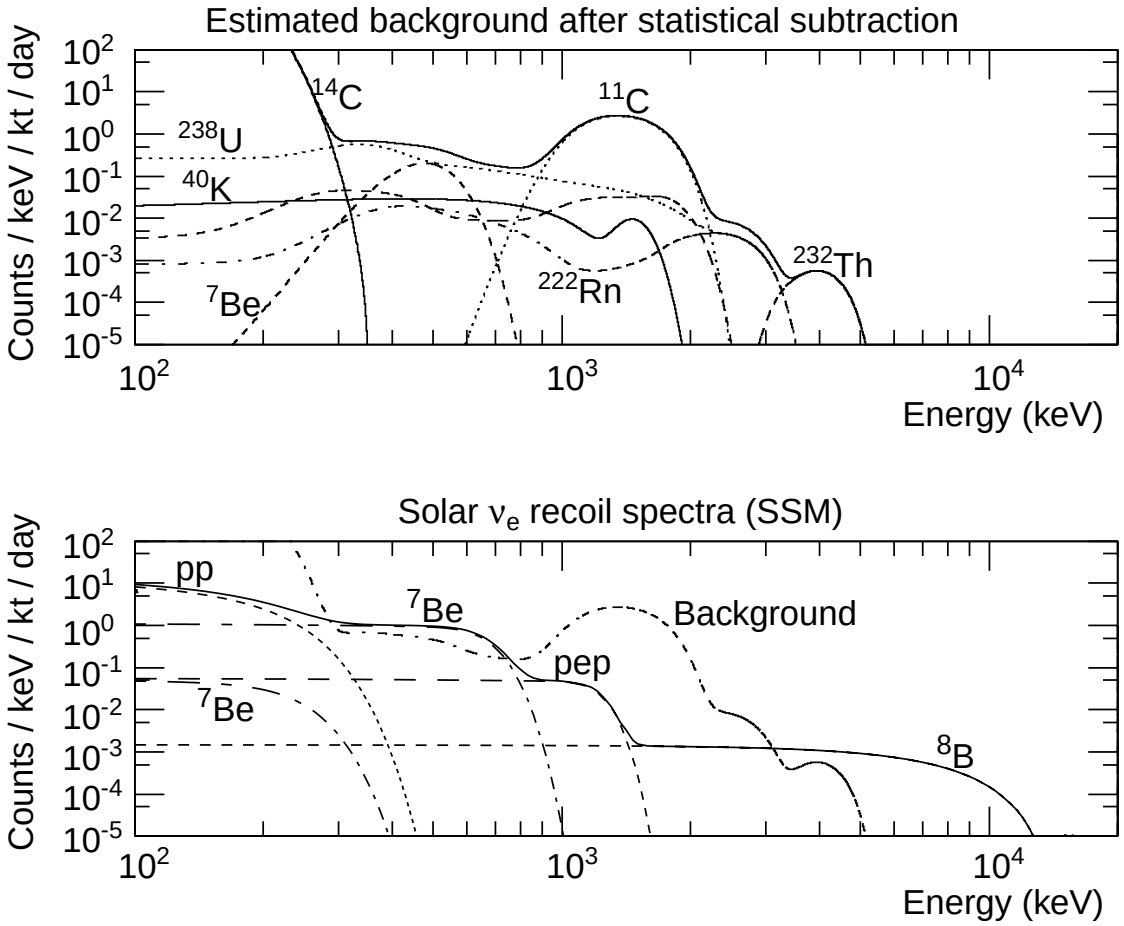

Figure 2.4: Recoil electron and background for solar neutrinos at KamLAND. The upper figure shows a decomposition of the calculated background spectrum after the "statistical subtraction"(Section 2.4.2) and sum of them without the recoil electrons spectrum of solar neutrinos. The quenched α component[32] was added statistically. The lower figure shows the recoil electron's energy spectrum derived from the solar neutrinos based on SSM, together with the total background. All spectra folded with the resolution $\delta E/E = 10\%/\sqrt{E(\mathrm{MeV})}$ which corresponding to the light yield 100p.e./MeV. ^{7}Be solar neutrino events are recognized using the compton edge of the recoil electron($T_e \leq$665keV).

		isotope	total	PSD and α-quenching	Statistical Subtraction
U	$\beta+\gamma$	^{234}Pa	39.3	39.3	39.3
		^{214}Pb	90.5	90.5	4.5
		^{214}Bi	4.4	0.2	0.2
		^{210}Bi	46.8	46.8	46.8
	α	all	755.8	46.6	46.6
Rn	$\beta+\gamma$	^{214}Pb	91.3	91.3	4.6
		^{214}Bi	4.4	0.2	0.2
	α	all	318.6	26.5	1.6
Th	$\beta+\gamma$	^{228}Ac	3.3	3.3	3.3
		^{212}Pb	23.1	23.1	1.2
		^{212}Bi	9.8	0.5	0.5
		^{208}Tl	0	0	0
	α	all	191.2	6.5	6.2
K	$\beta+\gamma$	^{40}K	14	14	14
^{14}C	β	^{14}C	13	13	13
Cosmogenic		^{11}C	0.6	0.6	0.6
		^{7}Be	35	35	35
Total			2463	438	217

Table 2.2: Estimated background rate(events/kt/day) in the range 280keV to 800keV. Contaminations are assumed 10^{-16} for U/Th, 10^{-14} for K, 1μBq/m^3 for Rn and ^{14}C/^{12}C=10^{-18}. And production rates of ^{7}Be and ^{11}C are assumed to be 400/kt/day and 3000/kt/day, respectively.

.

Chapter 3

KamLAND Physics and Required Features for the Detector

KamLAND will observe various neutrinos and anti-neutrinos, and we can study various phenomena, neutrino oscillation and so on. In this chapter, we describe the study will be achieved in KamLAND and requirements for the detector to observe these neutrinos in the last section.

The main target at KamLAND is the verification of $\nu_e(\bar{\nu_e}) \rightarrow \nu_x(\bar{\nu_x})$ oscillation and solving the "Solar Neutrino Problem". Now there are four reasonable neutrino oscillation solutions, LMA, SMA, LOW and VAC solution, to explain the solar neutrino anomaly, these solutions are implied by many experimental results. KamLAND can examine all of these solutions. LMA solutions can be examined directly using the anti-neutrino from Japanese nuclear reactors. And SMA, LOW and VAC solutions can be explored by ^{7}Be solar neutrino observation.

The other subjects of KamLAND are observation of terrestrial anti-neutrino, supernova neutrinos, and anti-neutrinos from the sun and past supernova. KamLAND will detect terrestrial anti-neutrinos which are products of the heat source in the Earth, and open the new physics. The terrestrial anti-neutrino will be recognized by characteristic two edges at 2.3MeV and 3.3MeV. Supernova neutrinos were first detected by old KAMIOKANDE[8], and impressed to all over the world. KamLAND has a chance to study on surpernova more detail than KAMIOKANDE. In addition, KamLAND will search for the anti-neutrinos from solar and past supernovae.

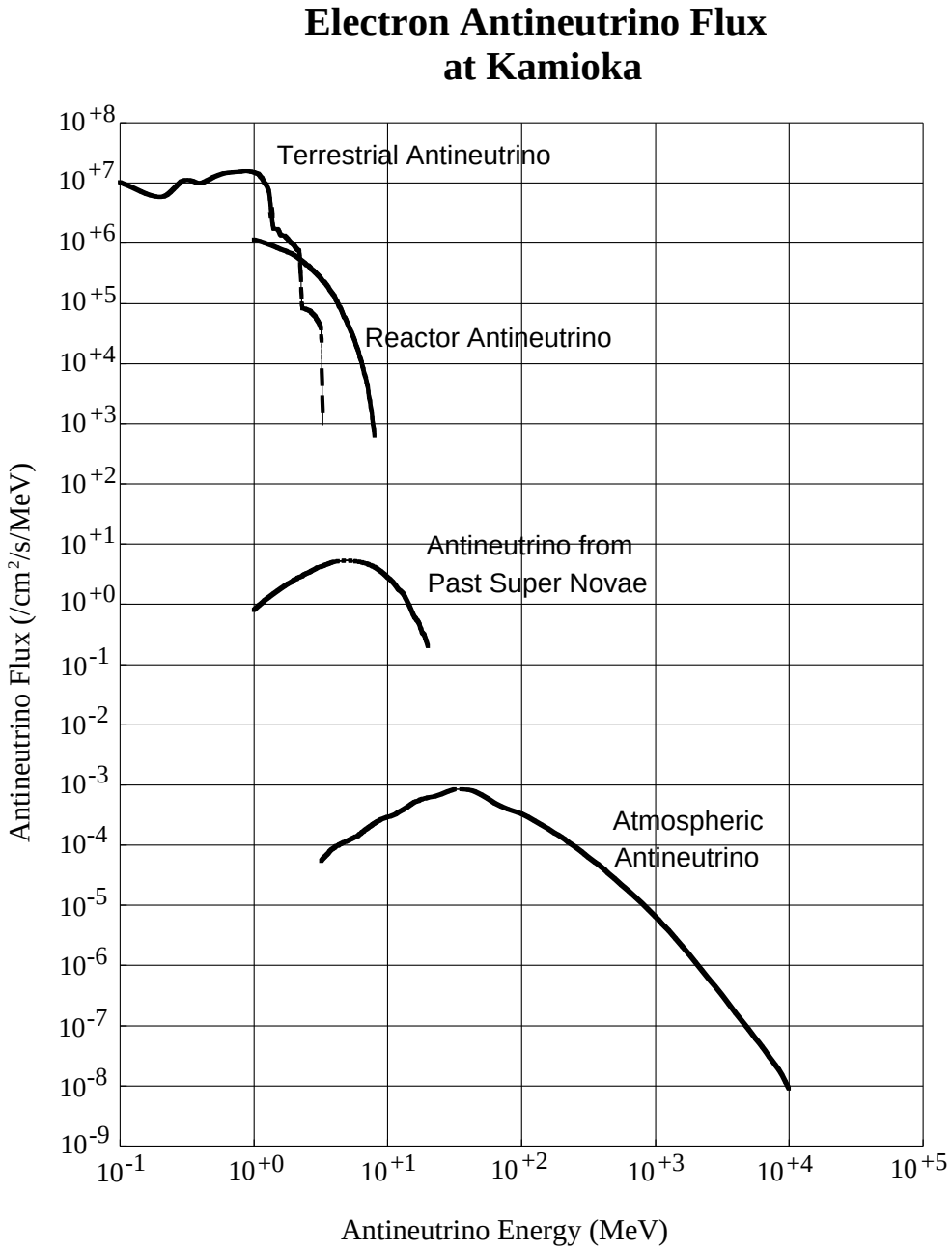

Figure 3.1: Expected $\bar{\nu}_e$ flux at the site of KamLAND.

3.1 Long Baseline Neutrino Oscillation Experiment Using Reactor Anti-Neutrino

Neutrino oscillation is observed at KamLAND from reactor anti-neutrino detection if LMA solution is correct. The energy of reactor anti-neutrino is about several MeV, and the distance from reactors to Kamioka is about 170km on average. Figure 3.2 shows the relation between distance from Kamioka to each Japanese reactors and expected event rate from each reactors. Number of emitted $\bar{\nu}_e$ at each reactor is proportional to the reactor power, and expected flux at Kamioka is depends on to the power flux. Power flux is defined as;

$$(\text{power flux}) = \frac{p_i}{4\pi r_i^2} \tag{3.1}$$

here, p_i is the electricity output of each reactor and r_i is the distance from Kamioka to each reactor. "Kashiwazaki" reactors are main anti-neutrino source. KamLAND is the long baseline neutrino oscillation experiment, and neutrino oscillation is observed from verification that the number of detected events is smaller than expected number of events. On this condition, KamLAND will can examine LMA solution($\Delta m^2 \sim 2 \times 10^{-5}[\text{eV}^2]$, $\sin^2 2\theta \sim 0.7$) directly for the first time in the world.

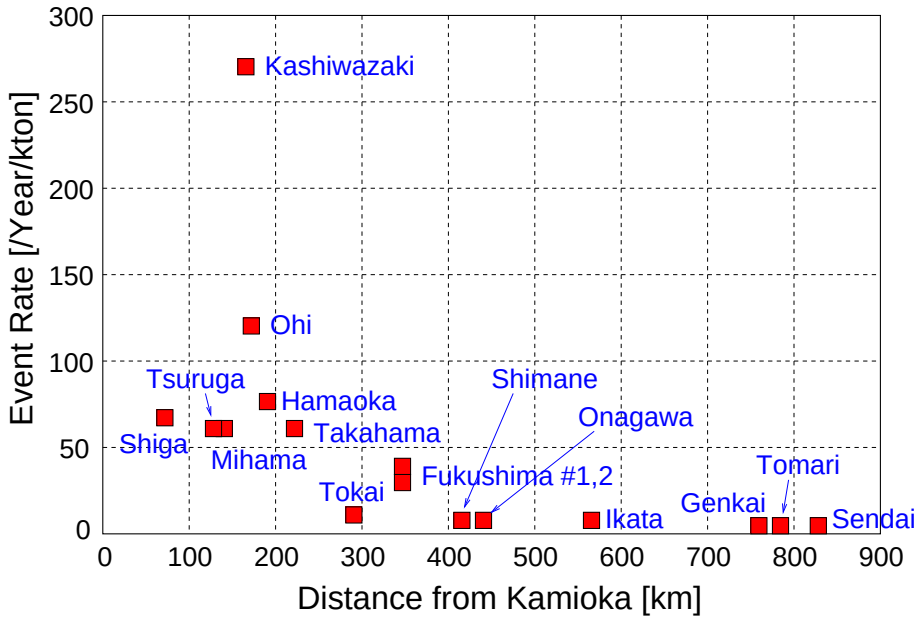

Figure 3.2: Distance from Kamioka to each Japanese reactors and expected event rates derived from each reactors. About 80% of all anti-neutrino events from reactors comes from the reactors which are place in the region from 140km to 210km.

3.1.1 Anti-Neutrino from Reactor

The anti-neutrino flux and spectrum depend only on the four isotopes ^{235}U, ^{238}U, ^{239}Pu and ^{241}Pu being fissioned in the reactor. Anti-neutrinos are produced by long chains of daughter isotopes and hundreds of different β-decays. Contribution percentages of these four isotopes are 70% of ^{235}U , 30% of ^{239}Pu and those of ^{238}U and ^{241}Pu are very small as ignored. The energy dependences of number of anti-neutrino from one fission derived from ^{235}U and ^{239}Pu are shown in Figure 3.3 which are measurement results[4, 11]. The uncertainty is about 3%.

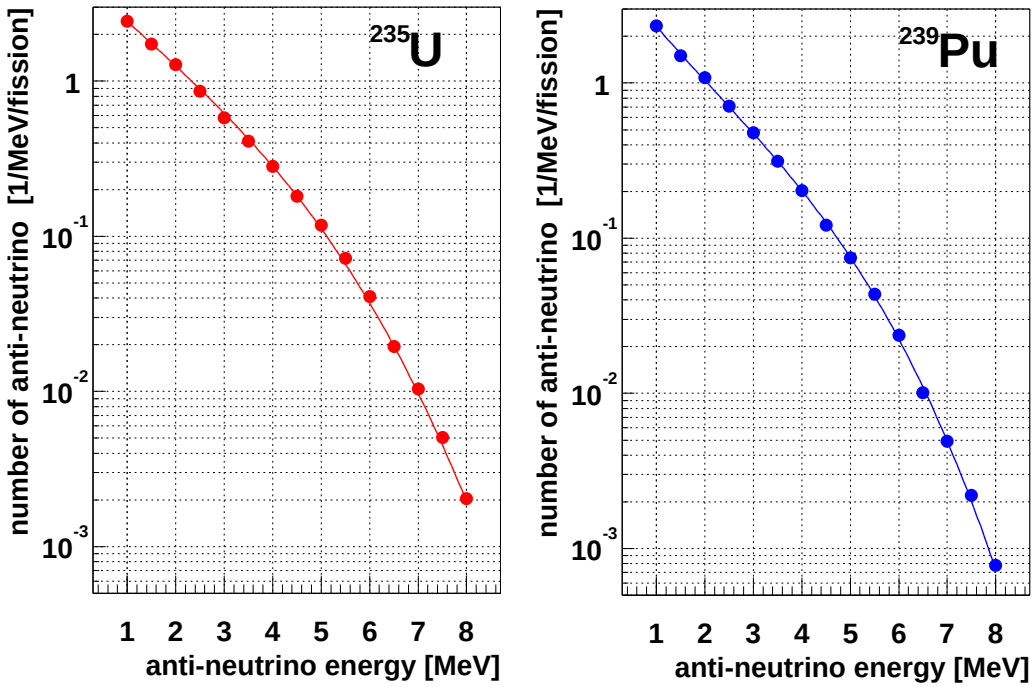

Figure 3.3: The energy spectrum of the number of anti-neutrino from one fission derived from ^{235}U and ^{239}Pu. These are measurement results at [4, 11].

The modeling of such processes is very difficult, but there is now very good agreement between theoretical calculations and experimental data[15, 3, 6]. Although fission rate of each isotopes are changed about 30%, total error in these measurements are about 1.4%. The expected average anti-neutrino flux at Kamioka from Japanese reactors are shown in Figure 3.4. This flux is calculated using the electricity output data from April 1997 to March 1998, and assumed that ^{235}U/^{239}Pu contribution ratio is 70%/30%. Here it is not considered the influence of neutrino oscillation.

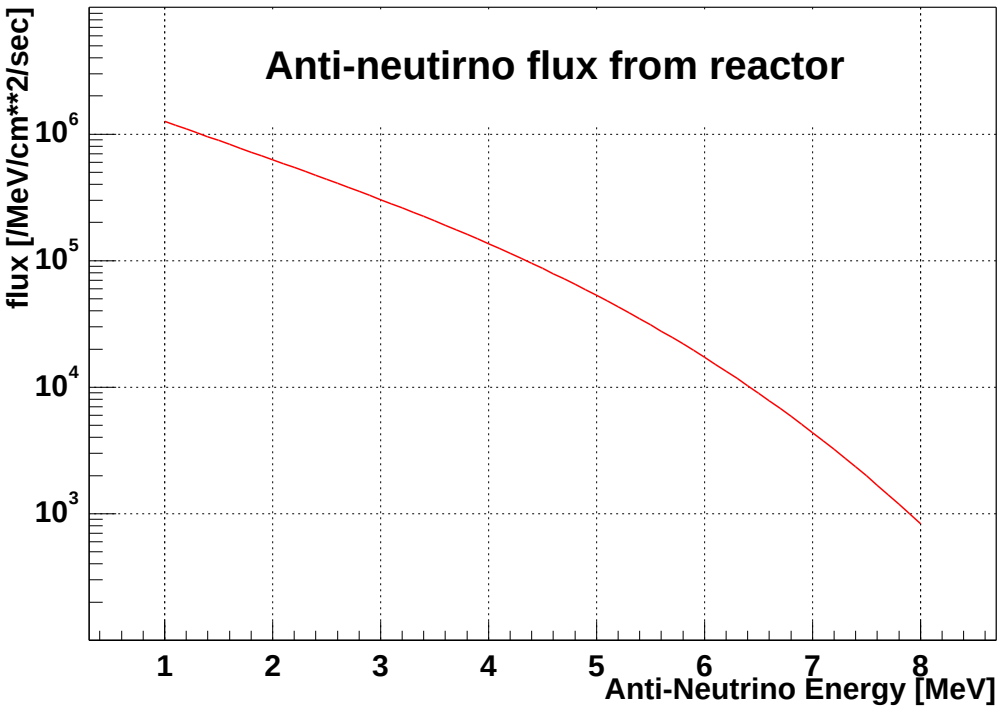

Figure 3.4: Anti-neutrino mean flux at Kamioka from the nuclear reactors which is calculated using the electricity output data from April 1997 to March 1998. In this figure, it is not considered about oscillation.

3.1.2 Oscillation Study using Anti-Neutrino from Reactor

Event Rate and Energy Spectrum Shape

Visible energy spectra of anti-neutrino event is shown in Figure 3.5 for 3kt·year statistics. The cross section for the calculation of these spectrum is lowest-order, and the visible energy denotes the detected energy of the prompt event in delayed coincidence event, $E_{visible} = E_{\bar{\nu}_e}$-0.782MeV. It is assumed that the detection efficiency is 100% and no background. Circle mark denotes the calculation result which is not consider neutrino oscillation, and square marker denotes the calculation result include the oscillation effect, here the oscillation parameters are treated as LMA solution parameters($\Delta m^2 = 2.0 \times 10^{-5}, \sin^2 2\theta = 0.7$). The event rate is about 486 events/year/600ton for no oscillation case and about 265 events/year/600ton for LMA oscillation case, respectively. Neutrino oscillation is observed not only from verification that the number of detected events is smaller than expected number of events but also from the shape of the energy spectrum will change. Figure 3.6 shows a ratio between

the number of observed events and that of expected events per 1MeV as a function of the visible energy. Error components are statistical error for observed and expected events only.

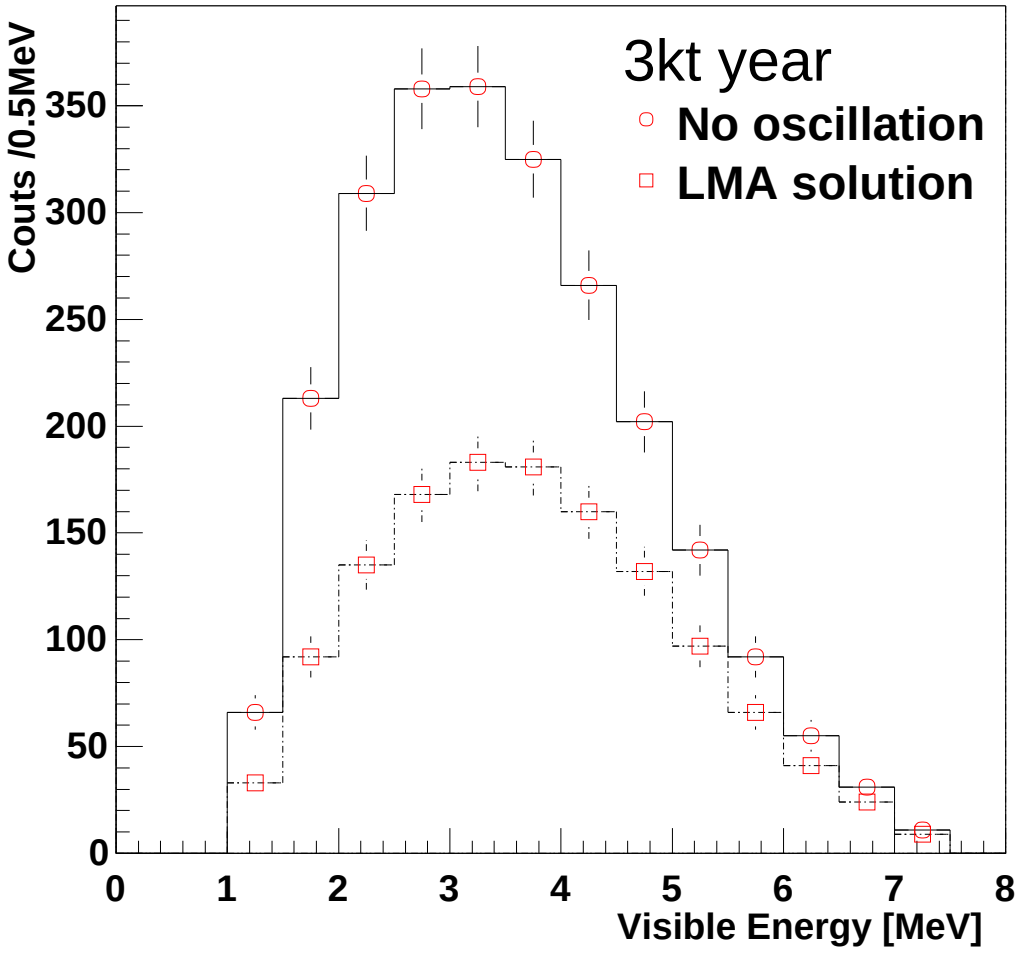

Figure 3.5: Visible energy spectra of anti-neutrino at KamLAND for 3kt·year statistics, here anti-neutrino flux is calculated results using the electricity output data of nuclear reactors between April 1997 and March 1998, and the cross section for the $\bar{\nu_e}$P$\rightarrow e^+$n interaction is lowest-order one. Visible energy denotes the detected energy of the prompt event in delayed coincidence event, $E_{visible} = E_{\bar{\nu}_e}$-0.782MeV. Circle marker denotes the calculation result which is not consider neutrino oscillation. Square marker denotes the calculation result include the oscillation effect, here the oscillation parameters are treated as LMA solution parameters($\Delta m^2 = 2.0 \times 10^{-5}, \sin^2 2\theta = 0.7$).

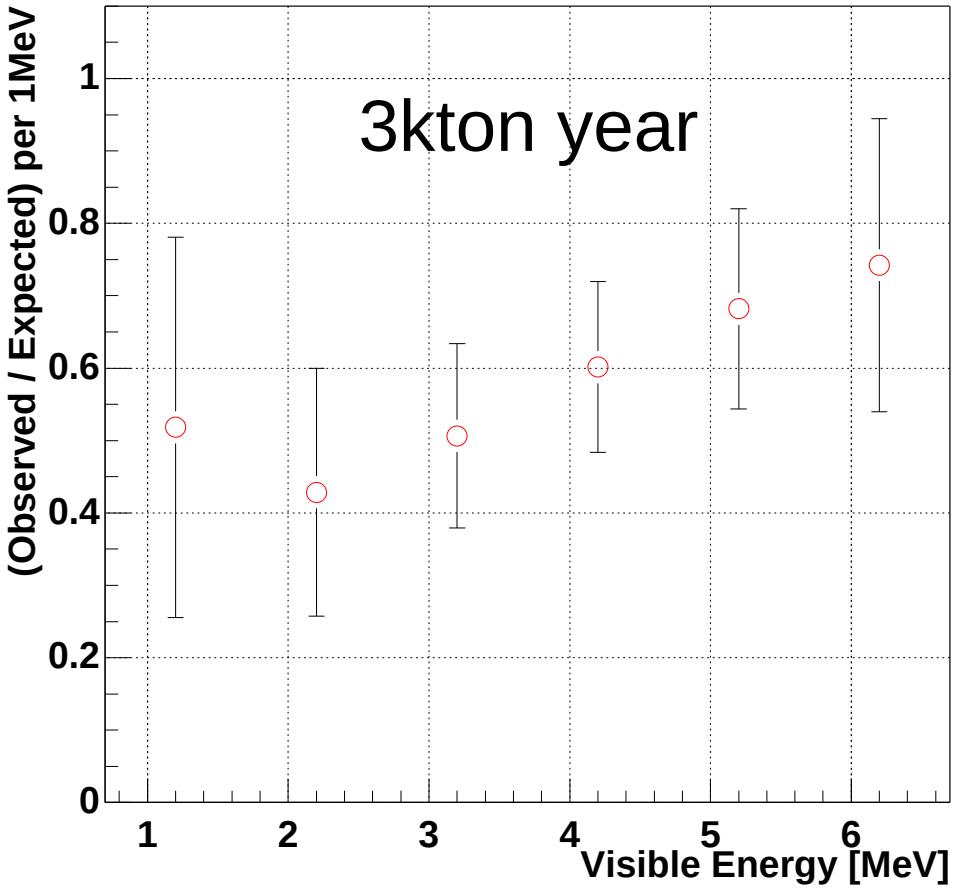

Figure 3.6: Energy spectrum of ratio between the number of observed events and the number of expected events. Neutrino oscillation can be observed from the variation of a shape of this energy spectrum. In this figure, it is assumed that oscillation parameters follow to the LMA solution, and the origin of error is only statistical error.

Seasonal Variation - Total Reactor Power Flux dependence of Nuclear Reactor -

Those analysis of above paragraph is not suitable if the backgrounds event rate is high. The reason is that separating background events from anti-neutrino candidate events completely is impossible. Therefore, it is important to operate the background free analysis and to estimate the number of background events. We can operate the background free oscillation analysis and estimate the background using this fluctuation.

Japanese reactors electricity output are change 20$\sim$ 30% between one year for the maintenance. Figure 3.7 shows the relation of the reactor power flux and number of event per month, here statistics is 3kt year. In this analysis method, the slope of the

number of events as a function of the power flux will change if neutrino oscillation is present in the LMA solution region. And an intercept at power flux is 0 denotes the number of background events. At this statistics, errors of intercepts are ± 28.5 events/month for both of no oscillation case and LMA solution case.

Expected Sensitivity for Oscillation Parameters

Assumed to a fiducial volume is 600ton and no background, KamLAND can examine the LMA solution region, $\Delta m^2 = 1.2 \times 10^{-5} \sim 10^{-4}[\mathrm{eV}^2]$ and $\sin^2 2\theta \geq 7.5$, at 90%C.L. for a half year. It will be reach at 99%C.L. for one year, and finally practical examined region is shown in Figure 3.8 at 99%C.L. for 5years(3kton year).

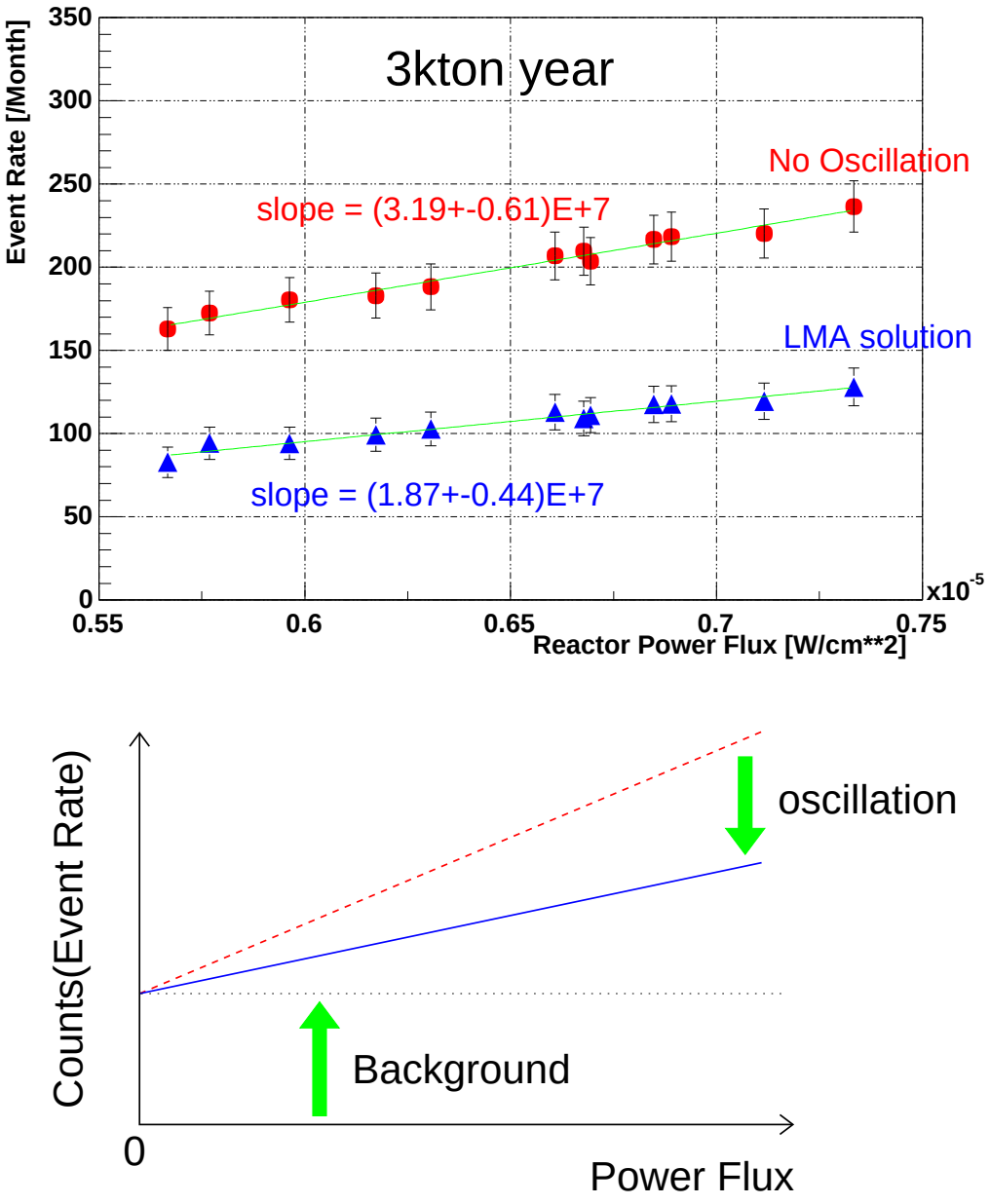

Figure 3.7: The rector power flux dependence of the number of anti-neutrino at KamLAND for 3kt year statistics, The circle marker denotes the calculation result which is not consider neutrino oscillation. The triangle marker denotes the calculation result include the oscillation effect, here the oscillation parameters are treated as LMA solution parameters($\Delta m^2 = 2.0 \times 10^{-5}, \sin^2 2\theta = 0.7$). We can operate the background free analys from the observation of a slope, event rate to power flux.

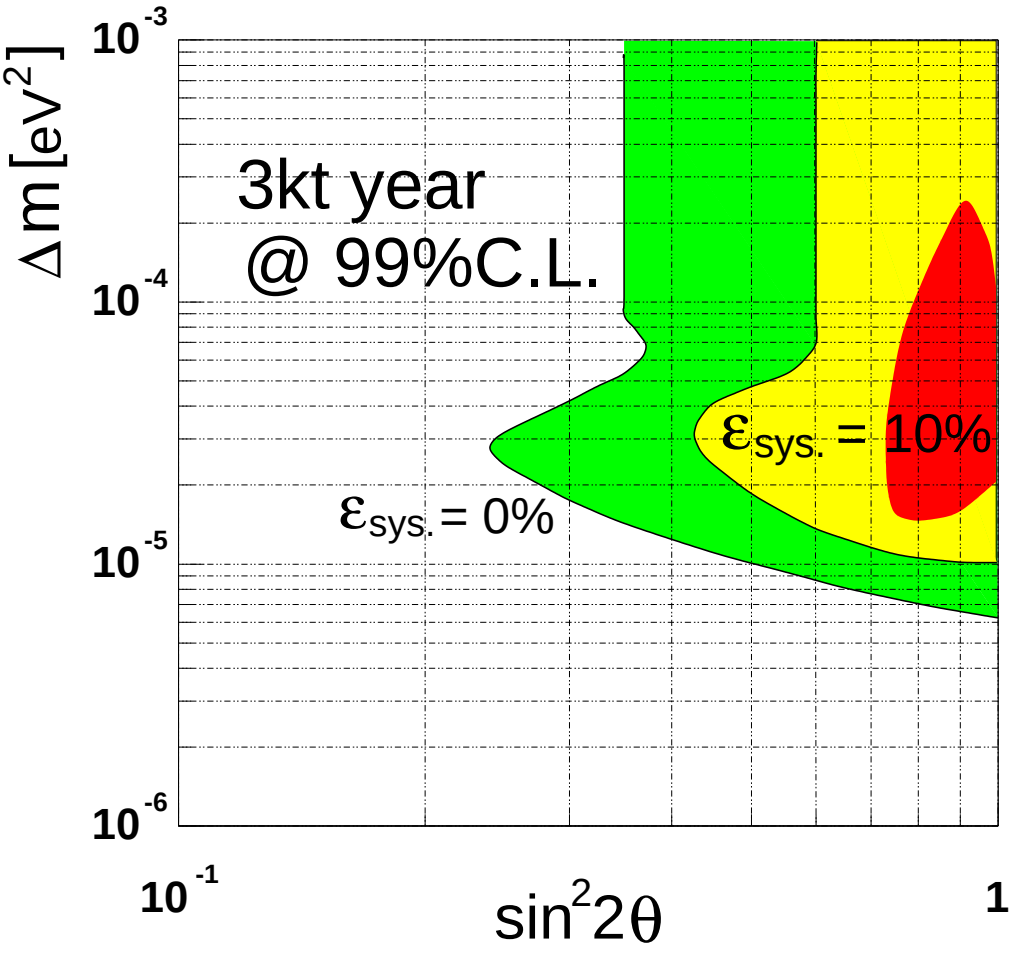

Figure 3.8: Expected sensitivity for oscillation parameters, Δm^2 and $\sin^2 2\theta$. Most inside region denotes LMA solution which implied many experimental results, and outer two regions denote sensitive region of KamLAND. Assumed to the systematic error is 0% and 10above region.

3.2 Solar Neutrino Detection and Oscillation Experiment

3.2.1 Solar Neutrino Observation at KamLAND

The nuclear fusion create solar energy. 98.5% of solar energy is derived from the pp-chain reactions and remaining 1.5% is created by CNO cycle reactions. Figure 3.9 shows all process of pp-chain. pp, pep, ^{7}Be, ^{8}B, and hep neutrinos are produced by these reactions. The flux of these neutrinos are shown in Figure 3.10. The main target of KamLAND is ^{7}Be neutrinos($5.15\times10^9/\mathrm{cm}^2/\mathrm{sec}^{-1}$),

$$^7\mathrm{Be} + \mathrm{e}^- \rightarrow {}^7\mathrm{Li} + \nu_e \ (90\%, E = 862\mathrm{keV}) \quad (3.2)$$

$$\rightarrow {}^7\mathrm{Li} + \nu_e + \gamma \ (10\%, E = 384\mathrm{keV}) \quad (3.3)$$

The recoil electron energy spectrum derived from ^{7}Be(862keV) neutrino interaction is continuous spectrum whose maximum energy is 665keV (Section 2.2).

Expected spectrum of solar neutrino and background as a function of the energy are shown in Figure 2.4. Assuming to the energy resolution is $10\%/\sqrt{E(MeV)}$, trigger threshold is determined at 280keV owing to the contamination of ^{14}C (Q_{β^-}=156.475keV).

Expected event rate of ^{7}Be neutrino at KamLAND is shown in Table3.1. It is assumed that background sources in the detector(U, Th, K, and Rn) are reduced to our aim, $\leq 10^{-16}$g/g for U/Th, $\leq 10^{-14}$g/g for K and $\leq 1\mu$Bq/m^3 for Rn. (Section 2.4.2).

Source	type	Rate(280-800keV) [counts/kt/day]	
		$\nu_e \rightarrow \nu_{\mu,\tau}$	$\nu_e \rightarrow \nu_s$
Solar ν_e	SSM	466	
	LOW	262	207
	SMA	98	2
Background	without S.S.	438	
	with S.S.	217	

Table 3.1: Event rates in the energy interval 280-800keV. S.S. denotes "Statistical Subtraction"2.4.2. ν_s denotssterile neutrinos

3.2.2 Oscillation Study using ^{7}Be Solar Neutrino

Figure 3.11 shows the relation of the solar neutrino and its survival probabilities at SMA solution, LMA solution, and LOW solution. **LMA** solution will be tested using **reactor anti-neutrino** at KamLAND directly.

Survival probability of SMA solution is nearly 0 at the ^{7}Be solar neutrino energy(862keV). So, the **SMA** solution can be recognized by essentially **null flux** of ^{7}Be neutrino. Expected event rates in the energy window, 280-800keV, are 98 events/kt/day for $\nu_e \to \nu_{\mu,\tau}$ oscillation and 2 events/kt/day for $\nu_e \to \nu_s$ oscillation.

For LOW solution, survival probability of night is much bigger than day's one at ^{7}Be energy, the difference between them is expected for $3\% \sim 50\%$. KamLAND can examine the **LOW** solution with a **day-night asymmetry**, this is the background free analysis.

At last, **VAC** solution is examined by observing **seasonal variation** of ^{7}Be solar neutrino event rate. This rate will change from 27 events/day to 124 events/day if the VAC solution is the correct solution.

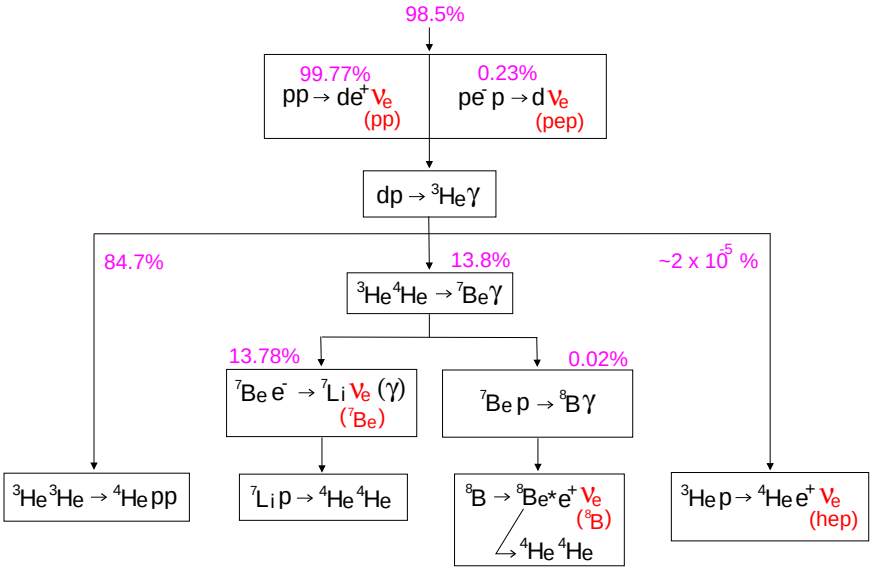

Figure 3.9: All nuclear fusion process of pp-chain. Four type neutrinos,pp, pep, ^{7}Be, ^{8}B, and hep, are produced in these reactions.

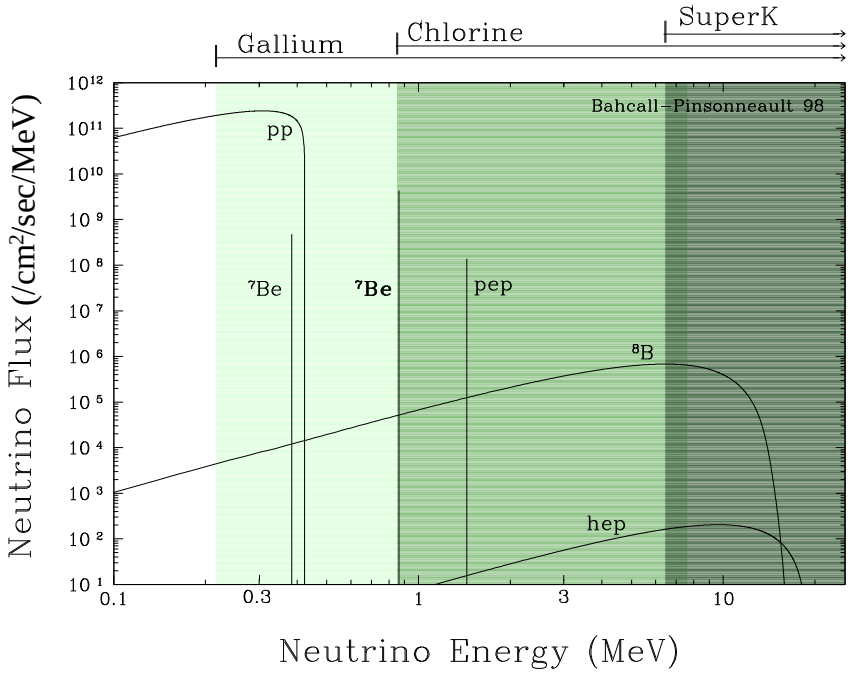

Figure 3.10: Solar neutrino flux which is calculated by J.Bahcall in 1998 based on the SSM. "Gallium", "Chlorine" and "SuperK" denote the sensitivity region of each experiment. KamLAND sensitivity region is same as the Chlorine experiment's one.

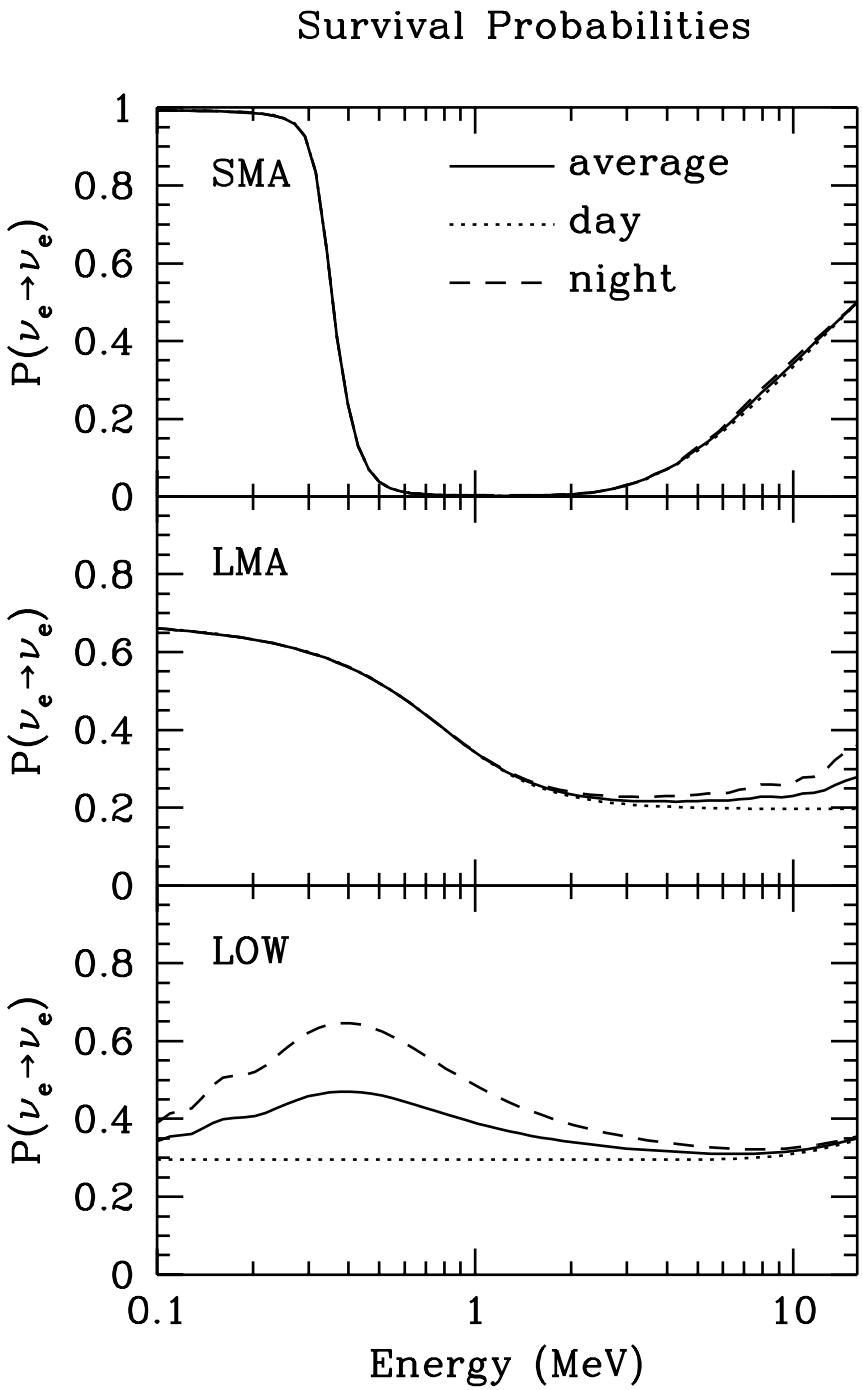

Figure 3.11: The energy dependence of the Solar neutrino survival probabilities which is calculated by the J.Bahcall. The survival means ν_e created in the sun to remain ν_e upon arrival at the KamLAND detector. The best-fit MSW solutions are computed including regeneration in the earth at night. The solid line refers to the one-year average survival probabilities computed taking into account regeneration in the earth. The dotted line refers to calculations for the day-time and the dashed line is the one-year average night-time survival probability (with regeneration).

3.3 Terrestrial Anti-Neutrino Detection

3.3.1 Terrestrial Anti-Neutrino

Earth emits the radiation heat about 16[TW]. The main source of this heat is the decay energy of radioactive elements, ^{238}U, ^{232}Th, and K. Anti-neutrinos are produced by β-decays in above decays. KamLAND can study the internal structure of the Earth with observing the this terrestrial anti-neutrinos. Figure 3.12 shows calculated flux of terrestrial anti-neutrinos(U, Th and K-decay series) based on the most popular terrestrial structure model(Table 3.2). There are several models about the terrestrial structure, and the absolute value of flux, U, Th and K-series, depend on each terrestrial model. Maybe, KamLAND will decide the correct terrestrial structure model through the terrestrial anti-neutrino observation.

Many characteristic edges can be noticed in these flux. KamLAND will detect these anti-neutrinos using the delayed coincidence technique, and the energy threshold is 1.8MeV. The energy of these edges are 3.3MeV(^{214}Bi-decay) and 2.3MeV(^{234}Pa-decay) in ^{238}U-decay series(E>1.8MeV), and 2.3MeV(^{212}Bi-decay) and 2.1MeV(^{228}Ac-decay) in ^{232}Th-decay series(E>1.8MeV). Furthermore, the rate of terrestrial anti-neutrino events at KamLAND is estimated 47events/year/600ton, and Figure 3.13 shows event rate spectrum as a function of a $\bar{\nu}_e$ energy. Terrestrial neutrinos are recognized benefit of these characteristic edges in the energy spectrum although the statistics is very small compared with the reactor anti-neutrinos. Figure 3.14 show $\bar{\nu}_e$ spectrum as a function of the visible energy. There are characteristic edges at about 1.5MeV and 2.5MeV.

3.3.2 Oscillation Study using Terrestrial Anti-Neutrino

The shapes of U-series and Th-series energy spectra do not change if the effect of the neutrino oscillation cannot be ignored, because each energy spectrum shapes do not depend on the terrestrial model. In other words, KamLAND can study the neutrino oscillation using the shape of the energy spectrum if we can know the ratio of two flux,

feature	thickness [km]	U abundance [ppm]	U intensity [Bq/m^3]	Th abundance [ppm]	Th intensity [Bq/m^3]
crust	35	0.91	9.23×10^3	3.50	1.16×10^4
mantle	2900	0.015	8.31×10^2	0.060	1.08×10^3
core	3500	0	0	0	0

Table 3.2: U/Th distribution of most popular terrestrial structure model

U-series and Th-series. In particularly, the ratio of the two edges at ∼2.3MeV and ∼3.3MeV will change if the region of Δm^2 is about $10^{-7.5} \sim 10^{-6} (\sin^2 2\theta = 1.0)$.

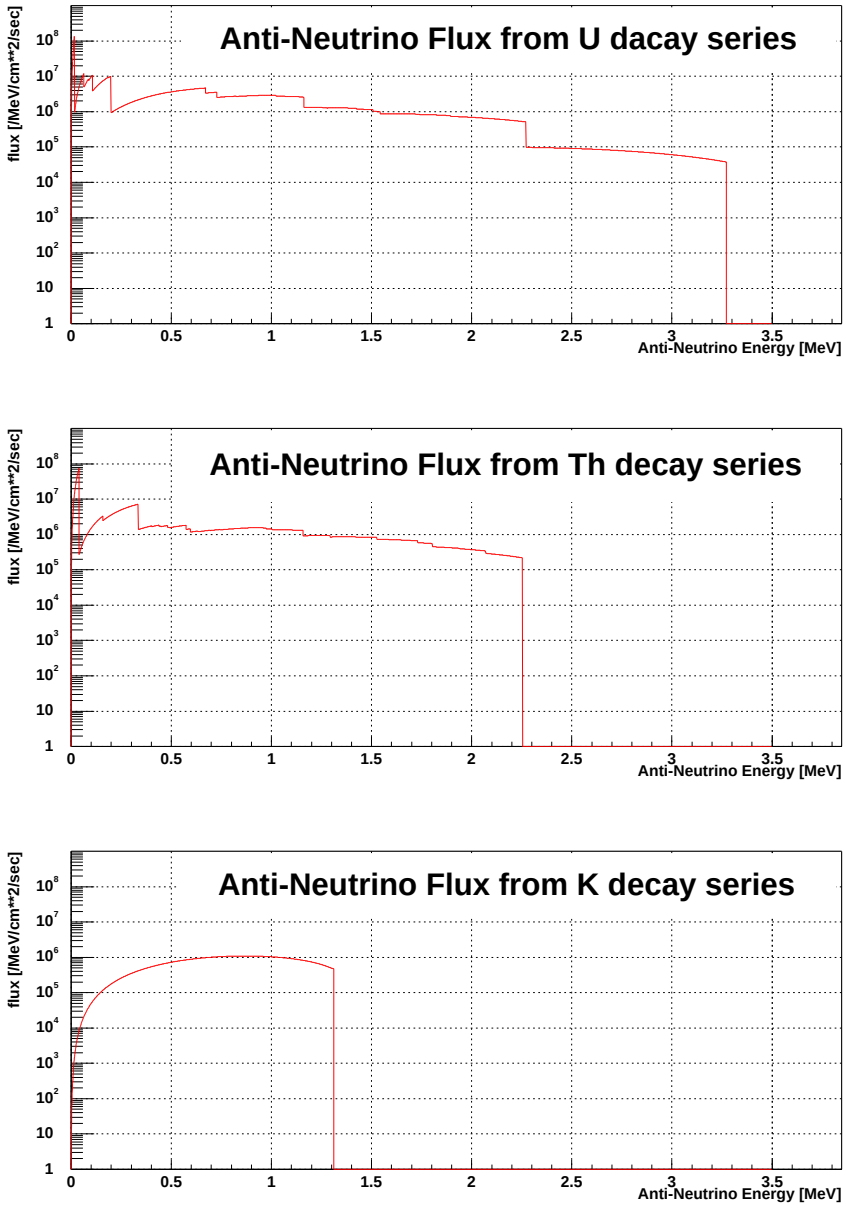

Figure 3.12: Terrestrial anti-neutrino flux from U, Th and K decay series. There are many characteristic edges. There are several models about the terrestrial structure, and the absolute value of two flux, U,Th and K-series depend on the terrestrial model. We can know the correct terrestrial model from the anti-neutrino observation.

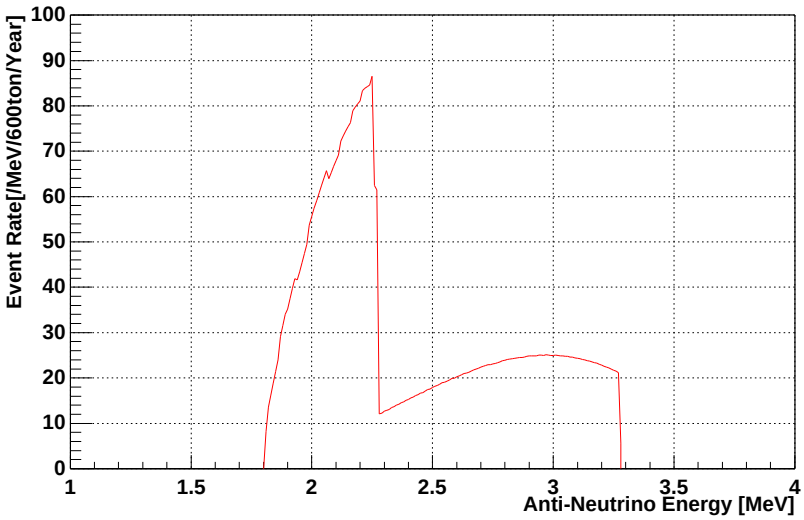

Figure 3.13: The energy spectrum of the terrestrial anti-neutrino for one year at KamLAND. It is assumed that the fiducial mass is 600 ton. The number of events for one year is estimated about 47events/year/600ton. There are two characteristic edges at about 2.1∼2.3MeV and 3.3MeV.

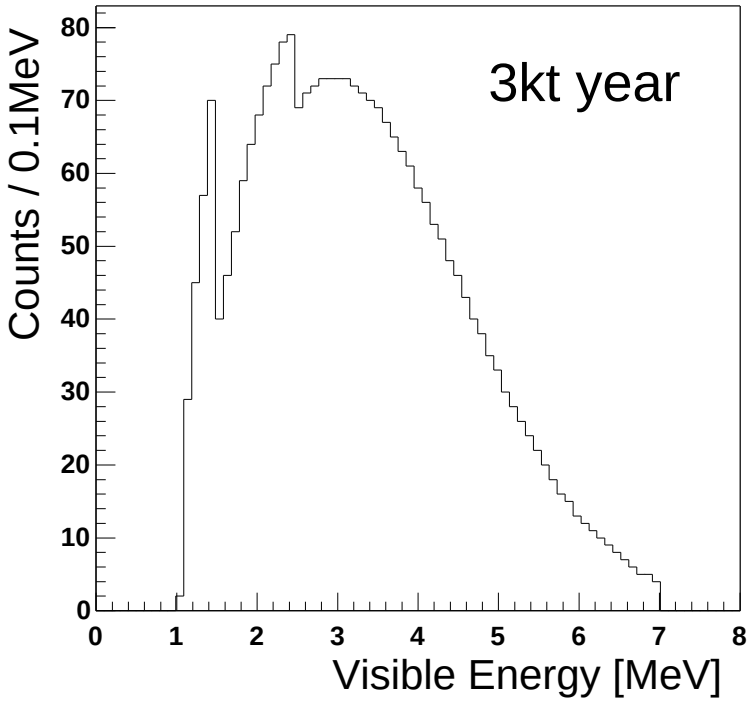

Figure 3.14: Visible energy spectrum of $\bar{\nu}_e$ from the terrestrial and Japanese reactors, statistics is 3kt year. Visible energy denotes the detected energy of the prompt event in delayed coincidence event, $E_{visible} = E_{\bar{\nu}_e}$-0.782MeV. The terrestrial neutrinos are recognized benefit of two characteristic edges, $E_{visible}$ ∼1.5 and 2.5MeV.

3.4 Supernova Detection

The KamLAND detector, containing a large amount of carbon, opens the possibility of detecting the scattering of ν and $\bar{\nu}$ from supernovae explosions on carbon nuclei.

With the standard supernova, type II(total energy release = 3×10^{53}erg; T(ν_e) = 3.5MeV, T($\bar{\nu}_e$) = 5.0MeV and T($\nu_{\mu,\tau}, \bar{\nu}_{\mu,\tau}$)), at the distance of 10kpc from the Earth, we arrive at the KamLAND count rate of,

$$N_\nu = \frac{35.3\langle\sigma\rangle}{T(\mathrm{MeV})} counts, \tag{3.4}$$

here, the thermally averaged cross section $\langle\sigma\rangle$ is in units of $10^{-42}\mathrm{cm}^2$ and the temperature is in MeV. We assume here that the detection efficiency is 100%.

Of particular interest for the supernova detection at KamLAND are the charged current reactions;

$$\text{Ⓐ} \quad \bar{\nu}_e p \rightarrow n e^+ \quad (E_{Th.} = 1.8\mathrm{MeV}, \tau \sim 175\mu\mathrm{sec.}) \tag{3.5}$$

$$\text{Ⓑ} \quad \nu_e {}^{12}C \rightarrow {}^{12}N e^- \quad (E_{Th.} = 17.3\mathrm{MeV}, T_{1/2} \sim 11.0\mathrm{msec.}, Q_{E.C.} = 17.3\mathrm{MeV}) \tag{3.6}$$

$$\text{Ⓒ} \quad \bar{\nu}_e {}^{12}C \rightarrow {}^{12}B e^+ \quad (E_{Th.} = 14.4\mathrm{MeV}, T_{1/2} \sim 20.4\mathrm{msec.}, Q_\beta = 13.4\mathrm{MeV}) \tag{3.7}$$

and the neutral current reactions;

$$\text{Ⓓ} \quad \nu_x(\bar{\nu}_x) {}^{12}C \rightarrow {}^{12}C^* \nu_x(\bar{\nu}_x) \quad (E_{Th.} = 15.11\mathrm{MeV}) \tag{3.8}$$

$${}^{12}C^* \rightarrow {}^{12}C\gamma(15.11\mathrm{MeV}) \tag{3.9}$$

populating the 15.11MeV state in ${}^{12}C$. Here, x denotes e, μ and τ, and details are described in 2.3. The signal for these exclusive reactions will be essentially background free due to the possibility of observing the delayed coincidence of the charged current reactions and the sharp peak at 15.11MeV for the neutral current reaction.

The expected number of events is shown in Table3.3. The first line gives the number of events expected without effects of neutrino oscillation. Next two lines give the expected number of events when oscillations are present, vacuum oscillation and MSW oscillations. When vacuum solution is correct, charged current reactions Ⓐ, Ⓑ and Ⓒ will increase because of $\nu_\mu(\bar{\nu}_\mu) \rightarrow \nu_e(\bar{\nu}_e)$ oscillation. For MSW solution, only reaction Ⓑ will be increase because of $\nu_\mu \rightarrow \nu_e$ oscillation with matter effect.

Compared the number of events of Ⓑ+Ⓒ from that of Ⓓ, we will know that the oscillations are present. It will be very difficult to distinguish the reaction Ⓑ and Ⓒ, however we will know vacuum oscillation or MSW by comparing the number of events, Ⓐ, Ⓑ+Ⓒ and Ⓓ

	Ⓐ $\bar{\nu}_e p \to n e^+$	Ⓑ $\nu_e^{12}\mathrm{C} \to {}^{12}\mathrm{N} e^-$	Ⓒ $\bar{\nu}_e^{12}\mathrm{C} \to {}^{12}\mathrm{B} e^+$	Ⓓ $\nu_x(\bar{\nu}_x)^{12}\mathrm{C} \to {}^{12}\mathrm{C}^* \nu_x(\bar{\nu}_x)$
no osc.	330	1.9	7.4	57.6
vacuum osc.	~ 600	14.5	13.8	57.6
MSW osc.	330	27	7.4	57.6

Table 3.3: Expected number of events in KamLAND for supernova neutrinos scattering on carbon and proton.

3.5 Anti-Neutrinos from the Sun and Past Supernovae

KamLAND will be the first large detector capable of identifying electron-anti-neutrinos from extra-terrestrial sources with very small backgrounds, hence opening an entirely new window for the exploration of unknown phenomena. The delayed coincidence technique used by KamLAND to identify $\bar{\nu}_e$ provides a very effective background rejection, so that the expected background due to muon-produced neutrons and γ-rays from natural radioactivity and cosmogenic isotopes will amount to less than 0.1event/day($\sim$37events/year) above 8MeV. Below 8MeV the reactor and terrestrial neutrinos will dominate, and below 30MeV atmospheric anti-neutrino will be negligible(several events per year). Therefore, following two anti-neutrinos will search in the energy window $8 \sim 30$MeV. Basically, we cannot discriminate such two anti-neutrinos, however it is very surprising incident that anti-neutrinos will be detect in this energy window.

One possible source of $\bar{\nu}_e$ is the Sun. There is little possibility of the transition $\nu_e \rightarrow \bar{\nu}_\mu \rightarrow \bar{\nu}_e$ if electron-neutrino has the magnetic moment. $\nu_e \rightarrow \bar{\nu}_\mu$ transitions, resonant spin flavor rotation, is due to the interaction with the magnetic field of the Sun, and $\bar{\nu}_\mu \rightarrow \bar{\nu}_e$ transitions are derived from neutrino oscillation between the Earth and Sun, vacuum oscillation. The upper limit on the anti-neutrino flux above 8.3MeV is $9\times10^4 \mathrm{cm}^{-2}\mathrm{sec}^{-1}$(@95%CL)which is about 1% of the solar neutrino flux. Such flux would produce in KamLAND a clear signal of $\sim$900events/year in the region above 8.3MeV, hence in one year we could put a 95%CL upper limit on the anti-neutrino flux of $3\times10^3 \mathrm{cm}^{-2}\mathrm{sec}^{-1}$, or 0.1% of the flux of neutrinos from the sum.

Another possible source of anti-neutrinos could be given by the past supernovae. Such catastrophic events produced ν and $\bar{\nu}$ that accumulated in the universe. Because of the red shift, the energy spectrum carries information on the time distribution of large collapses during the history of our universe. We would expect to detect about 40events/year within above energy window following to one of the standard models.

3.6 Required Features for the Detector

The main target of KamLAND experiment is the examination of LMA solution using low energy(1.8∼8MeV) electron-anti-neutrino from Japanese nuclear reactors which described in the Section 3.1. Anti-neutrinos will be detect using the delayed coincidence technique, so the energy threshold for this type neutrinos detection is 1.8MeV(Section 2.1). In this energy range, another anti-neutrino, terrestrial anti-neutrino, will be detected as described in the Section 3.3. The terrestrial anti-neutrino detection is also important subject of KamLAND, and the energy of this is less than about 3.3MeV. Moreover, ^{7}Be solar neutrino(862keV) observation is also important target of KamLAND experiment for the exploration of SMA, LOW and VAC solution. The kinematic energy of recoil electron is less than 665keV. To achieve these neutrinos detection, required features for the detector are;

- Large size for high statistics
- Very sensitive at above a few keV energy
- High energy resolution at least $\delta E/E = 10\%/\sqrt{E(MeV)}$ (100 p.e./MeV)
- Very very low background
- High flash point for safty(>60°C)

The most simple method of an observation for neutrino oscillation is verify a number of detected neutrino is smaller than expected number. High statistics and high sensitivity are important feature to decrease statistical and systematic error. In following section3.6.1, it is described the reason why high energy resolution is required Low background environment and capability of background suppression are proper requirement to decrease the systematic error.

The liquid scintillator satisfy above features, this is very sensitive at the energy range above a few hundred keV and that the contamination of radioactive sources which are the background sources are very low. Moreover, the underground site, the multiple layers structure of KamLAND and its purification system are very effective to suppress the background. In addition, time response of the liquid scintillator and PMT is very good, so that the dead time of KamLAND will be very short.

3.6.1 Necessity of High Energy Resolution

At the early stage of the experiment, purification will not not enough. Radioactive impurities in the scintillator will be 10^{-14}g/g for U/Th, 10^{-12}g/g for K and 500mBq/m^3

for Rn when experiment start. In case of this, background for delayed coincidence signal($\bar{\nu}_e signal$) may be serious. At the following condition to select $\bar{\nu}_e$ events,

- E_{prompt} $\geq$1MeV
- 1.85MeV$\leq$ $E_{delayed}$ $\leq$2.59MeV
- $|V(x,y,z)_{prompt} - V(x,y,z)_{delayed}|$ $\leq$1m
- $10\mu\text{sec} \leq T_{delayed} - T_{prompt} \leq 500\mu\text{sec}$
- a misidentification probability α against β, γ is 10%
- α-quenching factor is 13.8

accidental background rate and correlate background rate are estimated 0.17 events/kt/day and 0.006 events/kt/day, respectively. Percentage of background rate to reactor $\bar{\nu}_e$ event rate(2 events/kt/day; no oscillation) and terrestrial $\bar{\nu}_e$ event rate(0.2 events/kt/day) are 9% and 85%, respectively. Background rate will be reduced at the narrow delayed signal window. However detection efficiency of the delayed signal(2.2MeV γ-ray) will be reduced if energy resolution is unsatisfactory. At resolution $\delta E/E = 10\%\sqrt{E(MeV)}$ and $14\%\sqrt{E(MeV)}$, the detection efficiency of delayed signal are 99% and 92%, respectively(1.85MeV$\leq$ $E_{delayed}$ $\leq$2.59MeV). And, it is also easy to recognize the change of the energy spectrum following to the neutrino oscillation as the good energy resolution.

Even if radioactive impurities are reduced at our aim, U/Th$\leq$ 10^{-16}g/g, K$\leq$ 10^{-14}g/g and Rn$\leq$ 1μBq/m^3, high energy resolution is very important, especially ^{7}Be solar neutrino detection. The energy window for ^{7}Be neutrino observation is decided by contamination of ^{11}C(visible energy 1.02-2.49MeV) and ^{14}C(visible energy $\leq$156.475keV). We want to expand the energy window for high statistics, expected event rate of ^{7}Be neutrino is 466 events/kt/day(SSM) in the energy interval 280-800keV. At 280keV, S/N ratio(Signal to Noise) of ^{7}Be neutrino and ^{14}C is about 1 at energy resolution $\delta E/E = 10\%\sqrt{E(MeV)}$.

Additionally, terrestrial anti-neutrinos are recognized from characteristic edges, especially $\sim$1.5MeV and $\sim$2.5MeV(visible energy). These edges will be dull by the energy resolution, so it is not easy to recognize terrestrial anti-neutrino because of low flux. These edges become more sharp as the energy resolution become good.

In summary, we can study various physics which described in this chapter until good detector, the energy resolution and S/N is high, is accomplished. Observed energy is proportional to number of detected photons, light yield, and the energy resolution is depends on the light yield. High light yield is achieved until we use good scintillator

whose light-output(number of output photon) and attenuation length are good, or expands surface coverage of PMTs(use many PMTs). Expands PMT coverage is limited because of cost. So development of the scintillator whose light yield is high at the geometry of KamLAND is very important and essential. In following chapters, we describe the development of liquid scintillator for KamLAND.

Chapter 4

Measurement of the Light Attenuation-Length of the KamLAND Liquid Scintillator

KamLAND is a very large scintillation detector, diameter of the scintillator vessel is 13m, therefore the light attenuation length of the scintillator is crucial to the experiment. In this chapter, measurement of light attenuation length of the scintillator is described.

At first, overview of another measurements for the scintillator development, misidentification probability, light-output and emission spectrum are also described. Next measurement apparatus of the attenuation length and results are described.

These measurement are applied to a study of light yield[p.e./MeV] estimation. Calculation of the light yield at KamLAND requires several parameter(emission spectrum, quantum efficiency, coverage, balloon transparency) other than the attenuation length, so this calculation has several uncertainty. More strict estimation is postponed to the Chapter5.

From above measurements and calculations, we decide components and rough concentrations of KamLAND scintillator;

$$\text{Paraffin Oil}(80\%) + \text{P.C.}(20\%) + \text{PPO}(1\sim 2\text{g/l})$$

The attenuation length of this is 7.6m at 406nm of wavelength, and calculated light yields for central events and average inside the fiducial volume ($R \leq$5.5m) are 158p.e./MeV and 190p.e./MeV, respectively.

4.1 Selection of the Components of the Liquid Scintillator

In order to achieve high energy resolution and low background at KamLAND, light yield, purity and capability of a PSD is essential for the scintillator. The light yield depends on light output(number of output photons), light transparency of the scintillator, balloon, buffer oil, acrylic plate and photo-sensitive area, quantum efficiency and collection efficiency of PMT dynodes.

From the point of transparency of the scintillator, paraffin oil has been chosen for a base liquid instead of Pseudocumen(P.C.; 1,2,4-Trimethyl Benzene) which is the most popular solvent for small detectors but has relatively worse transparency than paraffin oil. Figure4.1 show the wavelength dependence of transparency of the paraffin oil and P.C., the thickness of two samples are 9cm. These spectra was measured by a light absorption meter(Figure4.2). Transparency is defined as the intensity ratio of two light, pass through object cell(10cm) and reference cell(1cm). However, P.C. is necessary to keep light output and capability of a PSD sufficiently high. Mixture of paraffin oil and P.C. is tested as a solvent, and optimum ratio has been surveyed.

On the other hand, the liquid scintillator consists of a few solvent and a few solute. Traditionally, two solutes, primary solute and secondary solute, are added in solvents. For primary solute, PPO(2,5-diphenyloxazole) is selected because it has been used at many experiments[2, 15, 3] and cost performance. The secondary solute plays a part of the wavelength shifter, the concentration of this solute is about 0.1g/l order. Because of this low concentration, performance as scintillator(light output and PSD) does not depend on the type of wavelength shifter. Wavelength shifter absorbs the scintillation light from the primary solute and emits the scintillation light whose wavelength is more longer. We considered BisMSB as a wavelength shifter because of cost performance. Light emission spectra of PPO and BisMSB are shown in Figure4.3. The emission spectrum is measured by a spectrophotometer, and schema meter is shown in Figure4.4.

Figure4.5 shows the apparatus of a misidentification probability(neutron against γ) measurement, here misidentification probability(Miss ID) denotes the percentage the neutron event is identified as γ-ray event. The scintillation light is emitted by neutron($\langle E_n \rangle$=2.14MeV) and γ-ray(<1MeV) from ^{252}Cf, and scintillation light is detected by 2"PMT. Tail charge and total charge of these scintillation light are measured by charge sensitive ADC. Pulse shape of the scintillation light from γ, β-ray is different from that of neutron, α. The decay time of heavy particles(neutron, α) is longer than that of light particles(γ, β). So the ratio of tail-charge/total-charge of light particle is less than that of heavy particle(Figure4.6). Figure4.7 and Figure4.8 show a misidenti-

fication probability as a function of P.C. and PPO concentration, respectively. At the measurement of the P.C. dependence, we used only PPO as a solute of the scintillator(concentration is fixed at 2g/l.). When the BisMSB(0.1g/l) was added in the scintillator, both of results are consistent within 1%. It is to be desired that Miss ID is less than 10% because we want to examine the LMA solution, $\Delta m^2 \sim 2\times10^{-5}, \sin^2 2\theta \sim 0.7$. We can explore the neutrino oscillation at the $\sin^2 2\theta > 0.1$ region if error of the flux measurement is less than 10%. From this request, P.C. is need at least 20% and PPO is at least 1g/l.

The light output measurement apparatus is shown in Figure4.9. Scintillators emit the light from recoil electron which is scattered by γ-ray from ^{60}Co, and this scintillation light is detected by 2"PMT. Light output of scintillators is compared using the ADC value of the compton edge. The measurement result as a function of PPO concentration is shown in Figure4.10, here the concentration of P.C. is fixed at 20%. The measurement result when the BisMSB(0.1g/l) was added in the scintillator is also consistent within 1%. The light output saturates at more than 2g/l of PPO. By the way, the light yield will be worse when PPO concentration is too much because of its self-absorption, especially at the large size detector, and it turn out that necessary concentration of PPO is 2g/l or less.

In summary, from the measurement of a misidentification probability, P.C. and PPO are necessary at least 20% and 1g/l, respectively. Suitable PPO concentration is 2g/l or less result from the light output measurement. When BisMSB is added in the scintillator at these measurements, results are consistent within 1%. We didn't know from these results which is the good scintillator adding BisMSB one or not adding one. Finally, both of results at light output and misidentification probability measurements give components and their concentration of the KamLAND scintillator;

Paraffin Oil(80%) + P.C.(20%) + PPO(1∼2g/l)

or

Paraffin Oil(80%) + P.C.(20%) + PPO(1∼2g/l) + BisMSB(0.1g/l)

From measurement results using a absorption meter(Figure4.11), it is estimated that transparencies of above two scintillators are satisfied at the size of KamLAND. However, the transparency is much influential at the large size detector, KamLAND, we measure the light attenuation-length more accurately with long light path($1 \sim 3$m). This apparatus and measurement results are described in following sections.

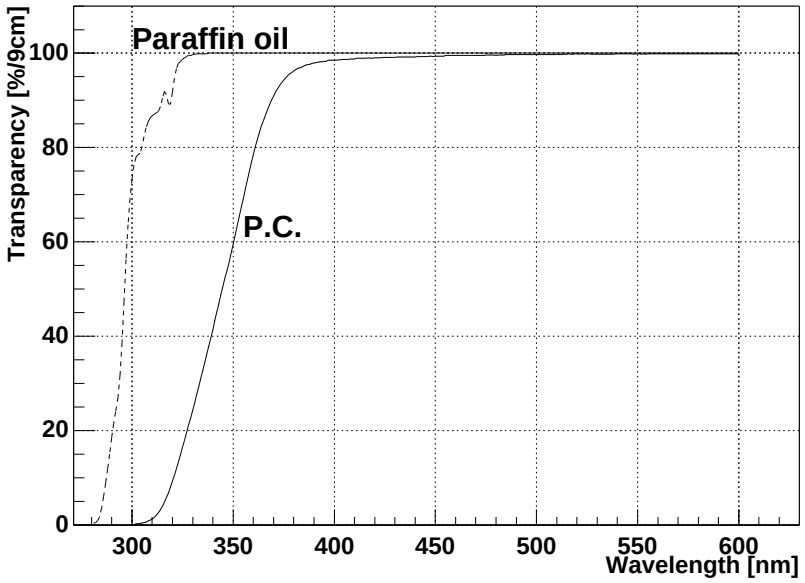

Figure 4.1: Light transparency spectrum of paraffin oil and P.C.. The transparency denotes the ratio(%) of tow attenuated light, the input light is attenuated by the solvents whose thickness are 1cm and 10cm. The horizontal axis denotes the wavelength of the input light. Solid-line denotes the transparency of P.C. and dot-line denotes paraffin-oil's one. At less than 400nm(wavelength) range, transparency of the paraffin-oil is much better than P.C.'s one.

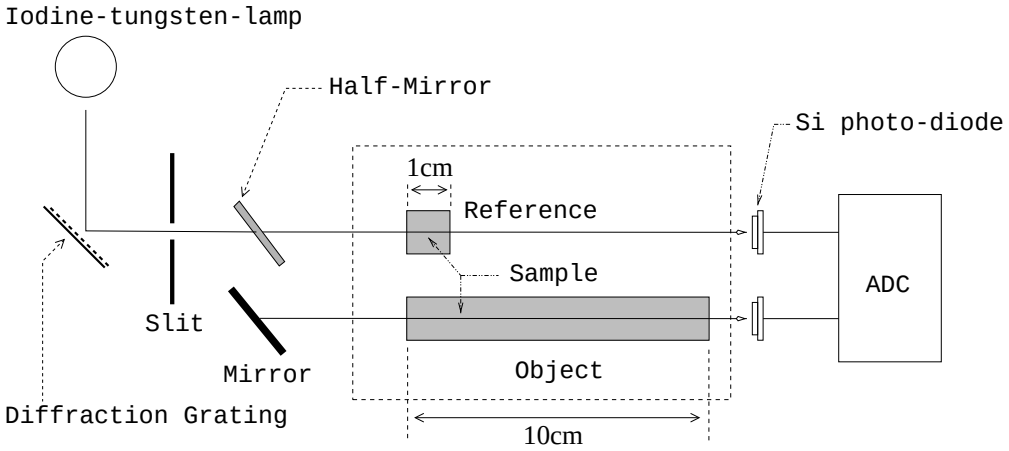

Figure 4.2: This is the Light absorption meter, U2000F(HITACHI). The light emitted from the tungsten-lamp is divided to two light, one light pass through the 1cm reference cell filled with sample and another light pass through the 10cm object cell. Intensity of two lights are measured by photo-diodes. Transparency is defined as the ration of these intensity.

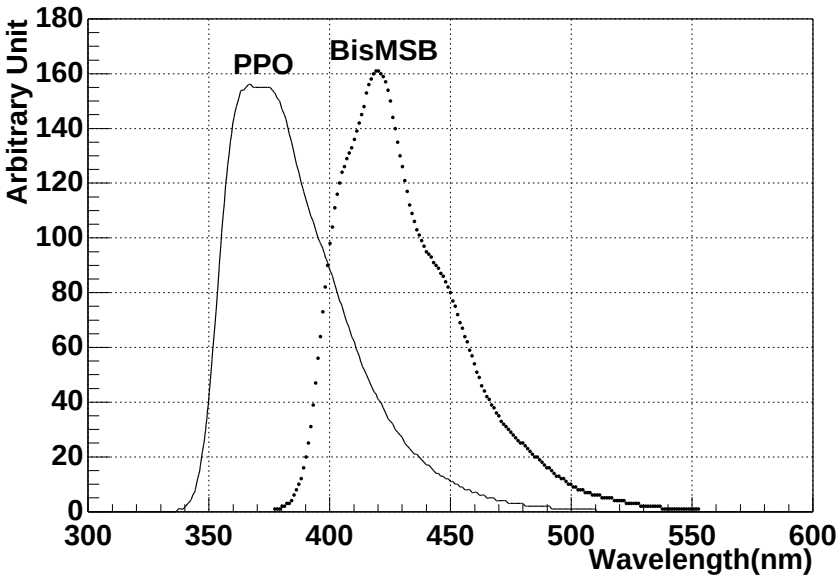

Figure 4.3: Light emission spectra of PPO and BisMSB. The horizontal axis denotes the wavelength of the emission light(scintillation light). The peak wavelength is about 375nm and 420nm, respectively. The wavelength of the scintillation light of BisMSB is longer than that of PPO.

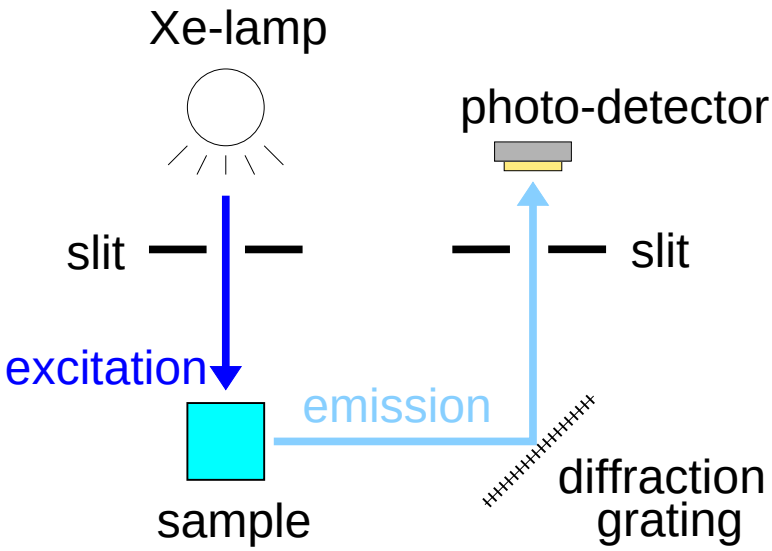

Figure 4.4: This figure is the spectrophotometer. The light source is the Xe-lamp, and it is narrowed the wavelength at 300nm. Sample scintillators are excited by this light, and emit the scintillation light. Intensity of this scintillation light is measured by the photo-detector, here detected light is narrowed the wavelength by the diffraction grating. This narrowed wavelength is regulated by this grating.

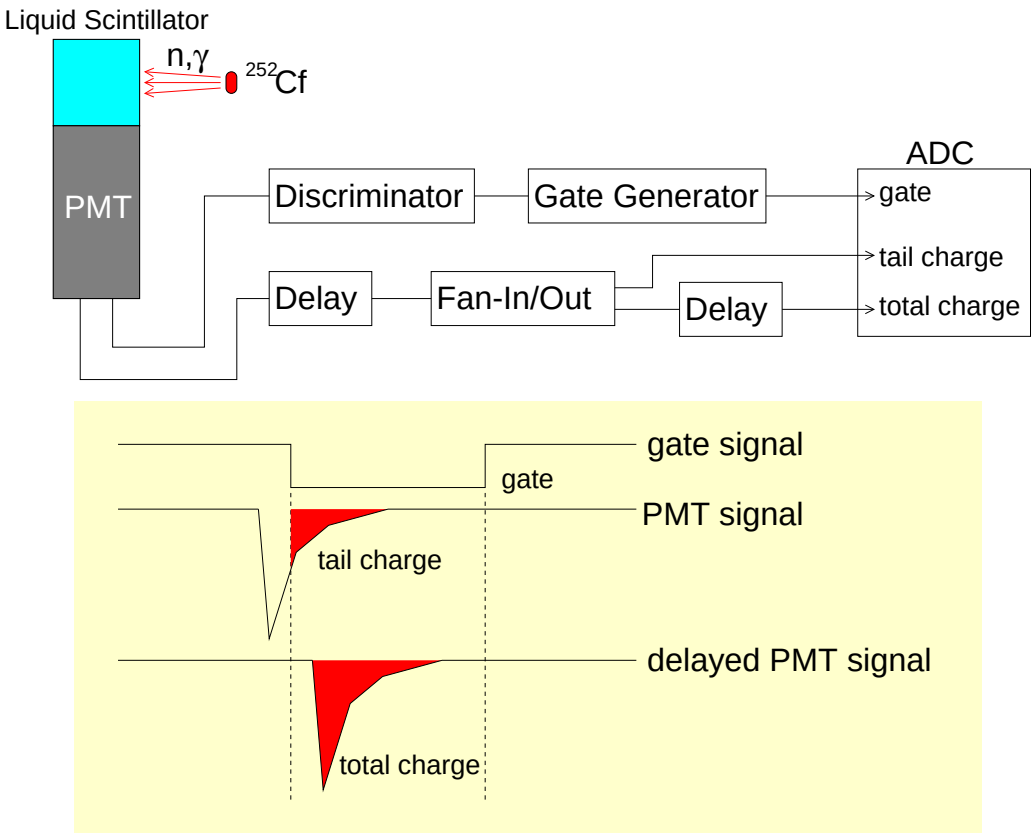

Figure 4.5: Tail charge and total charge of the scintillation light by ^{252}Cf(neutron($\langle E_n \rangle$=2.14MeV) and γ-ray(<1MeV)) are measured.

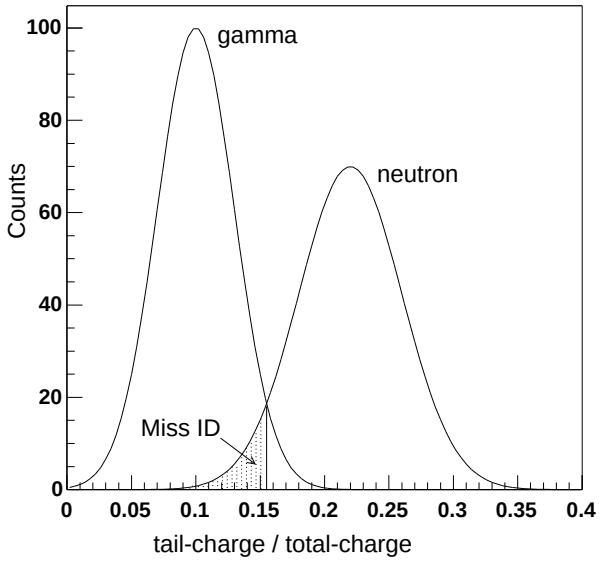

Figure 4.6: The definition of the Miss ID. The decay time derived from heavy particles(neutron, α) is longer than that from light particles(γ, β). So the ratio of tail-charge/total-charge of light particle is less than that of heavy particle. Miss ID denotes the percentage the neutron(heavy particle) event is identified as γ-ray(light particle) event.

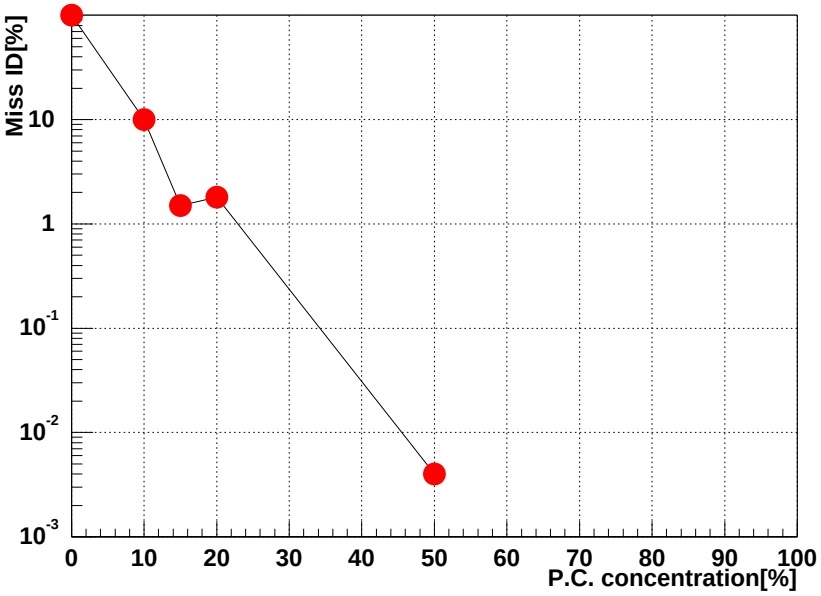

Figure 4.7: P.C. concentration dependence of the PSD efficiency. Miss ID denotes the percentage the neutron event is identified as γ-ray event, PSD efficiency is better as Miss ID become small. PSD is better as P.C. concentration become high.

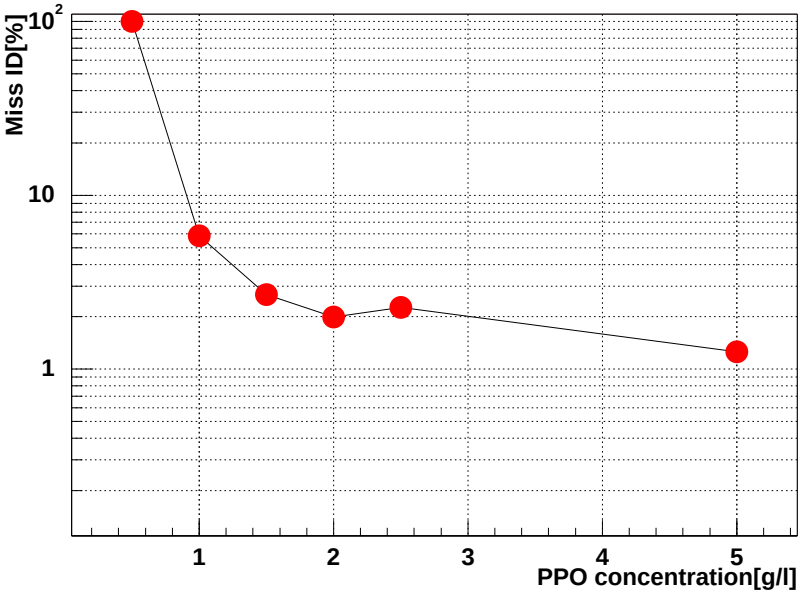

Figure 4.8: PPO concentration dependence of the PSD efficiency. PSD efficiency almost unchanged when PPO concentration is bigger than 1g/l.

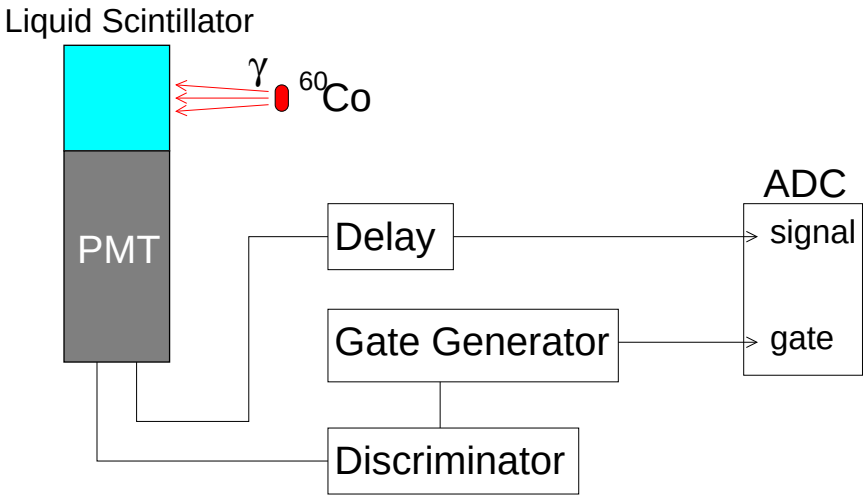

Figure 4.9: This is the light output measurement setup. Scintillators emit the light by recoil electron which is scattered by γ-ray from ^{60}Co(1.17, 1.33MeV), and this scintillation light is detected by 2"PMT, and the light output is measured by ADC. Light output of scintillators is compared using the compton edge. The measurement error is 7%(1σ).

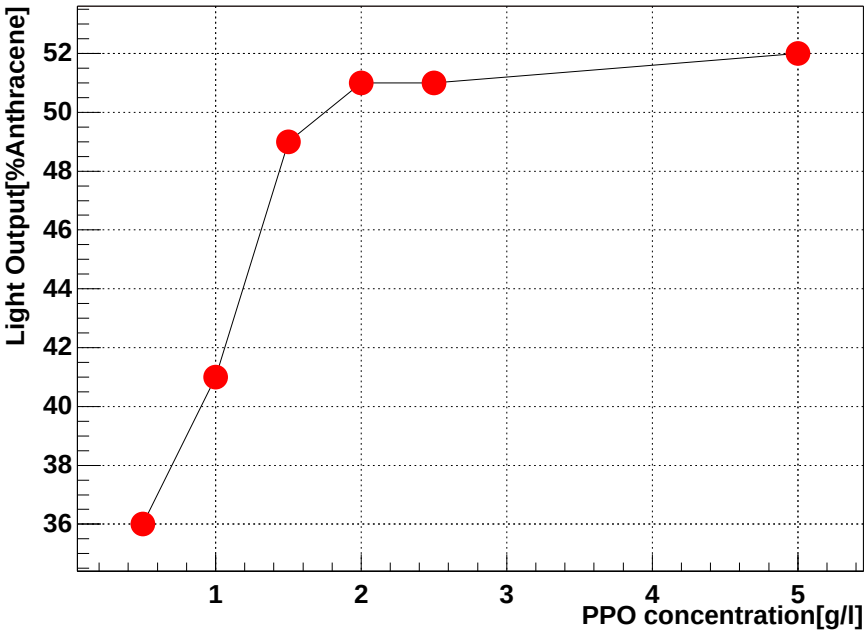

Figure 4.10: PPO concentration dependence of the light output. The light output is saturated at 2g/l.

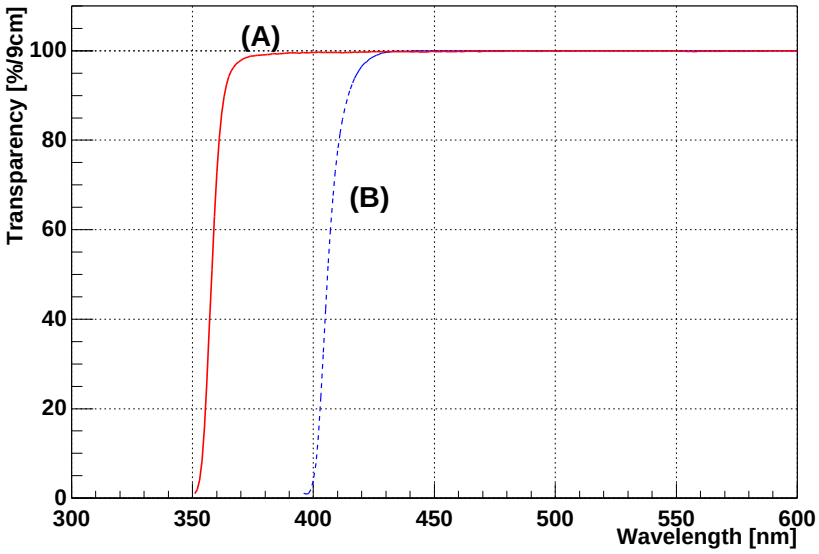

Figure 4.11: Light transparency spectrum of two scintillators. The transparency denotes the ratio(%) of tow attenuated light, the input light is attenuated by the solvents whose thickness are 1cm and 10cm. The horizontal axis denotes the wavelength of the input light. Solid-line denotes the transparency of the scintillator (A): Paraffin Oil(80%) + P.C.(20%) + PPO(2g/l), and dot-line denotes the transparency of another scintillator (B): Paraffin Oil(80%) + P.C.(20%) + PPO(1∼2g/l) + BisMSB(0.1g/l), At less than 400nm(wavelength) range, (B) is not transparent because of the absorption of BisMSB.

4.2 Apparatus

Light attenuation length was measured using the setup shown in Figure4.12. The light source is a N_2/Dye-laser, and wavelength of the laser light can be change using various dyes.We measure the light intensities after transimition through long and short tubes, $I(L)$ and $i(l)$, simultaneously. $I(L)$ is the light intensity which passes through the liquid scintillator in the long tube(light path = 2.75m) and $i(l)$ is the light intensity which passes through the scintillator in the short tube(light path = 1m).

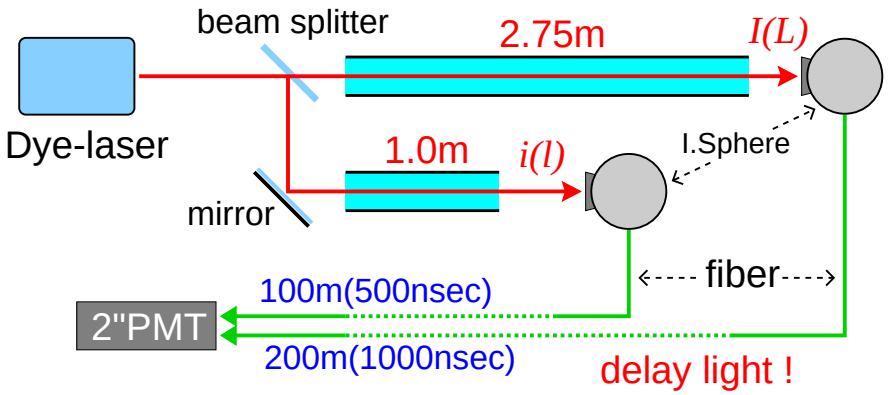

Figure 4.12: Setup of the system of measurement. The laser beam is divided into two beams using the beam splitter, and divided beams pass through each tubes(the length are 2.75m and 1.0m) which are filled with the liquid scintillator. Moreover, two beams are delayed(500nsec and 1,000nsec) by using optical fibers to avoid the noise which is emitted from the laser, and these beams are detected by only **one** PMT to avoid the unstaility of the PMT.

A noise is emitted from the laser system when the laser-light is emitted. In order to avoid a noise related to laser pulse emission, long optical fibers(core $\phi = 200\mu$m) are used as delay lines. Their length are 100m and 200m, providing 500nsec and 1,000nsec(1μsec) which is enough time to separate the noise from signals(Figure4.13).

Integrating spheres and ND-filters are used so that the light intensity is weakened to the level manageable with the 2inch PMT. Instability of the PMT gain is serious problem for the measurement if we use two or more PMT, thus we use only one PMT to measure both two light intensities. The schematics to measure two light intensities by single PMT is shown in Figure4.14.

Laser output is influenced on the flow rate of the nitrogen gas, dye condition and so on. In Figure4.15, left-side two histograms denote light intensities of two beams, $I(L)$ and $i(l)$. The hatched one is for $I(L)$ and another for $i(l)$, and upper and lower were measured in different period. In spite of the large drift of each intensities caused by laser

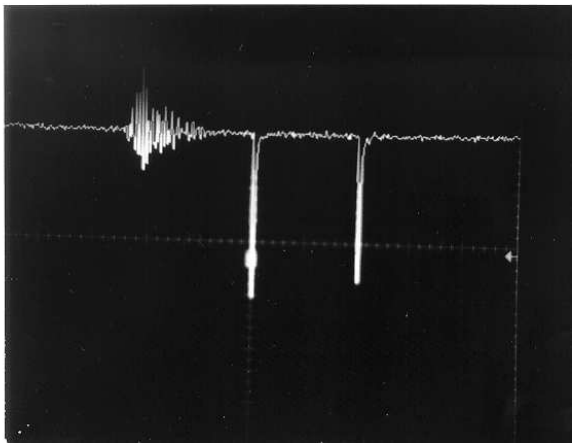

Figure 4.13: PMT signal on the oscilloscope. To separate the noise from laser signals, two light are delayed by using the optical fibers. One light is delayed by 500nsec, another is by 1,000nsec(1μsec).

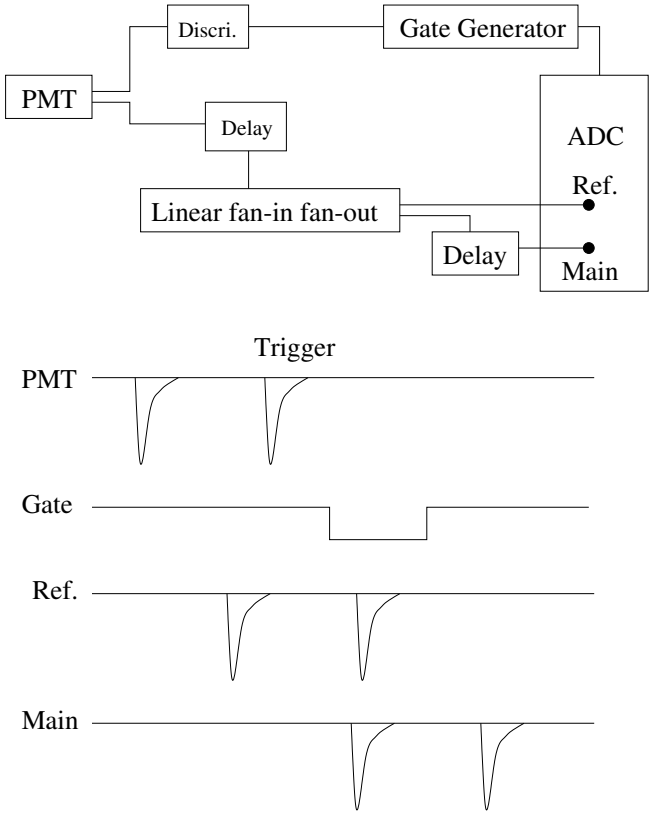

Figure 4.14: Logical setup of this measurement is shown in this figure. To measure the two signal from **one** PMT, one signal is delayed more than another and measure both two pulse.

instability, the ratio $R = I/i$ taken pulse by pulse by pulse is kept quite stable as shown in right side of Figure4.15. Upper mean value(0.947) and lower mean value(0.9489) are almost consistent.

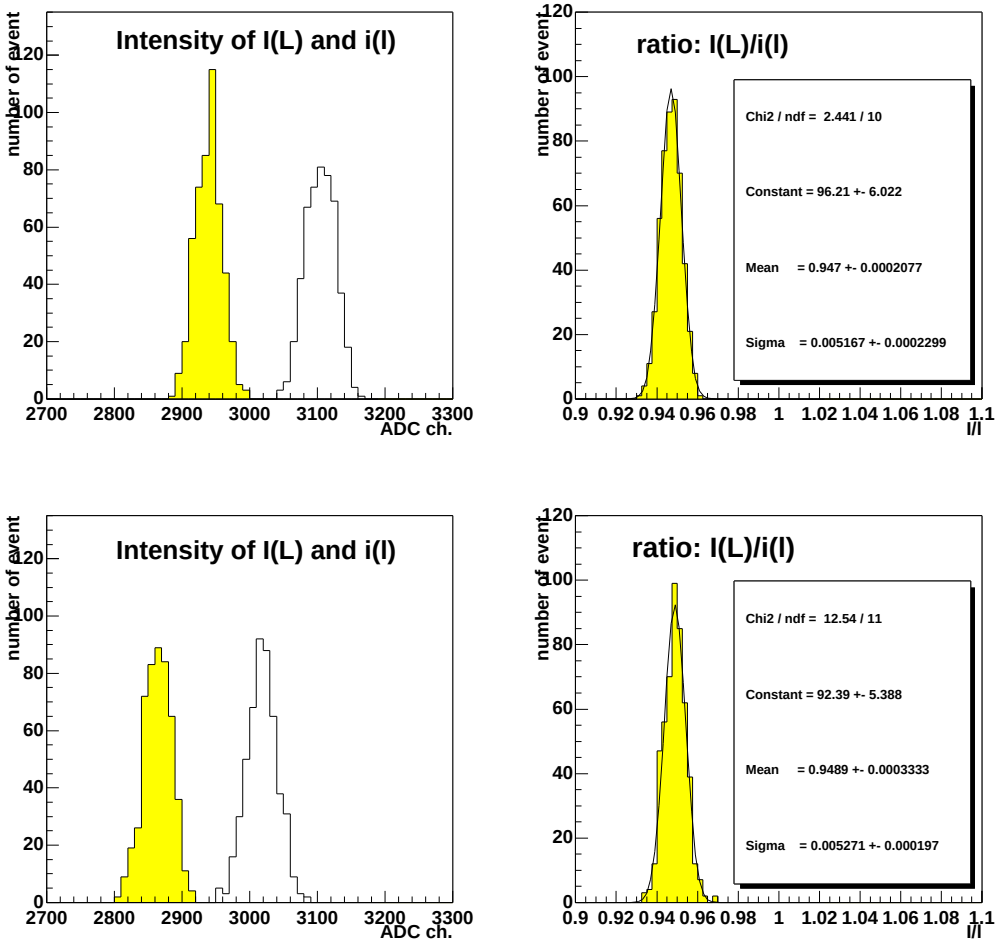

Figure 4.15: Left-side two figure denotes the intensity of two beams. The hatched histogram is for $I(L)$, and another for $i(l)$. Taking a ratio of $I(L)$ to $i(l)$ pulse to pulse, instability of the laser output is canceled.

Beam splitter and mirror are used due to divide laser beam, these optical apparatuses are origin of the systematic error. Therefore, we measure $I(L)/i(l)$ ratio(R) using "air" in place of the scintillator. This is the measurement of the influences of optical apparatuses because transparency of air is almost infinite long. In order to cancel these systematic error, transparency(T) and attenuation length(Λ) of the scintillator

are defined as;

$$T = R_{scintillator}/R_{air} \quad (R = I(L)/i(l)) \tag{4.1}$$

$$\Lambda = \left[\frac{L-l}{-\ln T}\right] = \left[\frac{1.75}{-\ln T}\right] \text{[m]} \tag{4.2}$$

$$\delta\Lambda = \frac{\partial\Lambda}{\partial T} = \Lambda^2 \frac{\delta T}{T} \tag{4.3}$$

here, δT and $\delta\Lambda$ denote the measurement error of the transparency and the attenuation length, respectively.

However, it is impossible to remove all systematic errors. Systematic errors which cannot take off are measured by reproducibility. Various reproducibilities were checked, and these results are shown in Table 4.1. Total systematic error of transparency, δT is estimated less than 1.2% from summing up each reproducibility in this table. This corresponds to the $\delta\Lambda \leq$1.4m at Λ=10m

checked reproducibilities	δT
T(L - l=0m)	$\leq$0.9%
influence of reflection in tube	$\leq$0.24%
position & direction dependence on integrating sphere	$\leq$0.73%
Total	$\leq$1.2%

Table 4.1: Various reproducibilities were checked. Total systematic error of transparency, δT, is estimated less than 1.2%.

For N_2/Dye-laser, we use is LN203C Nitrogen Dye Laser(Laser Photonics). Specification of the product is described in Table4.2. The LN203C consists of a combination of a nitrogen laser and an optical dye laser module(Figure-reflaser). The nitrogen laser(wavelength = 337.1nm) is operable, and its beam accessible, with and without the dye module installed. Table 4.3 shows dyes and their peak wavelength.

Inside of the integrating sphere is painted by an optical diffuser making white reflective wall. Light from the input port is diffusely reflected inside the sphere, so the output port is uniformly illuminated independent of the initial beam alignment(Figure4.18). The scrambling effect of the sphere ensures that the output is insensitive to the spatial, angular and polarization condition of the input. The highly uniformed coating makes an almost perfect diffuse reflector. Wavelength dependence of reflection is small, and wavelength dependence of throughput is small, too(Figure4.17). Sphere throughput is defined as the ratio of the total output power to the total input power. It depends on the reflection and the ratio of the port area to sphere wall area. The integrating sphere we used is '70461 Fiber Optic Integrating Sphere'of ORIEL(Figure4.19).

item	LN203C	Dye laser
Spectral Output (nm)	337.1	357∼710
Spectral Bandwidth (nm)	0.1	1∼3
Pulse-width (ps FWHM)	600	300∼500
Energy/Pulse (μJ)	100	Dye dependent
Conversion Efficiency (%)	N/A	15 at 500nm
Energy/Stability (%)at 10Hz	3	3
Peak Power (kW)	167	
Repetition Rate (maximum) (Hz)	50	50
Maximum Average Power (mW)	5	Dye dependent
Beam Dimensions (hor.x ver.) (mm)	5.5 × 3.1	2.5mm at exit
Flow Rate (L/min) at 10Hz	1.51	
Trigger In/Out	TTL	
Command Jitter (nm)	±2	
Input voltage	110V	
Dimensions (cm)	71.3 × 21.3 × 13.3	
Weight (kg)	9	

Table 4.2: Specifications of LN203C N_2/Dye laser

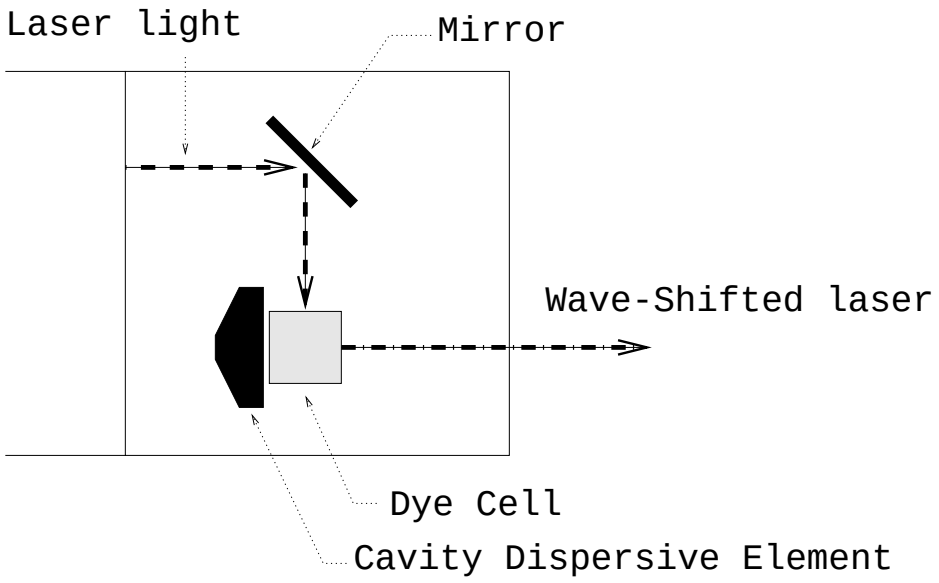

Figure 4.16: Dye-Module

Dye	Peak (nm)	Range (nm)
BPBD	365	357-395
PBD	366	360-386
BBQ	386	373-399
PBBO	400	391-411
DPS	406	396-416
BIS-MS13	421	411-430
S-420	425	408-453
C-440	437	427-457
C-450	446	428-465
C-460	457	440-478
C-480	470	453-495
C-481	481	460-518
C-500	500	473-547

Table 4.3: The structure and wavelength of dye

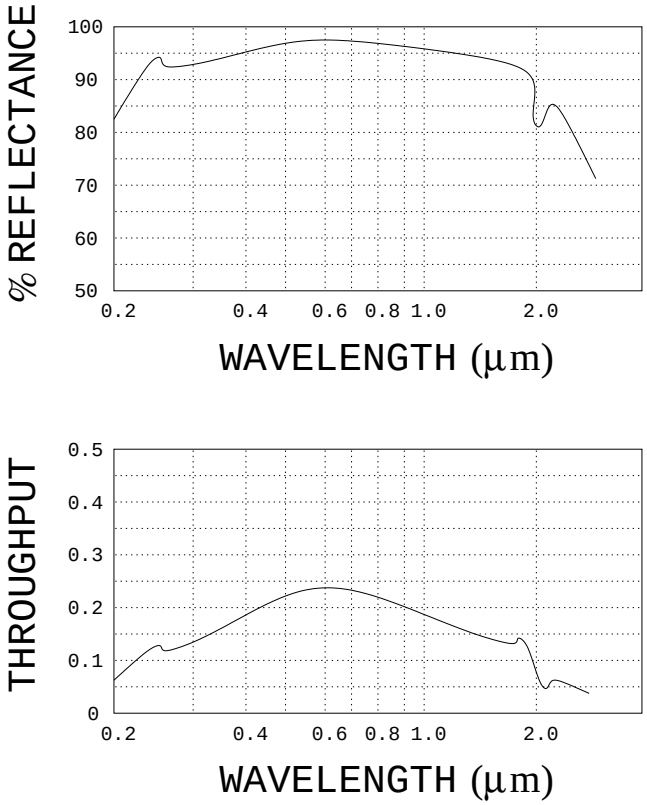

Figure 4.17: Internal reflectance and throughput of the integrating sphere

The PMT is the 2inch head-on type photo-multiplier tube(H1161-50) which is a product of HAMAMATU PHOTONICS K.K.. Table4.4 shows specification of the PMT. The coupling of the optical fiber and the PMT is shown in Figure4.20. Output light from optical fiber spreads by $0.2(= \tan\theta)$. Therefore, the FC connector is separated from the photo-cathode face by 10cm, so that the light expand to ϕ40mm which matches with the diameter of photo-cathode($\phi = 46$mm).

Photo-cathode	Bialkali
Material of Photo-current	UV Glass
Max. Overall Voltage(V)	-2700
Max. Bleeder Current(mA)	1.23
Max. Average Anode Current(μA)	46 at 2000V
Dark Current	$\leq$ 100nA
Rise Time	2.7ns
Transit Time	40ns
Spectral Response Range	300 $\sim$ 650nm

Table 4.4: Specifications of H1161-50

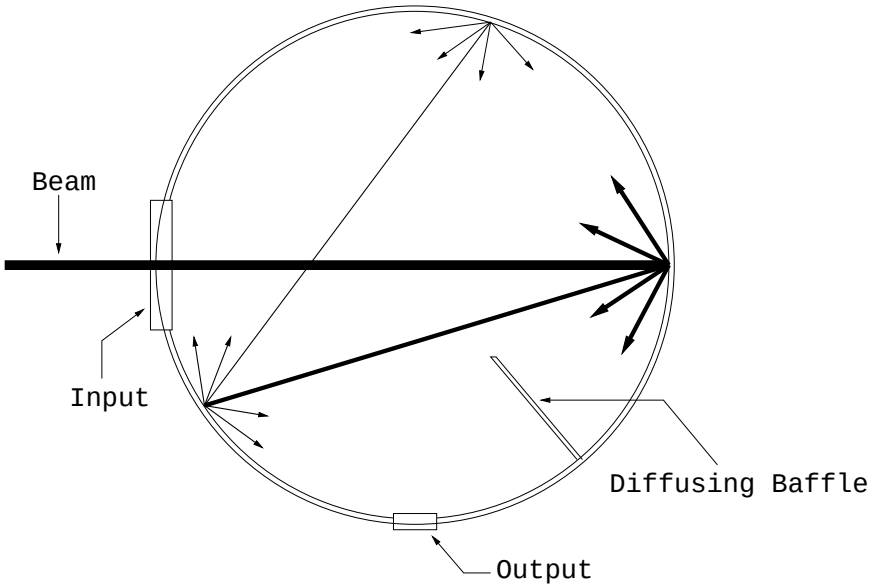

Figure 4.18: The incoming beam is diffusely reflected inside an integrating sphere. The output port cannot "see" the region of first impact.

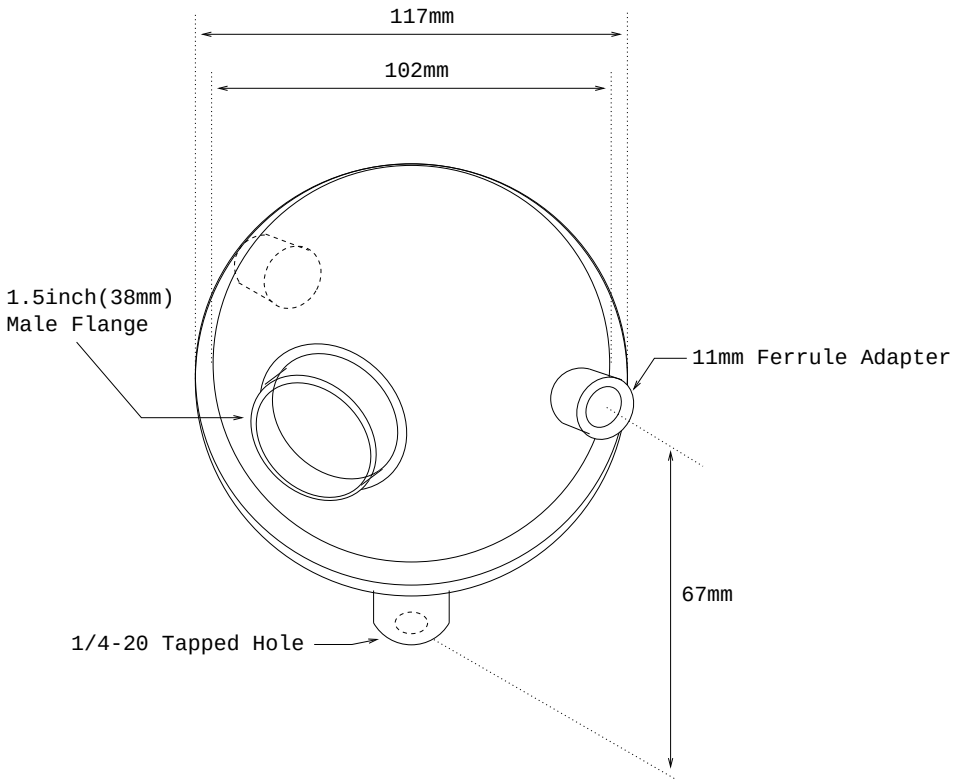

Figure 4.19: 70461 Fiber Optic Integrating Sphere

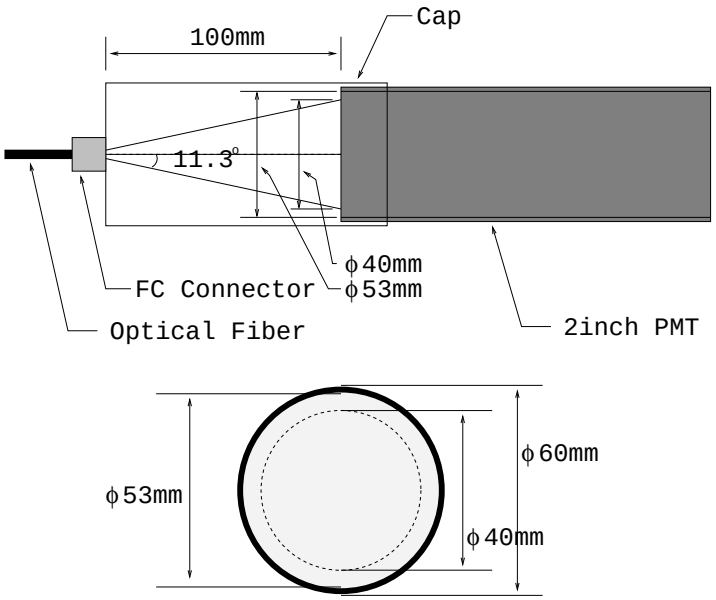

Figure 4.20: Connection optical fiber with PMT.

4.3 Result of measurement

Measured samples are;

(A) Paraffin-oil(80%) + P.C.(20%) + PPO(2g/l)

and

(B) Paraffin-oil(80%) + P.C.(20%) + PPO(2g/l) + BisMSB(0.1g/l)

Obtained transparencies and attenuation lengths of scintillators are shown in Table4.5. And Figure4.21 shows attenuation length as a function of wavelength. Different marks

wavelength	$T_{(A)}$	$T_{(B)}$	$\Lambda_{(A)}$	$\Lambda_{(B)}$
@386nm	79.1%	-	5.3m	-
@406nm	84.9%	-	7.6m	-
@421nm	88.6%	56.1%	10.3m	2.2m
@437nm	-	88.5%	-	10.2m
@446nm	91.0%	89.5%	13.3m	11.3m
@470nm	92.1%	92.1%	15.2m	15.2m

Table 4.5: Table of transparencies(T) and attenuation lengths(Λ) calculated from T for scintillators (A) and (B).

denote diferent measurements, and all measurements are consistent within the error. The attenuation length at long wavelength is better than that at short wavelength.

Dash lines denote expected attenuation lengths using results of absorption meter(Figure 4.11). Error of expected results from absorption meter is very large because of the size(9cm of light path), and estimated about $\delta\Lambda$=5m at 10m of attenuation length. However, these two results agree with our measurements at 386nm of wavelength for (A) and at 421nm for (B).

At the short wavelength range(360∼380nm), attenuation length cannot be measured since the intensity of Dye-laser is very weak at this range. We use results of absorption meter at this range for various calculation(Section 4.4).

For (A), the peak wavelength of the PPO emission is about 375nm(figure4.3). Scintillator (B) is opaque below 410nm of the wavelength because of absorption of the BisMSB, attenuation length is 15.5m at 437nm of wavelength. And peak wavelength of the BisMSB emission is about 420nm.

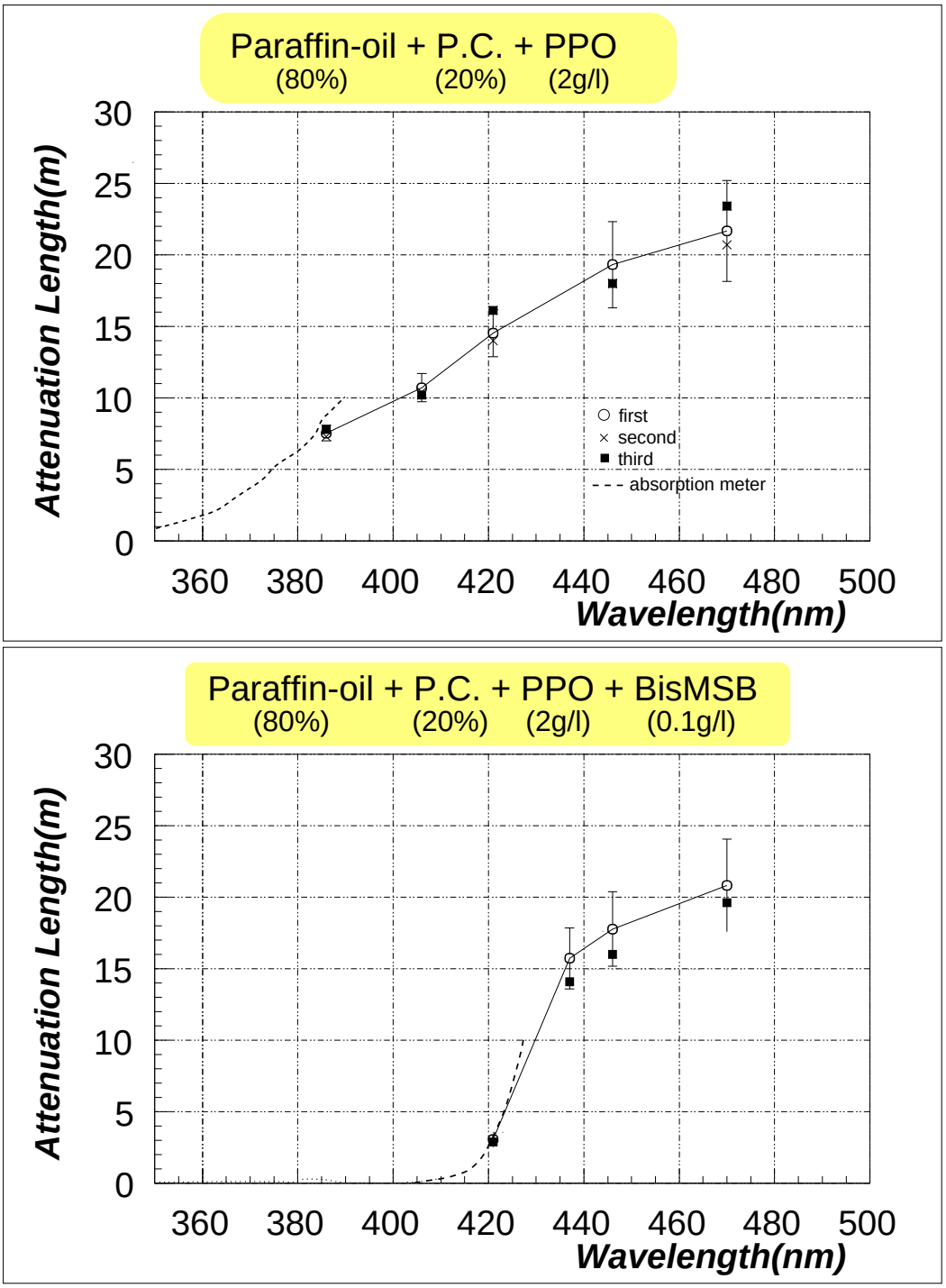

Figure 4.21: Attenuation length spectrum of the scintillator. ◯, × and ■ are measurement results, all measurement results are consistent within estimated error. Dash lines denote the expected attenuation lengths using the absorption meter. Error of expected results from absorption meter is very large because of the size(9cm of light path), and estimated about $\delta\Lambda$=5m 10m of attenuation length. For the scintillator which is added BisMSB, this is opaque below 410nm of the wavelength because of absorption of the BisMSB.

4.4 Estimation of the Light Yield

The light yield(p.e./MeV) of the KamLAND detector can be calculated by results of light-output, attenuation length(Figure4.21), emission spectrum(Figure4.3), PMT quantum efficiency(Figure1.13), surface coverage of PMTs(36%), balloon transparency (94%). Considering these effects, detection spectra after transferring 6.5m of two scintillator are obtained as shown in Figure 4.22. Scintillation lights below peak emission wavelength is no more effective.

Vertex dependences of light yield are shown in Figureref4.23, the horizontal axis is the distance from the center of the detector to the emission point. The error of detected photon is at least 10% which only contains uncertainty from the attenuation-length and light-output measurements. From this figure, the light yield is larger as the emission point goes close to the PMT surface. The light yield of the KamLAND detector is about $\sim$ 158 p.e./MeV for central events.

For uniformly distributing events inside the fiducial volume($R \leq$5.5m is expected), average light yields are shown in Table 4.6.

scintillator	average light yield
(A) Paraffin-oil(80%)+P.C.(20%)+PPO(2g/l)	$\sim$ 190p.e./MeV
(B) Paraffin-oil(80%)+P.C.(20%)+PPO(2g/l)+BisMSB(0.1g/l)	$\sim$ 180p.e./MeV

Table 4.6: Average light yield of two scintillator. It is assumed that events distribute uniformly inside the fiducial volume which is expected 5.5m.

In these estimations, effects from reemission is not taken into account. It will increase total number of photons to be detected, thus they are off timing(delayed) hits.

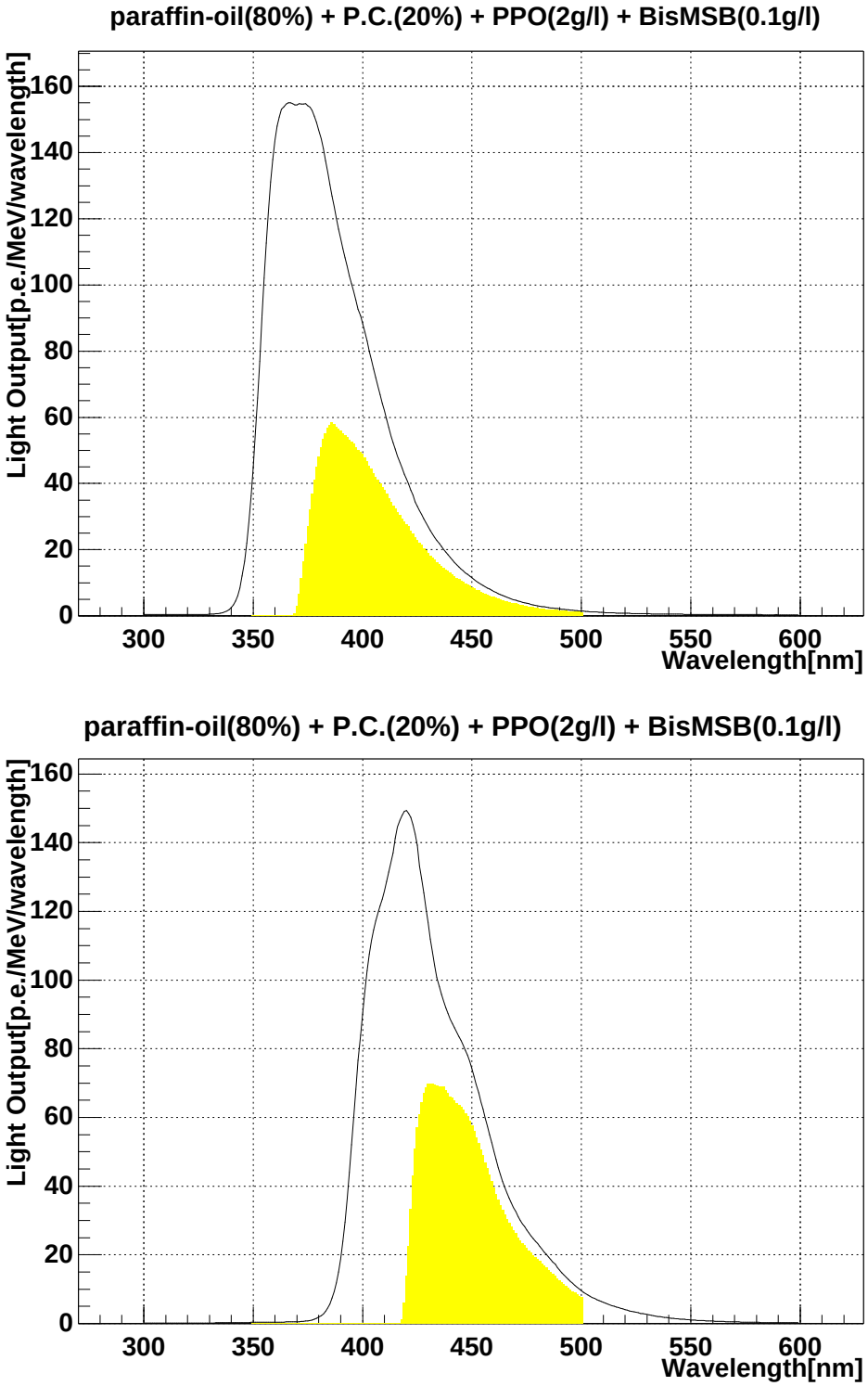

Figure 4.22: Wavelength dependences of emission lights and detected lights. Filled spectrum denote detected light spectra, and non-filled spectra are the emission light spectrum. Detected light is the light which is detected by PMTs at KamLAND. These spectra are calculated using various parameter, light-output, attenuation length(Figure4.21), emission spectrum(Figure4.3), PMT quantum efficiency(Figure1.13), surface coverage of PMTs(36%), balloon transparency (94%).

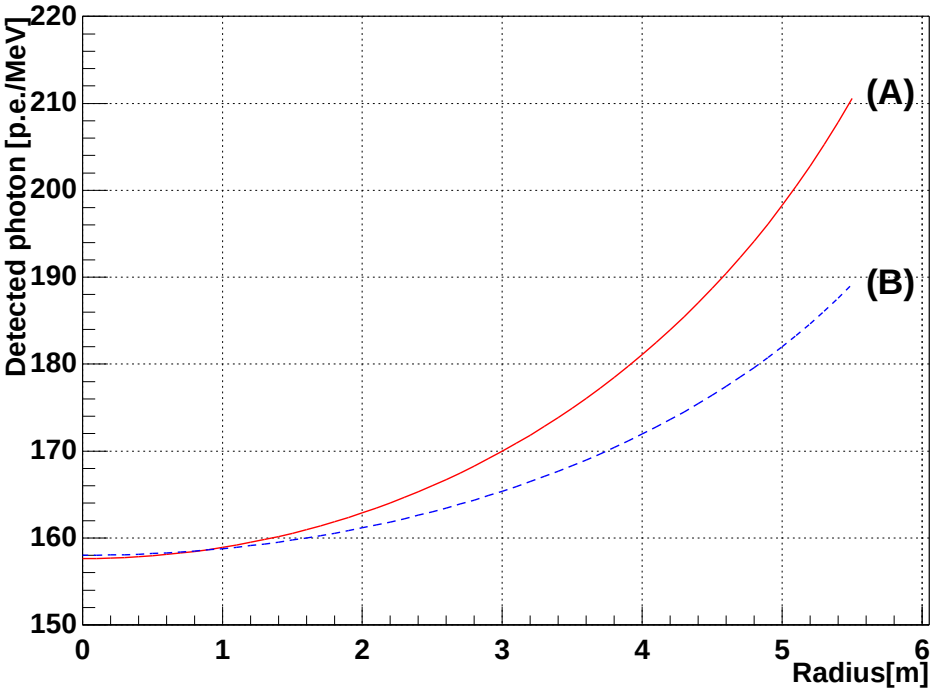

Figure 4.23: Position dependence of the light yield.

4.5 Summary

KamLAND will detect low energy(above a few hundred keV) neutrinos and anti-neutrinos. Here, high energy resolution give us accurate studies, for example deciding oscillation parameters precisely.

The energy resolution depends on the light yield, the number of detected photo-electron[p.e./MeV]. In other words, developing a high light yieldscintillator is very important.

From the light output and misidentification measurements, components of the KamLAND scintillator has been chosen as,

(A) Paraffin Oil(80%) + P.C.(20%) + PPO(1∼2g/l)

or

(B) Paraffin Oil(80%) + P.C.(20%) + PPO(1∼2g/l) + BisMSB(0.1g/l)

We have measured light attenuation lengths above scintillators(Figure4.21), and have estimate light yields of the KamLAND detector(Figure4.23). The mean light yields of the KamLAND detector are estimated to be ∼190 p.e./MeV for (A) and ∼180 p.e./MeV for (B), here the error of these estimations are more than 10%.

From various measurements, attenuation-length, light-output and misidentification probability, we could not find a merit to use BisMSB as the wavelength shifter. On the other hand, adding BisMSB cost much more money and this is insoluble as compared with PPO. At the present stage, we think that adding BisMSB has some demerits, and decide **not to use the BisMSB for the component of KamLAND scintillator**.

In summary, we decide components and rough concentrations of KamLAND scintillator. P.C. is need at least 20% and PPO is at least 1g/l result from measurements of a misidentification probability., From the point of transparency, paraffin oil has been chosen for a base liquid, and necessary concentration of PPO is 2g/l or less. BisMSB is not necessary because we could not find a merit using it from various measurement results.

Paraffin Oil(80%) + P.C.(20%) + PPO(1∼2g/l)	
attenuation length	7.6m @ 406nm
estimated light yield	∼158p.e/MeV(central events)
	∼190p.e/MeV(on average $R \leq$5.5m)

Chapter 5

Direct Light Yield Study of the KamLAND Liquid Scintillator

Direct measurement of the light yield is the best way to estimate the actual photoelectron number in a large liquid scintillator system. We have made 6.8m long liquid scintillator system. The light yield was measured by detecting the scintillation light from the cosmic-ray muons. The distance from the emission position to the detection position is 640cm(KamLAND scintillator vessel radius is 650cm). From this measurement, we determined the components of the liquid scintillator for KamLAND to be,

$$\text{N12(80\%)} + \text{P.C.(20\%)} + \text{PPO(1.5g/l)},$$

where, N12 is normal Dodecane, P.C. is pseudocumene(1,2,4Trimethyl Benzene).

Using the measurement results, the light yield of the KamLAND detector is $\sim$180p.e./MeV(Threshold = 1/4p.e.) for the central events, if average transparency of the vessel balloon is 94%, and the number of 17"PMT and 20"PMT are 1295 and 590, respectively. This corresponds to statistical energy measurement fluctuation of

$$\delta\text{E/E} = 7\%/\sqrt{\text{E(MeV)}}\ .$$

5.1 Motivation

KamLAND will detect the low energy neutrinos and anti-neutrinos. For example, the energy range of the reactor anti-neutrinos is several MeV and that of the solar neutrinos, especially ^{7}Be neutrino, is 862keV. To detect such a low energy neutrino, the energy resolution of KamLAND have to be good in the energy region from a few hundred keV to several MeV.

The energy resolution is depends on the number of the detected photon(light yield). So, the light yield study of the liquid scintillator is very important. Moreover, optimizing component from the light yield study is also very important.

The light yield depends on the light output and transparency of the liquid scintillator, PMT quantum efficiency, number of PMTs, and so on. We can estimate the light yield from measurement results of the light-output study. However these measurements well performed in the apparatus which is smaller than KamLAND, and wavelength dependence cannot be taken into account well. Therefore, the direct measurement is the best way to study the actual light yield.

5.2 Liquid Scintillator

The Base liquid of the liquid scintillator for KamLAND is paraffin oil. The transparency of paraffin oil is better than pseudocumene. The KamLAND scintillator consists of solvents and a solute, that is, paraffin-oil, Pseudocumene and PPO.

$$\text{Paraffin-oil} + \text{Pseudocumene(P.C.)} + \text{PPO}$$

P.C. is one of the most popular solvents to be used in large volume liquid scintillators, and PPO is one of the most popular solute. P.C. is indispensable component for the Pulse Shape Discrimination(PSD)[31]. There are two candidates for paraffin-oil, Isoparaffin(P250[1]) and Normal-Paraffin(N12[2]). The transparency of N12 is little better than that of P250, but that difference is very little. So, we compared P250 and N12 by the long liquid scintillator system.

From other studies(light-output, PSD)[31], the ratio of the paraffin-oil to the solvent(P.C.) was decided to be 8 : 2. From other studies(light-output[31], light attenuation length[27], emission spectrum[26]), and a calculation using these results suggest that the best concentration of PPO is 1$\sim$2g/l.

[1] praol 250, Showa Shell, Japan
[2] Normal Paraffin N12D, Cosmo Petrolium Company, Japan

5.3 Apparatus

5.3.1 Setup

The apparatus is shown in Figure5.2. The liquid scintillator is filled in the anodized Aluminum tube whose the internal diameter is 14cm and the length is 683cm, both ends of the scintillator pipe are sealed by UV transparent acrylic plates of 35mm thick and viewed by 5"PMTs(HMAMATU R1250). The scintillation light is derived from the energy deposit of the cosmic ray muons. Three plastic scintillators(5cm×10cm,5cm×10cm and 10cm×16cm) sandwich the tube in order to tag the cosmic rays. To suppress the light reflection, there are thin Alminium(anodized) rings at intervals of 40cm in the tube. The internal diameter of the ring is 11cm. From simple simulation, the amount of the reflection light is estimated to be less than 0.01%. The triple coincidence of plastic scintillation counters creates trigger signal, TDC-start and ADC-gate signals. ADC measure the total charge of 5"PMT and TDC measure the time between the time of the photon hits 5"PMT and the time the trigger is created(Figure5.3).

5"PMT which is near trigger counter monitor the light-output, and we can know the deposit energy of muon. This PMT is called **energy monitor**. A radioactive source is used at energy calibration. On the other hand, there is another 5"PMT, 640cm away from trigger counter. The distance 640cm is near the KamLAND balloon radius of 650cm. The number of photoelectrons which is detected by the 2nd PMT is 0.1∼0.2p.e./Trigger, therefore the direct light yield is calculated by photon counting method. This PMT is called **photon counter**. When the photon counter does not detect photon(0 photon), TDC will be overflow. Because the probability that the photon counter detects photon is ∼1/10, the average number of p.e. can be calculated from the Poisson distribution.

Moreover, the timing property of scintillation light is can directly be measured by the time distribution of the photon counter.

5.3.2 PMT

5"PMTs for photon counting and monitor are HAMAMATU R1250. The quantum efficiency(Q.E.) of the cathode is 22% which is the same value of 17"PMT Q.E.. 1 photoelectron charge distribution and transit time spread are shown in Figure5.4. The transit time spread(TTS) is 3.1nsec(FWHM).

PMTs for trigger counter are HAMAMATU R580(1-1/2").

Figure 5.1: The picture of the setup apparatus for the light yield measurement.

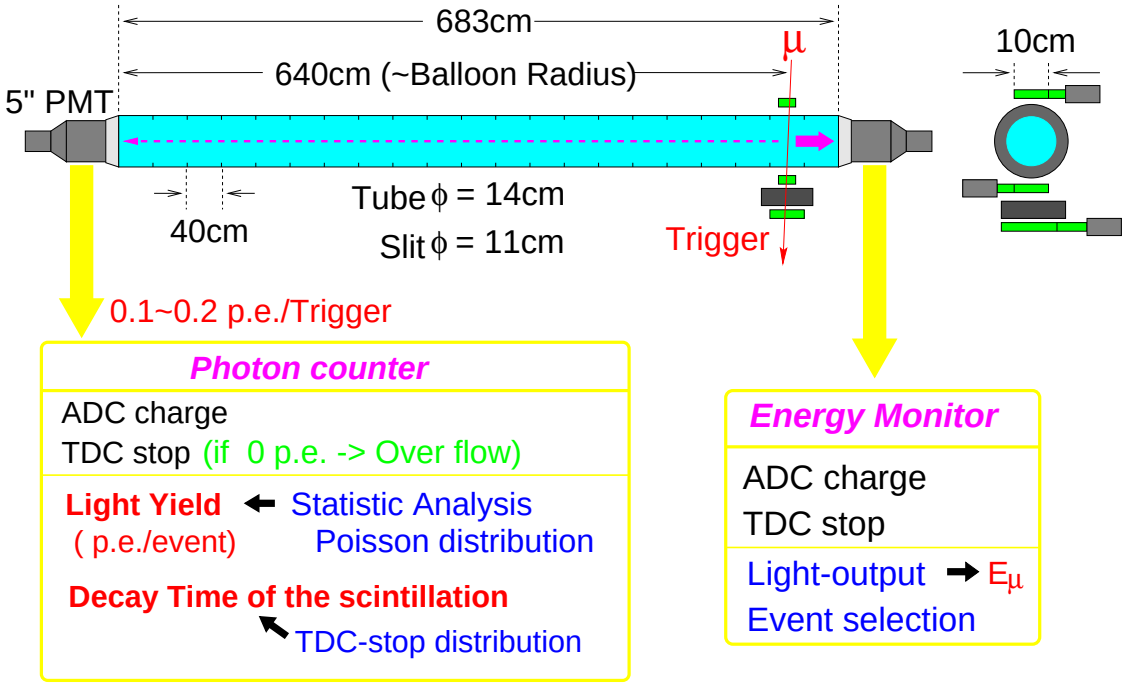

Figure 5.2: The liquid scintillator is filled in the long(683cm) tube, and the scintillation light is detected by two 5"PMT put on both ends of the tube. One PMT is used for the photon counting, and another is the scintillation light monitor of each event. The former is named **photon counter**, and the latter is **energy monitor**. The cosmic ray muon is identified using the triple coincidence of the three scintillation counters(trigger counter) whose scintillator are the plastic scintillator, and this coincidence signal is the event trigger. The distance from the trigger counter to photon counter is 640cm which is almost same as the radius of the scintillator vessel(balloon) at KamLAND. The detected photon par event at the photon counter is 1∼2 photon because the solid angle of the photon counter to the emission point is very small and the light is attenuated while propagate in the scintillator.

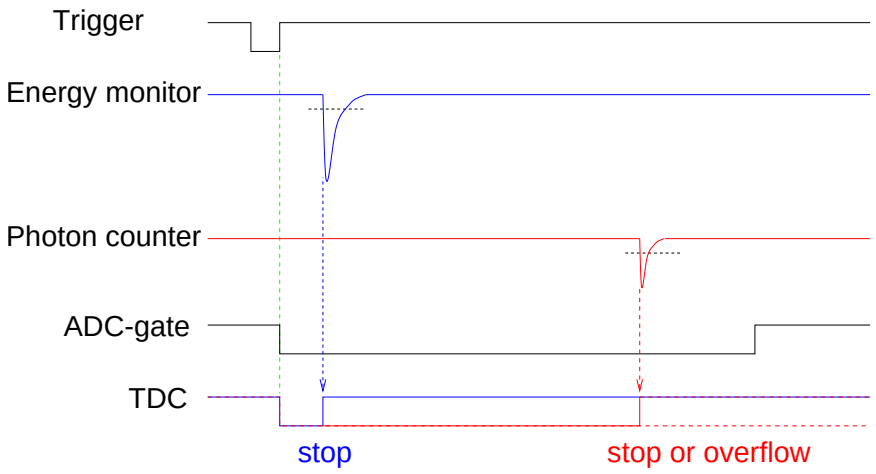

Figure 5.3: Total charges both of 5"PMT are measured by ADC, and the timing information is by TDC. ADC gate and TDC start signals are created from the trigger signal. For photon counter, the number of the detected photon is about 1photon, so that stop signal is rarely created.

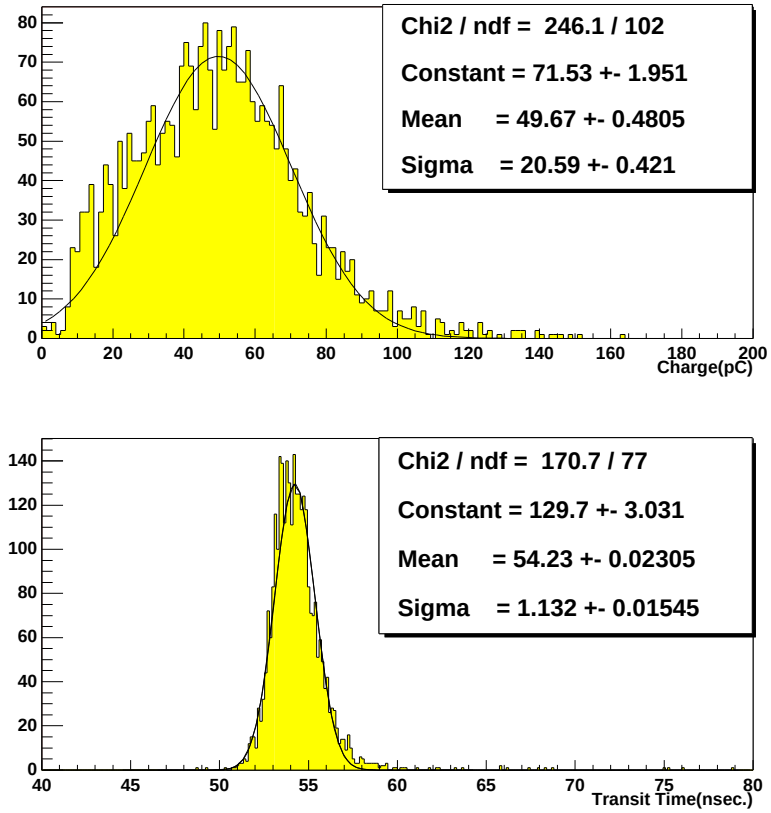

Figure 5.4: 1photon charge and transit time distribution of 5"PMT.

5.4 Analysis method

The measurement results, charge and time distribution of photon counter and energy monitor, are shown in Figure5.5. The peak($\sim$160pC) in the charge distribution of photon counter is 1p.e. peak. The shape of the photon counter time distribution reflects the shape of the emission, and the decay time(τ) is calculated from fitting. The dark shadow events in photon counter events, the overflow events about the charge and the fast events about time, are shower events. On the other hand, for the energy monitor, the charge reflects the deposit energy of muon and overflow events in the time distribution stands for accidental trigger(accidental coincidence of trigger counters).

After excluding background events(dark shadow), the number of the energy monitor event is N, and the number of the photon counter event is (N-n)(the number of overflow event is n). The analysis using Poisson distribution,

$$P(x) = \frac{\lambda^x}{x!}\mathrm{e}^{-\lambda} \qquad (x = 0, 1, 2\cdots) \tag{5.1}$$

produce the light yield. Here, λ is the mean photon number(p.e./event) and x is the number of photon per event. The number of the $x = 0$ events is equal to the number of TDC-overflow events, so that

$$P(0) = \frac{\lambda^0}{0!}\mathrm{e}^{-\lambda} \tag{5.2}$$

$$= \mathrm{e}^{-\lambda} \tag{5.3}$$

$$\therefore \quad \lambda[\text{p.e./event}] = -\ln\left[P(0)\right] \tag{5.4}$$

$$= \ln\left[\frac{\#\text{ of events}}{\#\text{ of TDCoverflow events}}\right] \tag{5.5}$$

$$= \ln\left(\frac{\mathrm{N}}{\mathrm{n}}\right) \tag{5.6}$$

Using the above equation, the light yield per event[p.e./event] is measured.

The background which cannot be removed this analysis is that the scintillation light by the environmental radiation hit the photon counter(TDC-stop) before require light hit. This background is measured using random trigger. As a result, the background is less than 10^{-3}p.e./event. This can be ignored statistically.

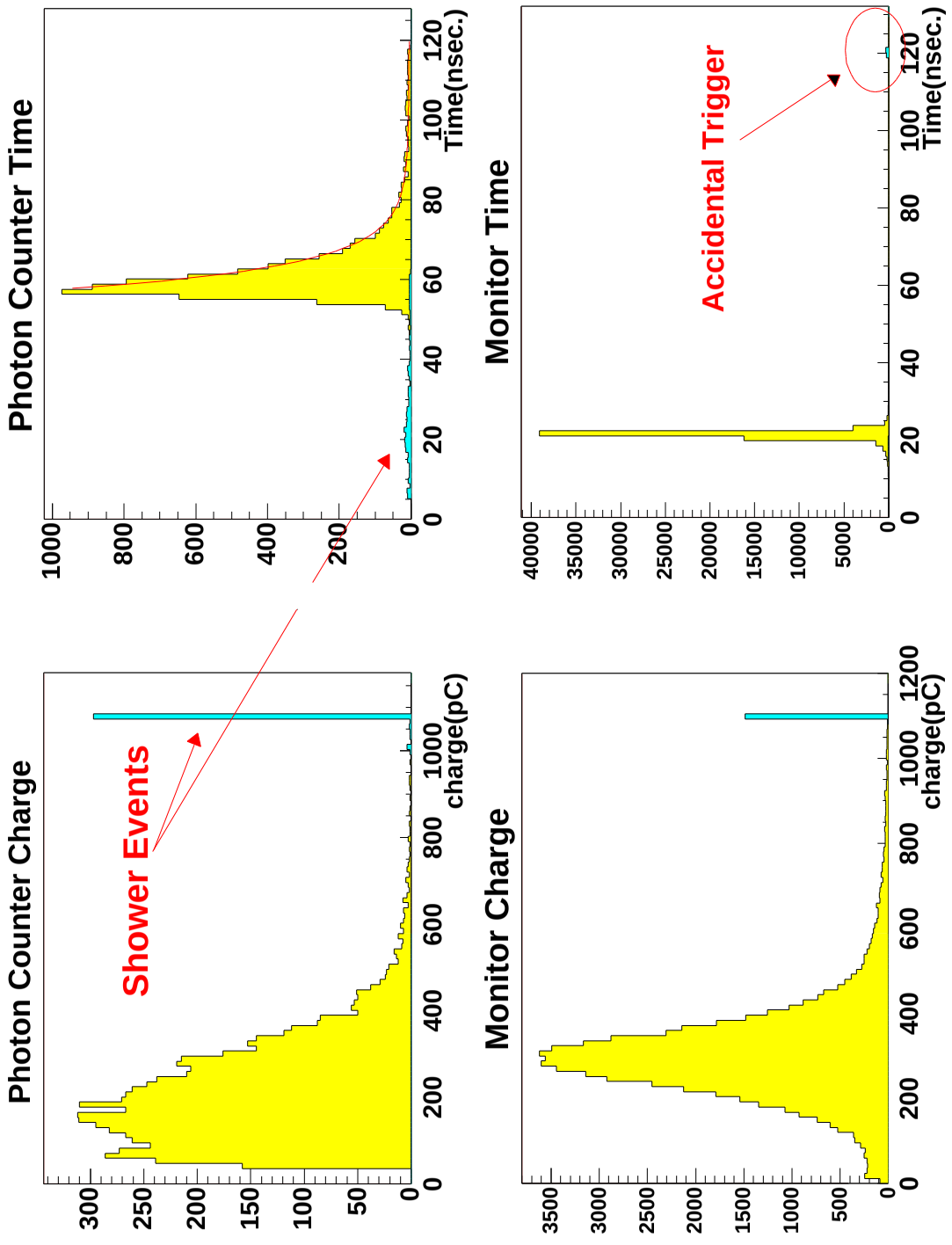

Figure 5.5: Charge and time distribution of photon counter and energy monitor. The light blue express backgrounds from shower events or accidental trigger. The threshold of photon counter is 1/4p.e.

5.5 Measurement results

5.5.1 Paraffin-Oil Dependence of Light Yield

At first, we measured the light yield of two scintillators which were diluted with different paraffin-oils, one is diluted with normal-paraffin(N12) and the other is diluted with iso-paraffin(P250). Two scintillator are consists of

$$\text{Paraffin-oil}(80\%) + \text{P.C.}(20\%) + \text{PPO}(2\text{g/l}).$$

The measurement results are shown in Tabel5.1. The light yield of the N12-base scintillator is better than P250-base one. From this result, it is find that N12 is better than P250 in terms of the light yield.

Paraffin-Oil	N/n	Light Yield[p.e./event]
N12	96926/82987	0.155±0.001
P250	63052/55830	0.122±0.001

Table 5.1: Measurement results of scintillators which are diluted with different paraffin-oil.

5.5.2 PPO concentration dependence of Light Yield

The PPO concentration dependence of light yield is shown in Table5.2, Figure5.6. From these measurement results, the best PPO concentration is 1.50g/l.

PPO[g/l]	N/n	Light Yield[p.e./event]
2.00	96926/82987	0.155±0.001
1.77	96727/81988	0.165±0.001
1.50	88786/75110	0.167±0.01
1.25	95910/81611	0.161±0.01
1.00	29724/25712	0.145±0.02

Table 5.2: PPO concentration dependence of the light yield.

5.5.3 PPO concentration dependence of Decay Time

The PPO concentration dependence of decay times are shown in Table5.3, Figure5.7. The fitting result of the photon counter time distribution provides decay times. In general, the scintillation light may be given by a two-component exponential, fast and

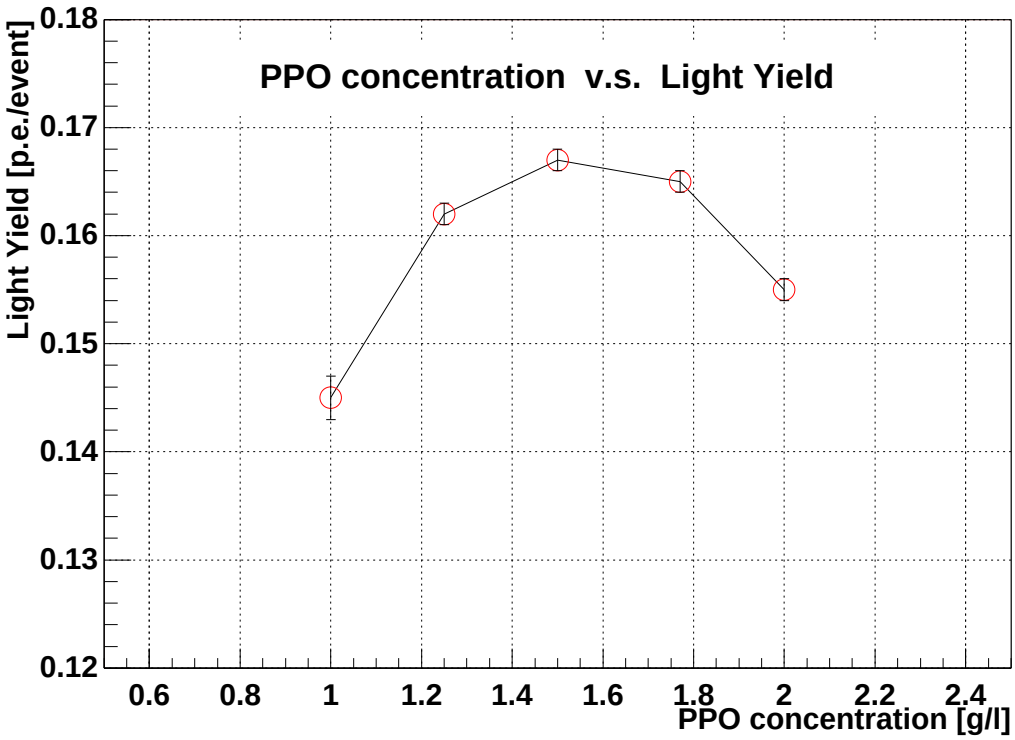

Figure 5.6: PPO concentration dependence of the light yield. When PPO concentration is 1.5g/l the light yield is maximum.

slow, although the fast component dominates(C.3.1). In Table5.3, "Fast component" and "Slow component" are decay times of the fast component and slow component, respectively.

If the PPO concentration is lower, the decay time for the fast component becomes longer. On the other hand, the decay time for the slow component almost doesn't change if the PPO concentration is longer.

PPO[g/l]	Fast Component[nsec]	Slow Component[nsec]	χ^2/d.o.f.
2.00	5.406 ± 0.09584	37.44 ± 6.667	90.77/46
1.77	5.572 ± 0.1009	45.58 ± 11.07	95.39/45
1.50	6.115 ± 0.1174	52.55 ± 16.68	110.1/45
1.25	6.499 ± 0.1111	48.53 ± 17.6	129.1/45
1.00	6.835 ± 0.06039	31.75 ± 3.468	98.2/45

Table 5.3: PPO concentration dependence of decay times.

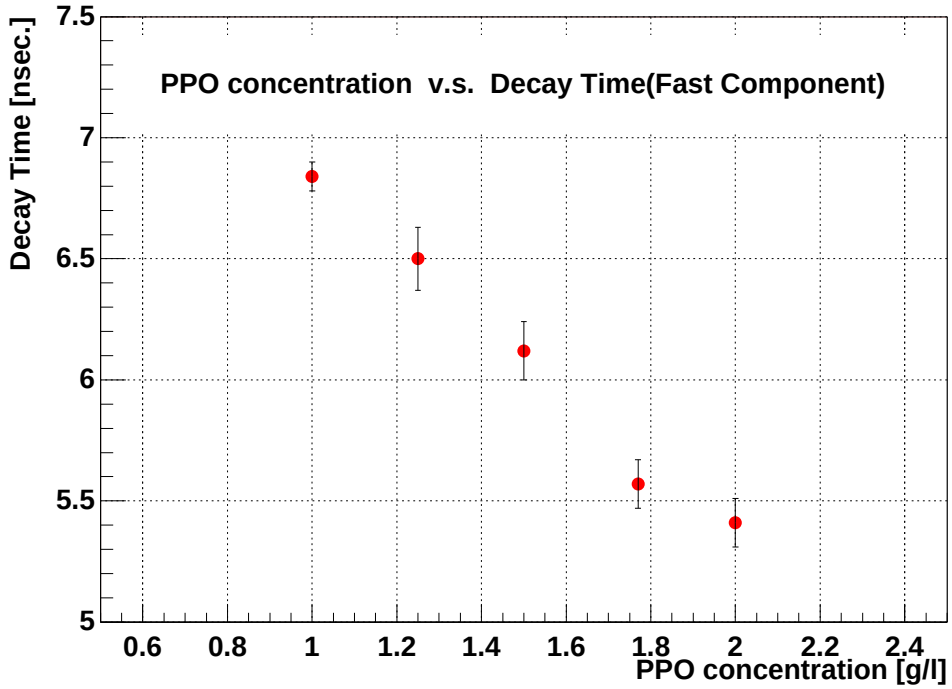

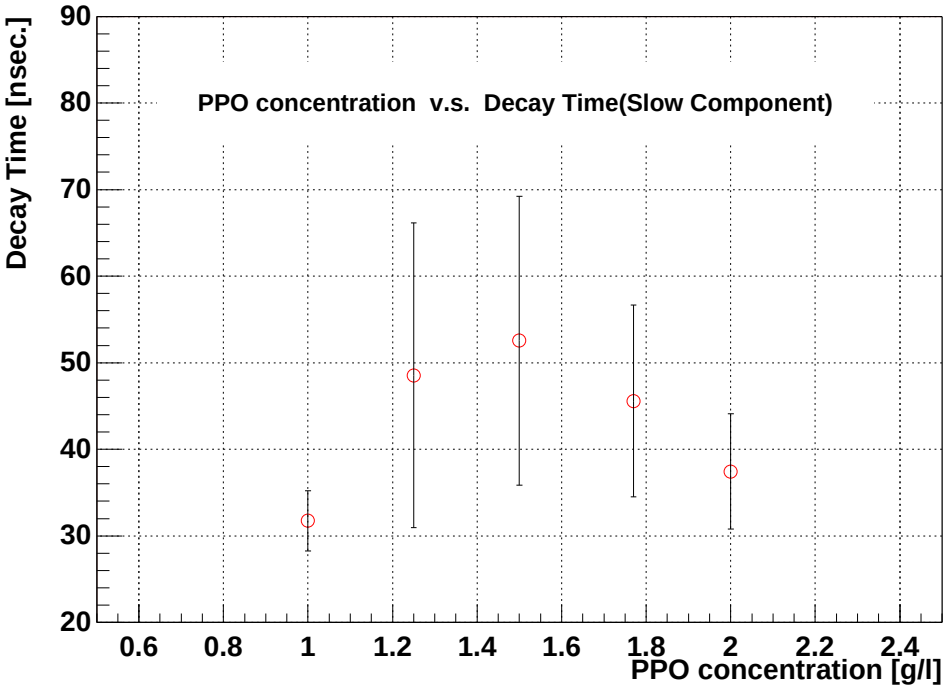

Figure 5.7: PPO concentration dependence of decay time. For fast component, the decay time is longer as PPO concentration become small. On the other hand, PPO concentration dependence is hardly ever seen for the slow component.

5.6 Energy(dE/dX) Calibration

Because we need to know the absolute light yield on a certain energy, the energy calibration for the monitor PMT is very important. The light-output of the liquid scintillator is proportional to the energy, and the ADC charge of the energy monitor is proportional to the light output. If we know the ADC charge which corresponds to one energy, we can know the energy μ deposits at the apparatus event by event.

We used ^{137}Cs(γ-ray 662keV) and measured the the ADC charge of energy monitor which corresponds to the compton scattered electron energy. The energy of the electron which is scattered to the fixed angle is constant.[3] If the direction of the scattered γ-ray to the input γ-ray is 180°(Back Scatter), the scattered electron kinematic energy is 478keV(∵ function(D.12)).

The Setup for Energy calibration is shown in Figure5.8. The event trigger is created by the coincidence of the scattered electron(energy monitor) and back scattered γ(NaI scintillation counter). Figure5.9 show the ADC charge histogram of the energy monitor when the distance between energy monitor PMT and ^{137}Cs is short(∼13cm). The charge at the peak corresponds to the scattered electron energy, 478keV. The left hand side of the peak is the backgrounds which comes from the accidental coincidence.

Figure5.10 shows the results when the distance between energy monitor PMT and ^{137}Cs or muon trigger is 25cm. The peak charge which corresponds to 478keV is 17.8±0.4pC, and the peak charge by cosmic ray muon is 867.5±6.8pC. Assume the zenith angle distribution of the cosmic ray muon is $\cos^2\theta$, muon path which corresponds to the peak is 14cm. From these result, the energy which corresponds to the peak charge is 23.2±0.6MeV(muon path = 14cm). For the photon counter, the effective diameter of the Aluminum tube is 11cm because the internal diameter of the ring is 11cm. Therefor, the energy which corresponds to the peak charge is 18.2±0.5MeV for the photon counter. If dE_μ/dX ∼2MeV·cm^2·g^{-1}, the muon deposit energy is expected to be ∼18MeV(muon path = 11cm). This is the consistent with the measurement result.

[3] See AppendixD

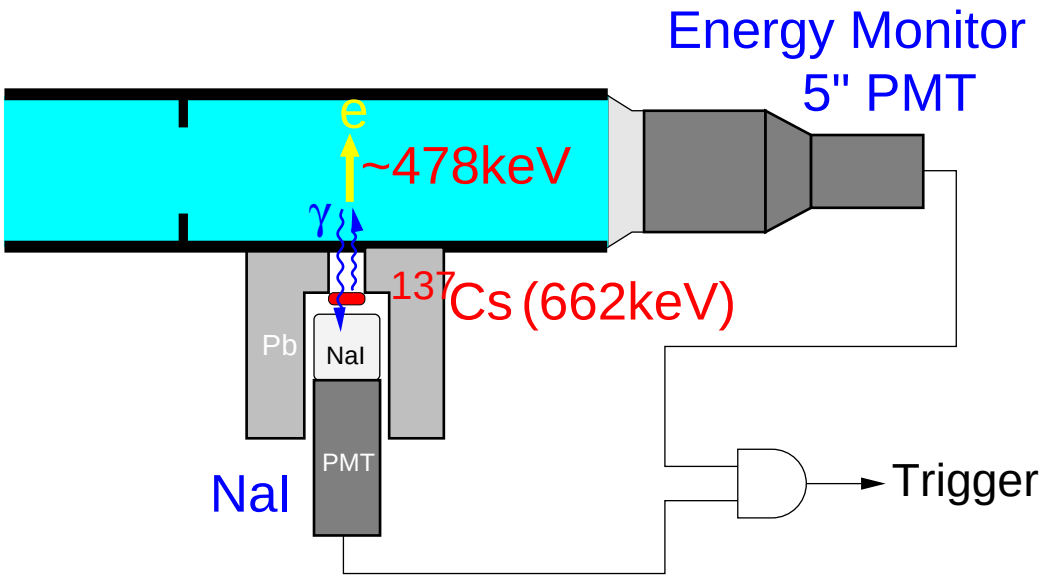

Figure 5.8: Setup for energy calibration. The energy monitor detects the scintillation light which derived from the scatter electron, and NaI counter detects the back-scattered gamma-ray. The event trigger is created from the coincidence of these two signal.

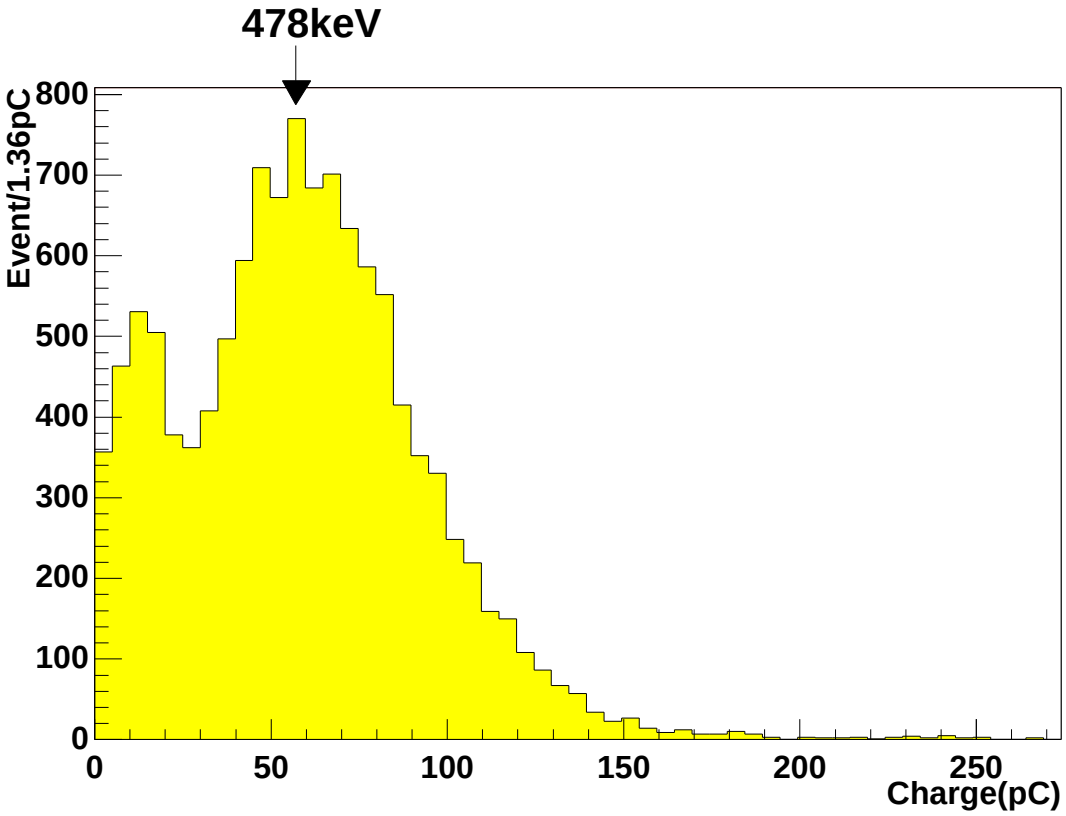

Figure 5.9: ADC charge of the energy monitor when the distance between the energy monitor and ^{137}Cs is about 13cm. The peack is denotes the 478keV.

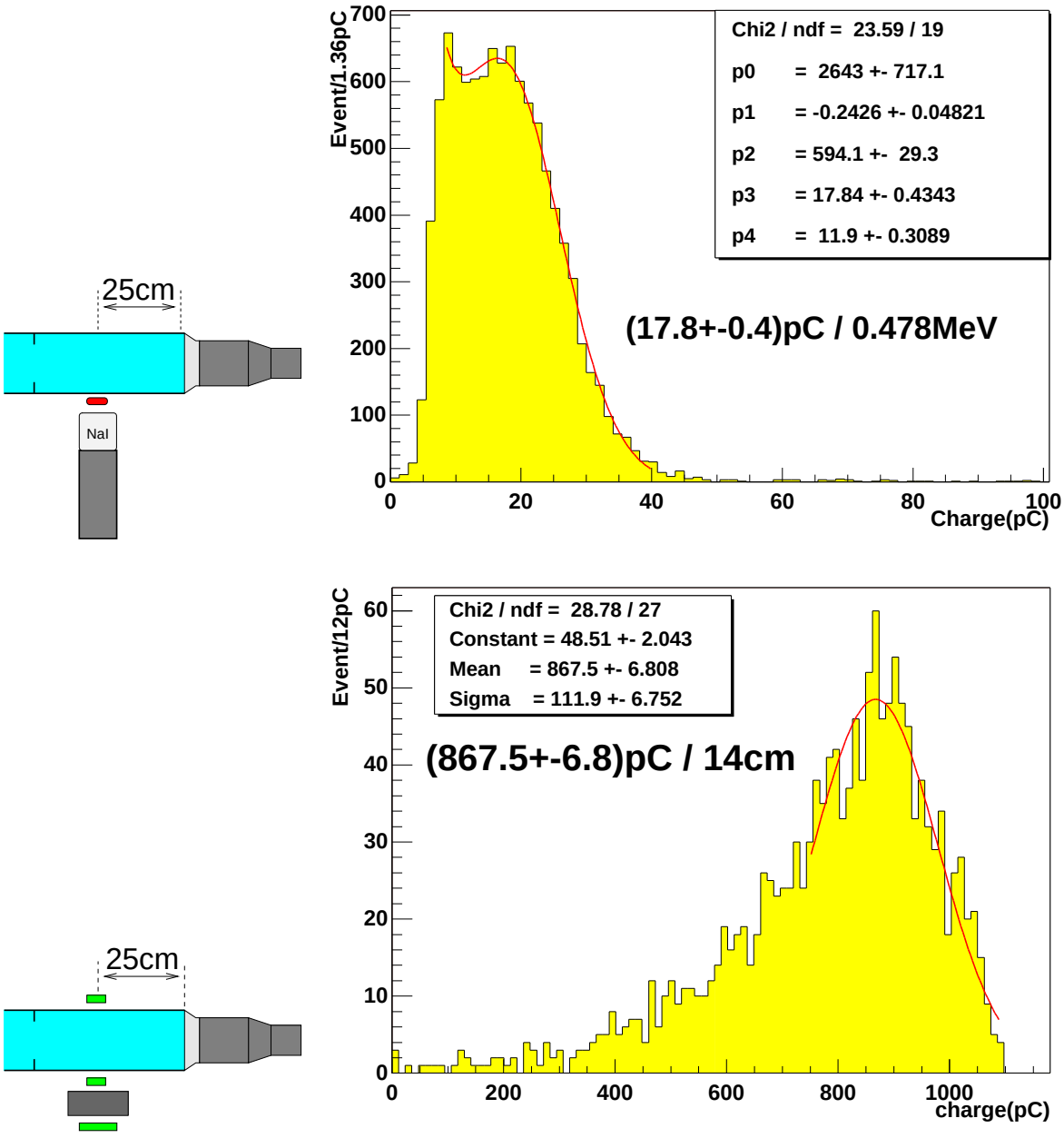

Figure 5.10: Total charges of the energy monitor when the distance between this monitor and ^{137}Cs, trigger counter is 25cm.

5.7 Discussion

From the results of the light yield and the energy calibration, the light yield of KamLAND detector can be estimated using following parameters.

- Number of PMT = 1,295(17"PMT), 580(20"PMT)
- Transparency of Balloon = 94% @360nm
- Transparency of Acryl which used in the long scintillator system = 85% @360nm
- 17"PMT light collection efficiency 85%
- 5"PMT collection efficiency 64%

The estimated light yield of KamLAND(@center) is ∼190p.e./MeV(Th.=1/4p.e.). This is corresponding to

$$\frac{\delta \mathrm{E}}{\mathrm{E}} = \frac{7}{\sqrt{E(\mathrm{MeV})}} \quad \% \quad (@\mathrm{center})$$

The actual number of p.e. is expected to be higher than this number because that this measurement is insensitive to the light re-scattering and that higher p.e. number is expected for the peripheral events than central events.

5.8 Summary

The light yield were measured using the long apparatus(∼KamLAND scintillator vessel). From the measurement results, the normal-paraffin(N12) turned out to be better than iso-paraffin(P250), and the best concentration of PPO is 1.5g/l. Moreover, using the energy calibration and a several parameters, the light yield of KamLAND(@center) is estimated to be 190p.e./MeV(Th.=1/4p.e.).

Chapter 6

Summary

KamLAND is the very large-size detector to observe low energy anti-neutrino and neutrino. Volume of liquid scintillator which is one of the main component in the detector is 1,300m^3, and radius of the scintillator vessel is 6.5m. Almost all $\bar{\nu}_e$ come from nuclear reactors and terrestrial, and their visible energy are above 1MeV. On the other hand, many ν_e come from the Sun, and the energy of the solar neutrino, especially ^{7}Be neutrino, is 862keV. In order to study on various physics through the detection of these neutrino, several features are required for the scintillator.

- Light Yield $\geq$ 100 p.e./MeV($\delta E/E = 10\%/\sqrt{E(MeV)}$)
- MissID(α, fast neutron $\leftrightarrow \beta, \gamma$) $\leq$ 10 %
- High Flash Point($>$ 60 °C) for safty
- Very low contamination of natural radioactivities

Low energy threshold give high statistics of the solar neutrino, and the lower limit is decided by contamination of ^{14}C(Q_β = 157 keV) β-decay. This contamination can be suppressed by the high energy resolution, and the energy resolution is depends on the light yield(number of detected photon). When the light yield 100 p.e./MeV, the lower limit of the threshold will be 280 keV. Low background condition is also important feature, and Pulse Shape Discrimination(PSD) is effective technique for the background suppression. MissID is the probability to recognize α or fast neutron events as β or γ events.

Generally, the liquid scintillator consists of solvents, primary solute and wavelength shifter(secondary solute). We selected Pseudocumen(1,2,4-Trimethyl Benzene) as a solvent, PPO as a primary solute and BisMSB as a wavelength shifter because many experiments have used. The light yield depends on the light output, light transparency,

surface coverage of PMTs and light sensitivity of PMT. KamLAND scintillator is diluted with the paraffin oil because the light transparency is the most important at the large size detector. The transparency of the paraffin oil is very good and its flash point (83°C) is much higher than that of pseudocumen(54°C). Therefore, the dilution, paraffin-oil/pseudocumen $>$ 70%/30%, also give the high flash point($>$ 60°C).

MissID(fast neutron $\leftrightarrow$ γ) and light output measurements gave the concentration of pseudocumen and PPO. And these measurements results are no difference within 1% when BisMSB is added 0.1g/l in the scintillator. Here, the composition of the scintillator is squeezed;

Paraffin-oil(80%) + P.C.(20%) + PPO(1$\sim$2g/l)

or

Paraffin-oil(80%) + P.C.(20%) + PPO(1$\sim$2g/l) + BisMSB(0.1g/l)

We measured light attenuation lengths of above two scintillator(PPO=2g/l), and calculated light yield using various parameters, attenuation-lengths, light-output, surface coverage of PMTs, light sensitivity of PMT and transparency of the scintillator vessel(Chapter4). Calculated light yields are almost same(average 180$\sim$200p.e./MeV), and there is also no difference adding BisMSB. Therefore, we decide that BisMSB or other wavelength shifter is unnecessary because of cost and no merit.

Additionally, we measured the light yield directly, for more detail study(Chapter5). We studied about paraffin oil types and PPO concentration.

- Paraffin oil dependence
  → There are two types paraffin oil, normalparaffin(N12) and isoparaffin(P250) as base liquid. N12-base scintillator is better(27%) than the P250-base one.

- PPO concentration(1-2g/l) dependence
  → The best concentration of PPO is 1.5g/l.

These studies gave the best components and concentration of the scintillator for KamLAND.

Normalparaffin(N12)	+	Pseudocumen	+	PPO
80%		20%		1.5g/l

Moreover, the light yield of KamLAND(@center) is estimated about 190p.e./MeV(Th. = 1/4p.e.) using some parameters, the surface coverage of PMTs, transparencies of the scintillator vessel, collection efficiency of PMTs. This value corresponds to the energy

resolution,

$$\frac{\delta \mathrm{E}}{\mathrm{E}} = \frac{7}{\sqrt{E(\mathrm{MeV})}} \quad \% \quad (@\mathrm{center})$$

When the light yield is 190 p.e./MeV, we can below the trigger threshold to about 240keV. Additionally, background rate from ^{14}C will be much lower(1/460) than that at 100 p.e./MeV of light yield when energy threshold is 280 keV.

In summary, we develop the scintillator for KamLAND experiment based on the various measurements results. The composition of the scintillator and this features summarized in Table6.1.

Normalparaffin(N12) + Pseudocumen + PPO		
80%	20%	1.5g/l
light yield	190 p.e./MeV @ central event	
light output	49%Anthracene	
attenuation length	10 m @ 400 nm	
flash point	64°C	
density	0.78 g/cm^3	
refractive index	1.44	

Table 6.1: The composition and features of KamLAND scintillator.

Appendix A

Neutrino Oscillation

A.1 Vacuum Oscillation

If neutrinos have the mass, the theory up to the present have to be modified. For massive neutrinos, the flavor eigenstates, ν_e, ν_μ, ν_τ, are not the same as the mass eigenstates, ν_1, ν_2, ν_3, and its relation is written by the mixing matrix which is the same matrix as the CKM matrix for quarks.

$$|\nu_\alpha\rangle = U_{\alpha j}|\nu_\jmath\rangle \qquad (\alpha = e, \mu, \tau;\ \ j = 1, 2, 3) \tag{A.1}$$

From this relation, it is possible that one neutrino(ν_α) converts to another flavor(ν_β). This phenomenon is called neutrino oscillation. Time evolution of states obey the Shrödinger equation,

$$i\frac{d}{dt}|\nu_j\rangle = E_j|\nu_j\rangle \tag{A.2}$$

here E_j is the energy of ν_j, and the wave function can be written as

$$|\nu_j(t)\rangle = \mathrm{e}^{-iE_jt}|\nu_j(0)\rangle. \tag{A.3}$$

For flavor eigenstates, using Eq.A.1 and Eq.A.2, A.3,

$$i\frac{d}{dt}|\nu_\alpha\rangle = U_{\alpha j}E_jU^\dagger_{j\alpha}|\nu_\alpha\rangle \tag{A.4}$$

$$|\nu_\alpha(t)\rangle = U_{\alpha j}\mathrm{e}^{-iE_jt}U^\dagger_{j\alpha}|\nu_\alpha(0)\rangle. \tag{A.5}$$

If ν_α is produced at $t = 0$, the probability of detecting this neutrino at $t = t$ is

$$P(\nu_\alpha \to \nu_\alpha) = |\langle\nu_\alpha(t)|\nu_\alpha(0)\rangle|^2 \tag{A.6}$$

$$= \left|\langle\nu_\alpha(t)|U_{\alpha j}\mathrm{e}^{-iE_jt}U^\dagger_{j\alpha}|\nu_\alpha(0)\rangle\right|^2 \tag{A.7}$$

To simplify the problem, we consider only two flavors,

$$U = \begin{pmatrix} \cos\theta_V & \sin\theta_V \\ -\sin\theta_V & \cos\theta_V \end{pmatrix} \tag{A.8}$$

here θ_V is the mixing angle in vacuum between ν_e and ν_x. Flavor eigenstates are expressed as

$$|\nu_e\rangle = |\nu_1\rangle \cos\theta_V + |\nu_2\rangle \sin\theta_V \tag{A.9}$$

$$|\nu_x\rangle = -|\nu_1\rangle \sin\theta_V + |\nu_2\rangle \cos\theta_V \tag{A.10}$$

When time is t,

$$|\nu_e(t)\rangle = \cos\theta_V \mathrm{e}^{-iE_1 t}|\nu_1\rangle + \sin\theta_V \mathrm{e}^{-iE_2 t}|\nu_2\rangle \tag{A.11}$$

The mass of ν_1, ν_2 are m_1, m_2, respectively. The energy is

$$E_i = \sqrt{p^2 + m_i^2} \tag{A.12}$$

Therefore, the probability of $\nu_e \to \nu_e$ is

$$P_{\nu_e \to \nu_e}(t) = 1 - \sin^2 2\theta_V \sin^2\left(\frac{\Delta m^2 t}{4p}\right) \tag{A.13}$$

$$= 1 - \sin^2 2\theta_V \sin^2\left(\frac{1.27\Delta m^2[\mathrm{eV}^2] l[\mathrm{m}]}{4E[\mathrm{MeV}]}\right) \tag{A.14}$$

$$= 1 - \sin^2 2\theta_V \sin^2\left(\frac{\pi l}{L_V}\right) \tag{A.15}$$

here Δm^2 is the mass square difference between ν_1 and $\nu_2 (\Delta m^2 = \left|m_2^2 - m_1^2\right|)$, l is the propagation length in the time interval of t, and L_V is the oscillation length in vacuum which is defined as

$$L_V \equiv \frac{4\pi E}{\Delta m^2} \tag{A.16}$$

For $\bar{\nu_e} \to \bar{\nu_e}$, these can be written similar expression.

From above equations, it is clear that $P_{\nu_e \to \nu_e}(t) < 1$, so the number of observed $\nu_e(\bar{\nu_e})$ events are less than that of generated $\nu_e(\bar{\nu_e})$ events if $\nu_e(\bar{\nu_e})$ and $\nu_x(\bar{\nu_x})$ have finite different masses and there is a non-zero mixing angle between them.

On the other hand, the Shrödinger equation for two generation is

$$
\begin{aligned}
i\frac{d}{dt}\begin{pmatrix}\nu_e\\ \nu_x\end{pmatrix} &= U\begin{pmatrix}E_1 & 0\\ 0 & E_2\end{pmatrix}U^\dagger\begin{pmatrix}\nu_e\\ \nu_x\end{pmatrix} && \text{(A.17)}\\
&= \left[\frac{E_1+E_2}{2}\begin{pmatrix}1 & 0\\ 0 & 1\end{pmatrix} + \frac{E_2-E_1}{2}\begin{pmatrix}-\cos 2\theta_V & \sin 2\theta_V\\ \sin 2\theta_V & \cos 2\theta_V\end{pmatrix}\right]\begin{pmatrix}\nu_e\\ \nu_x\end{pmatrix} && \text{(A.18)}\\
&= \left[\frac{E_1+E_2}{2}\begin{pmatrix}1 & 0\\ 0 & 1\end{pmatrix} + \frac{\pi}{L_V}\begin{pmatrix}-\cos 2\theta_V & \sin 2\theta_V\\ \sin 2\theta_V & \cos 2\theta_V\end{pmatrix}\right]\begin{pmatrix}\nu_e\\ \nu_x\end{pmatrix} && \text{(A.19)}\\
&\equiv \left(\hat{H}_0+\hat{H}_V\right)\begin{pmatrix}\nu_e\\ \nu_x\end{pmatrix} && \text{(A.20)}
\end{aligned}
$$

here $\hat{H}_V$ is

$$
\hat{H}_V\begin{pmatrix}\nu_e\\ \nu_x\end{pmatrix} \equiv \frac{\pi}{L_V}\begin{pmatrix}-\cos 2\theta_V & \sin 2\theta_V\\ \sin 2\theta_V & \cos 2\theta_V\end{pmatrix}\begin{pmatrix}\nu_e\\ \nu_x\end{pmatrix} \qquad \text{(A.21)}
$$

This hamiltonian $\hat{H}_V$ is derived from the Vacuum Oscillation.

A.2 Neutrino Oscillation in the Matter(MSW Effect)

A.2.1 General Equations of the MSW Effect

Neutrino oscillations in matter was first proposed by S.P.Mikheyev and A.Yu.Smirnov based on the theory advocated by L.Wolfenstein. Therefore, that is often called the MSW effect.

When neutrino propagate through the matter, ν_e and ν_μ(or ν_τ) feel different potentials because ν_e scatters off electrons via both neutral and charged currents, whereas $\nu_\mu(\nu_\tau)$ scatters only via the neutral current(FigureA.1). The electron neutrino receives an extra contribution of $\sqrt{2}G_F n_e$which derived from the charged current interaction, here n_e is the electron number density in the matter.

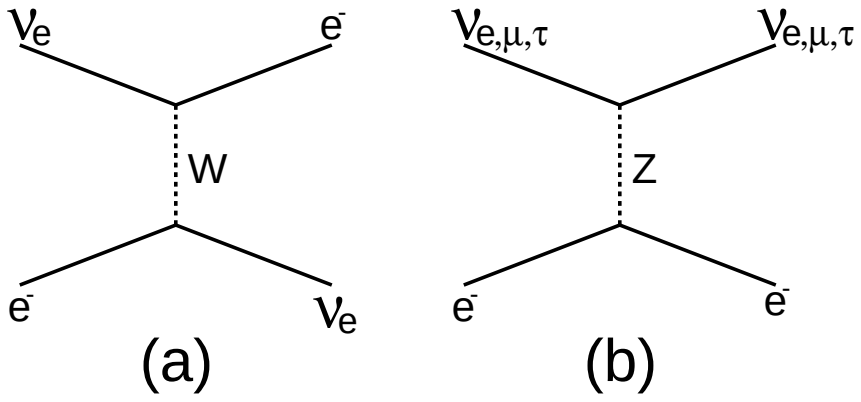

Figure A.1: Feynman diagrams of the neutrino scattering with electron, (a) is a charged current interaction of ν_e, and (b) is a neutral current interaction of ν_e, ν_μ, ν_τ.

From these effective potentials, the hamiltonian in the matter($\hat{H_M}$) is written as

$$\hat{H}_M \begin{pmatrix} \nu_e \\ \nu_x \end{pmatrix} = \left(\hat{H}_0 + \hat{H}_V + \hat{H}_e + \hat{H}_{\mu,\tau}\right) \begin{pmatrix} \nu_e \\ \nu_x \end{pmatrix} \tag{A.22}$$

$$= \alpha \begin{pmatrix} 1 & 0 \\ 0 & 1 \end{pmatrix} \begin{pmatrix} \nu_e \\ \nu_x \end{pmatrix} \tag{A.23}$$

$$+\frac{\pi}{L_V} \begin{pmatrix} \frac{L_V}{\pi} \cdot \frac{G_F n_e}{\sqrt{2}} - \cos 2\theta_V & \sin 2\theta_V \\ \sin 2\theta_V & -\frac{L_V}{\pi} \cdot \frac{G_F n_e}{\sqrt{2}} + \cos 2\theta_V \end{pmatrix} \begin{pmatrix} \nu_e \\ \nu_x \end{pmatrix} \tag{A.24}$$

$$\equiv \alpha \begin{pmatrix} 1 & 0 \\ 0 & 1 \end{pmatrix} \begin{pmatrix} \nu_e \\ \nu_x \end{pmatrix} \tag{A.25}$$

$$+\frac{\pi}{L_V} \begin{pmatrix} \frac{L_V}{L_e} - \cos 2\theta_V & \sin 2\theta_V \\ \sin 2\theta_V & -\frac{L_V}{L_e} + \cos 2\theta_V \end{pmatrix} \begin{pmatrix} \nu_e \\ \nu_x \end{pmatrix}, \tag{A.26}$$

here the first term is a common phase[1] , and L_e is the neutrino-electron interaction length which is defined as

$$L_e = \frac{\sqrt{2}\pi}{G_F n_e} \tag{A.27}$$

Now, we define that the oscillation length and the mixing angle in matter are L_M and θ_M, respectively.

$$\frac{\pi}{L_M}\begin{pmatrix} -\cos 2\theta_M & \sin 2\theta_M \\ \sin 2\theta_M & \cos 2\theta_M \end{pmatrix} \equiv \frac{\pi}{L_V}\begin{pmatrix} \frac{L_V}{L_e} - \cos 2\theta_V & \sin 2\theta_V \\ \sin 2\theta_V & -\frac{L_V}{L_e} + \cos 2\theta_V \end{pmatrix} \tag{A.28}$$

From $|\textit{left side}| = |\textit{right side}|$ at the above equation, L_M, and $\sin^2 2\theta_M$ are written as

$$L_M \equiv \frac{L_V}{\sqrt{\sin^2 2\theta_V + \left(\frac{L_V}{L_e} - \cos 2\theta_V\right)^2}} \tag{A.29}$$

$$\sin^2 2\theta_M \equiv \frac{\sin^2 \theta_V}{\sin^2 2\theta_V + \left(\frac{L_V}{L_e} - \cos^2 2\theta_V\right)^2} \tag{A.30}$$

From the above equations, we can know that the mixing angle in the matter, θ_M, is larger as the electron number density, n_e, is larger (TableA.1). Here, $n_e^{resonance}$ is called "MSW Resonance Density", and the oscillation is maximum("Resonance Condition") at that density.

$$\frac{L_V}{L_e} = \cos 2\theta_V \tag{A.31}$$

$$n_e^{resonance} = \frac{\Delta m^2}{2\sqrt{2}G_F E}\cos 2\theta_V \tag{A.32}$$

n_e	0	$\cdots$	$n_e^{resonace}$	$\cdots$	∞
θ_M	θ_V	$\cdots$	$\pi/4$	$\cdots$	$\pi/2$

Table A.1: The relation between the electron density and the mixing angle in the matter.

A.2.2 Neutrino Oscillation in the Sun

The flavor eigenstates in the matter are written as

$$|\nu_e\rangle = \cos\theta_M|\nu_1\rangle + \sin\theta_M|\nu_2\rangle \tag{A.33}$$

$$|\nu_x\rangle = -\sin\theta_M|\nu_1\rangle + \cos\theta_M|\nu_2\rangle \tag{A.34}$$

[1]A common phase can be omitted when we consider about the neutrino oscillation, because it doesn't influence on the oscillation.

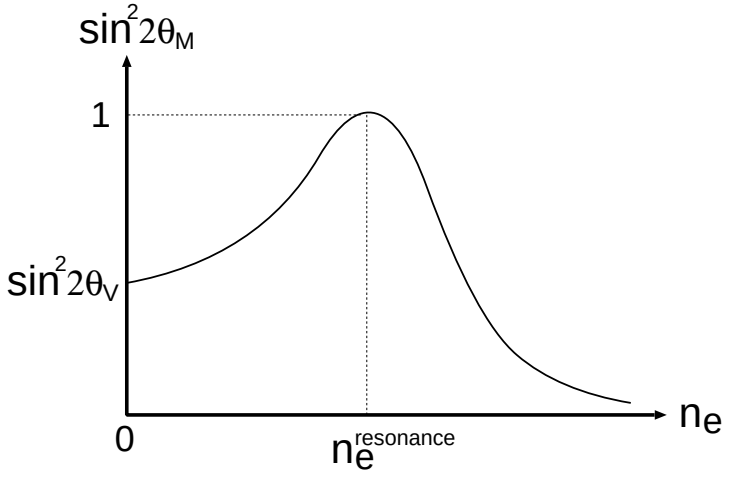

Figure A.2: The definition of the resonance condition and resonance density.

n_e	$\infty \longrightarrow 0$
$\langle \nu_e \vert \nu_2 \rangle$	$1 \longrightarrow \sin\theta_V$
$\langle \nu_x \vert \nu_2 \rangle$	$0 \longrightarrow \cos\theta_V$

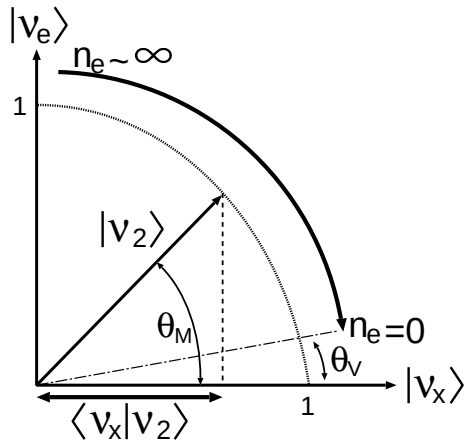

Figure A.3: As the electron density decreases slowly, the flavor eigenstate remains close to the mass eigenstate $|\nu_2\rangle$. Upon emerging from the Sun to an essentially vacuum environment, the original $|\nu_e\rangle$ is close to the vacuum flavor eigenstate $|\nu_x\rangle$.

The neutrino flavor which is created in the Sun is the electron neutrino, and the electron density at the center of the Sun is very high, $n_e \sim \infty \Rightarrow \theta_M \sim \pi/2$. Therefore, the neutrino which is created in the Sun is almost ν_2, and the flavor eigenstates of the solar neutrinos are written as

$$|\nu_e\rangle = \sin\theta_M |\nu_2\rangle \quad \text{(A.35)}$$

$$|\nu_x\rangle = \cos\theta_M |\nu_2\rangle \quad \text{(A.36)}$$

In the end, a part of the electron neutrinos which are created at the center of the Sun($n_e \sim \infty$) changes another flavor while it goes out from the Sun($n_e : \infty \rightarrow 0$).

FigureA.3 illustrates how a solar neutrino beam can change completely its flavor when the electron density varies slowly.

A.2.3 Regeneration in the Earth

Electron neutrinos which are converted to ν_x while passing through the Sun may be reconverted to ν_e on their way to a neutrino detector on the opposite side of the Earth from the Sun. If the MSW explanation is correct, electron neutrinos created in the Sun have had their flavor changed by matter interactions. Therefore, regeneration in the Earth will on the average produce more ν_e from ν_x rather than vice versa and may make the Sun appear to shine brighter in electron neutrinos at night(Day-Night effect).

Appendix B

Decay Chain of ^{238}U and ^{232}Th

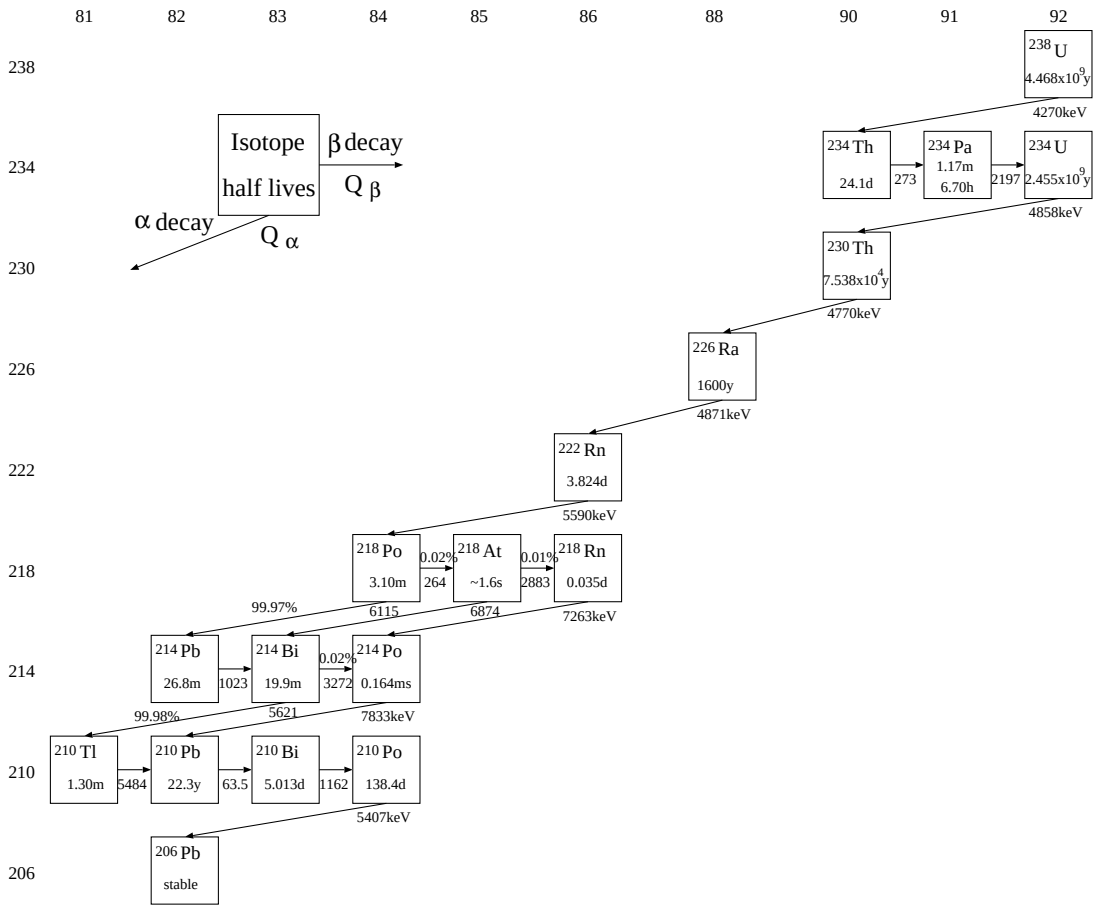

Figure B.1: Decay Tables of ^{238}U

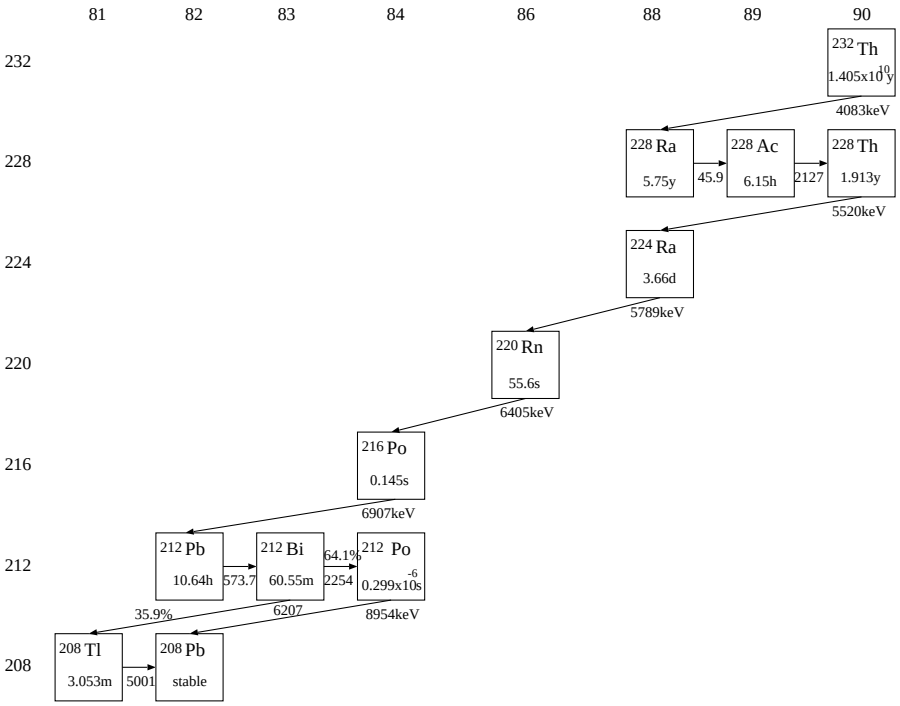

Figure B.2: Decay Tables of ^{232}Th.

	(keV)	(%)		(keV)	(%)		(keV)	(%)
^{238}U	E_α		^{226}Ra	E_α		^{214}Bi	E_γ	
(4.468×10^9y)	4220	20.9	(1600y)	4685	5.55		609	43.7
	4270	79.0		4871	94.45		665	1.45
	E_γ			E_γ			768	4.61
	50	20.9		186	5.55		934	2.94
^{234}Th	E_β		^{222}Rn	E_α			1120	14.9
(24.10d)	86	2.9	(3.824d)	5590	99.92		1155	1.65
	106	7.6	^{218}Po	E_α			1281	1.46
	107	19.2	(3.10m)	6115	99.979		1377	3.77
	199	70.3	^{214}Pb	E_β			1402	1.55
	E_γ		(26.8m)	184	2.35		1408	2.85
	30	5.66		489	1.04		1416	1.00
	63	4.89		671	46		1509	2.17
	92	19.1		727	40.5		1661	1.06
	93	2.79		1023	9.3		1730	2.90
	113	2.19		E_γ			1847	2.06
^{234}Pa	E_β			242	1.07		2119	1.17
(1.17m)	386	1.55		295	39.5		2204	4.86
(6.70h)	415	8		352	46.5	^{214}Po	E_α	
	435	2.8	^{214}Bi	E_β		(164μs)	7833	99.99
	460	1.14	(19.9m)	790	1.45	^{210}Tl	E_β	
	474	45.4		824	2.74	(1.30m)	1379	2
	503	7.0		1068	5.54		1604	7
	644	19.4		1153	4.14		1238	5.92
	1002	1.1		1255	2.9		1859	24
	1069	2.9		1261	1.66		2024	10
	1106	1.12		1277	1.38		2414	10
	1173	3.9		1382	1.59		4205	30
	1208	4.8		1425	8.26		4386	20
^{234}U	E_α			1508	16.9	^{210}Pb	E_β	
(2.455×10^9y)	4805	28.42		1542	17.5	(22.3y)	17	84
	4858	71.38		1729	3.05		64	16
	E_γ			1894	7.18		E_γ	
	53	28.42		3272	19.9		47	84
^{230}Th	E_α					^{210}Bi	E_β	
(7.538×10^4y)	4702	23.4				(5.013d)	1163	100
	4770	76.3				^{210}Po	E_α	
	E_γ					(138.4d)	5407	100
	68	23.4						

Table B.1: Decay chain of ^{238}U

Isotope	Energy (keV)	BR (%)	Isotope	Energy (keV)	BR (%)	Isotope	Energy (keV)	BR (%)
^{232}Th	E_α		^{228}Ac	E_γ		^{212}Pb	E_β	
(1.405×10^{10}y)	4018	22.1		58	74.1	(10.64h)	158	5.17
	4083	77.9		99	3.71		335	82.5
	E_γ			129	11.2		574	12.3
	64	22.1		209	4.05		E_γ	
^{228}Ra	E_β			270	4.43		239	82.6
(5.75y)	39	100		279	1.37		300	4.88
	E_γ			322	1.64	^{212}Bi	E_α	
	7	100		338	11.7	(60.55m)	6167	25.13
^{228}Ac	E_β			409	1.29		6207	9.75
(6.15h)	403	1.57		463	2.96		E_β	
	439	2.6		504	1.64		633	1.87
	444	1.18		509	1.37		741	1.43
	481	4.18		563	2.52		1527	4.36
	489	1.15		755	1.07		2254	55.46
	596	8.1		795	4.40		E_γ	
	959	3.54		836	1.49		40	25.6
	974	5.6		911	24.1		328	4.02
	1004	5.82		965	4.79		727	6.45
	1104	3.0		969	4.79		785	1.13
	1158	31.0		1631	1.97		1621	1.50
	1731	11.6	^{228}Th	E_α		^{212}Po	E_α	
	1940	1.9	(1.9131y)	5436	28.2	(299ns)	8954	100
	2069	10		5520	71.1	^{208}Tl	E_β	
				E_γ		(3.053m)	1040	3.09
				84	28.2		1292	24.5
			^{224}Ra	E_α			1526	21.8
			(3.66d)	5548	5.06		1803	48.7
				5789	94.94		E_γ	
				E_γ			277	2.66
				241	5.06		511	8.89
			^{220}Rn	E_α			583	30.0
			(55.6s)	6405	99.89		861	5.28
			^{216}Po	E_α			2616	35.3
			(0.145s)	6907	99.9981			

Table B.2: Decay chain of ^{232}Th

Appendix C

General Arguments of Liquid Scintillator

C.1 General Characteristics of the Scintillator

When radiation passes through the scintillator, it excites the atoms and molecules making up the scintillator causing light to be emitted. This light is detected by the PMT and so on, and converted to the electrical current signal. We get the physical information through the analysis of that signal.

In general, the scintillator signal is capable of providing a variety of information. Among its most outstanding features are:

1. **Sensitivity to Energy**
   Above a certain minimum energy, most scintillators behave in a near linear fashion with respect to the energy deposited, i.e., the light output of a scintillator is directly proportional to the exciting energy. If we use the detector whose electrical signal is proportional to this light(for example PMT), it makes the scintillator suitable as an energy spectrometer.

2. **Fast Time Response**
   Scintillation detectors are fast instruments in the sense that their response and recovery times are short relative to other types of detectors. This faster response allows timing information to be obtained with greater precision, for example, the time difference between two events. This and its fast recovery time also allow scintillation detectors to accept higher count rates since the dead time, i.e., the time that is lost while waiting for the scintillator to recover, is reduced.

3. **Pulse Shape Discrimination(PSD)** (Details in C.3.4)

With certain scintillators, it is possible to distinguish between different types of particles by analyzing the shape of the emitted light pulses. This is due to the excitation fo different fluorescence mechanisms by particles of different ionizing power. This technique is known as **Pulse-Shape Discrimenation(PSD)**.

C.2 Structure of the Liquid Scintillator

The liquid scintillator is consists of a few solvent and a few solute. The liquid scintillator is the organic liquid that the solute is dissolved in the solvent. The ionization energy seems to be absorbed mainly by the solvent and then passed on to the solute. This transfer usually occurs very quickly and efficiently.

- **Solvent**
  The solvent is the organic liquid, for example benzene, toluene, pseudocumene and so on. These liquids absorb radiation energy and then pass on to the phosphor(solute), so that the requirements for the good solvent are **high efficiency of the energy transition**, **not attenuate the scintillation light** and so on. Many solvents not only transit the energy to the solute but also emits the light from themselves, although it is very weak in comparison with that from the solute.

- **Solute(Phosphor)**
  Solute is the powdered phosphor, luminescence powder, for example PPO, PMP and so on. These materials which dissolved in the solvent convert the passed energy from the solvent to the light. Generally, the density of the solute is g/l order, and there are proper concentration for each solutes because of self-absorption(C.4).

- **Wavelength Shifter(Secondary solute)**
  The wavelength shifter absorbs the light which emitted by the above solute(primary solute) and emits the light whose wavelength is more longer than that from the primary solute. This solute is used if the light detector efficiency is not suitable for the wavelength region of the primary solute's emission. For example, Bis-MSB, POPOP etc. are well known wavelength shifter. These solute are called secondary solute against to the above primary solute.

The liquid scintillator is well known and used from long ago. But, the precise details of the energy transfer mechanism are still not clear, although there are a few models(references[18, 31, 33]).

C.3 Light Output Response

C.3.1 Time Response

When exposed to certain forms of energy, for example, light, heat, radiation and so on, the scintillator absorb and re-emit the energy in the form of visible light. If the reemission occurs immediately after absorption or more precisely within 10nsec., the process is usually called fluorescence. However, if reemission is delayed because the excited state metastable, the process is called phosphorescence or afterglow.

As a first approximation, the time evolution of the reemission process may be described as a simple exponential decay(FigureC.1).

$$N = \frac{N_0}{\tau_d} \exp\left(\frac{-t}{\tau_d}\right), \tag{C.1}$$

here N is the number of photons which emitted at time t, N_0 is the total number of photons between t=0 to t=∞, and τ_d the decay constant. The finite rise time from zero to the maximum in most materials is usually much more rapid than the decay time and has been taken as zero here for simplicity.

While this simple representation is adequate for most purposes, the real phenomenon is a more complex. A more accurate description, may be given by a two-component exponential

$$N = A \exp\left(\frac{-t}{\tau_f}\right) + B \exp\left(\frac{-t}{\tau_s}\right), \tag{C.2}$$

where τ_s and τ_f are the decay constants, $\tau_f < \tau_s$. For most scintillators, one component is generally much faster than the other so that it has become customary to refer to them as the **fast** and **slow** components, or the **prompt** and **delayed** components. Their relative magnitudes, A and B, vary from material to material, although it is the **fast** component which generally dominates(FigureC.1).

C.3.2 Response for Radiation

The light output of a scintillator refers more specifically to its efficiency for converting ionization energy to light. This is an extremely important quantity, as it determines the efficiency and resolution of the scintillator. In general the light output is different for different types of particles at the same energy(ionization quenching, C.4). Moreover, for a given particle type, it does not always vary linearly with energy. The efficiency that an average energy loss required for the creation of a photon decreases for heavier particles.

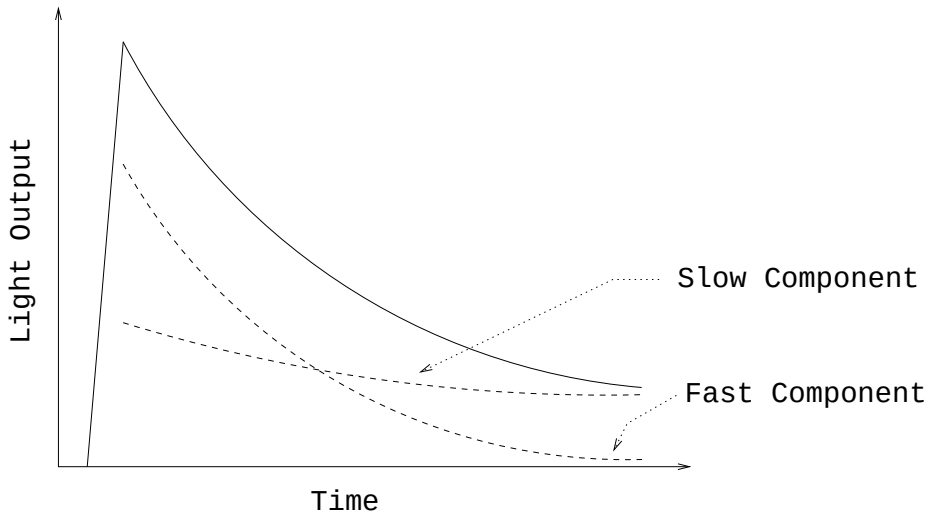

Figure C.1: Scintillation light is resolved into **fast(prompt)** and **slow(delayed)** components. The solid line represents the total light decay curve.

C.3.3 Linearity

The fluorescent light emitted, L, is directly proportional to the energy, E, deposited by the ionizing particle,

$$L \propto E. \tag{C.3}$$

Strictly speaking, this linear relation is not true, although for many applications it can be considered as a good approximation. In reality, the response of scintillators is a complex function of not only energy but the type of particle and its specific ionization. For example, in liquid scintillator, non-linearities are readily observed for electrons at energies below 125keV, although they are small.

C.3.4 Pulse Shape Discrimination(PSD)

In C.3.1, we mentioned that the emitted light has **fast component** and **slow component**. In general, both of these components depend on dE/dx to some degree or another. Therefore, the overall decay time of the emitted light pulse will vary with the type of exciting radiation. The scintillator is capable of distinguishing between different types of incident particle by the shape of the emitted light pulse(**Pulse Shape Discrimination**).

The explanation for this effect lies in the fact that the fast and slow components arise from the de-excitation of different states of the scintillator. Depending on dE/dx, these states are populated in different proportion, so that the relative intensities of

the two components are different for different dE/dx. A high dE/dx produces a high density of excited molecules which results in increased intermolecular interactions, so that de-excitation is high. In other words, the proportion of the fast component emitted relative to the slow component is reduced if dE/dx is high. In general, dE/dx of the heavy particle is higher than that of the light particle, so that the heavier particle has the smaller proportion of the fast component relative to slow component(FigureC.2).

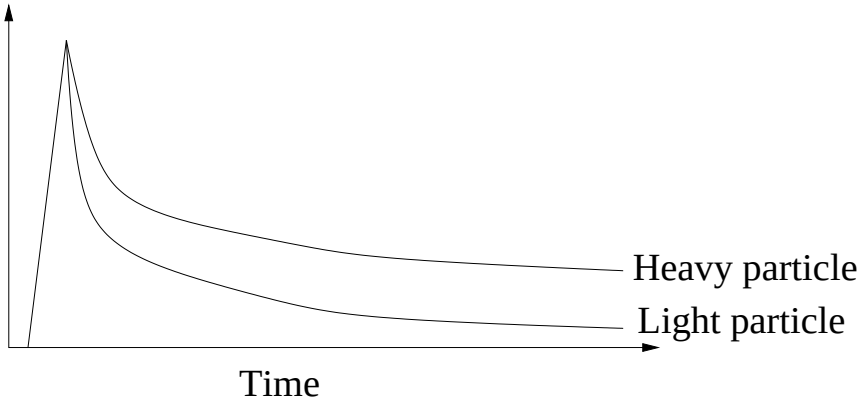

Figure C.2: The shape of the emitted light pulse is different if incident particle is different.

C.3.5 Temperature Dependence

The light output of most scintillators is also a function of the temperature. This dependence is generally weak at room temperatures, but should be considered if operation at temperatures very different from normal is desired. For example, in organic scintillators, the light output is practically independent of temperature between -60°C and +20°C and only drops to 95% of this value at +60°C.

C.4 Quenching

Quenching is the most important consideration when we use the scintillator. Quenching is the energy loss in the energy transition process, so that light output of scintillator is decrease. High energy physicists have to pay attention to next lines.

1. **Ionization Quenching**
   When a particle whose dE/dx is high pass through in the scintillator, the de-excitation of scintillator is higher than that when the other particle whose dE/dx is small pass through. In other words, the light output efficiency is different for different types of particles because their dE/dx is different.

2. **Oxygen Quenching**
   Dissolved oxygen in the liquid scintillator cause the quenching. The light output of the scintillator is rise if we can exclude oxygen in the scintillator. Nitrogen bubbling is the most useful method to exclude oxygen.

3. **Absorption of light(Color Quenching)**
   If there are materials whose absorption spectrum overlaps emission spectrum of the scintillator, the emission light is absorbed by these materials, so that detected light is decreased.

4. **Self-absorption**
   In all scintillator, a part of the absorption spectrum overlaps emission spectrum, so that the scintillator absorbs the light which it emitted(**self-absorption**) and emits the light again(FigureC.3). The effect of self-absorption is higher, the time and space resolution of the scintillation detector is worse.

5. Detector Efficiency
   If the overlap region of the quantum efficiency of the detector to the emission spectrum of the scintillator is poor, detected light is very poor. We must use the suitable detector for the scintillator. For example, PMT quantum efficiency spectrum is shown in FigureC.4.

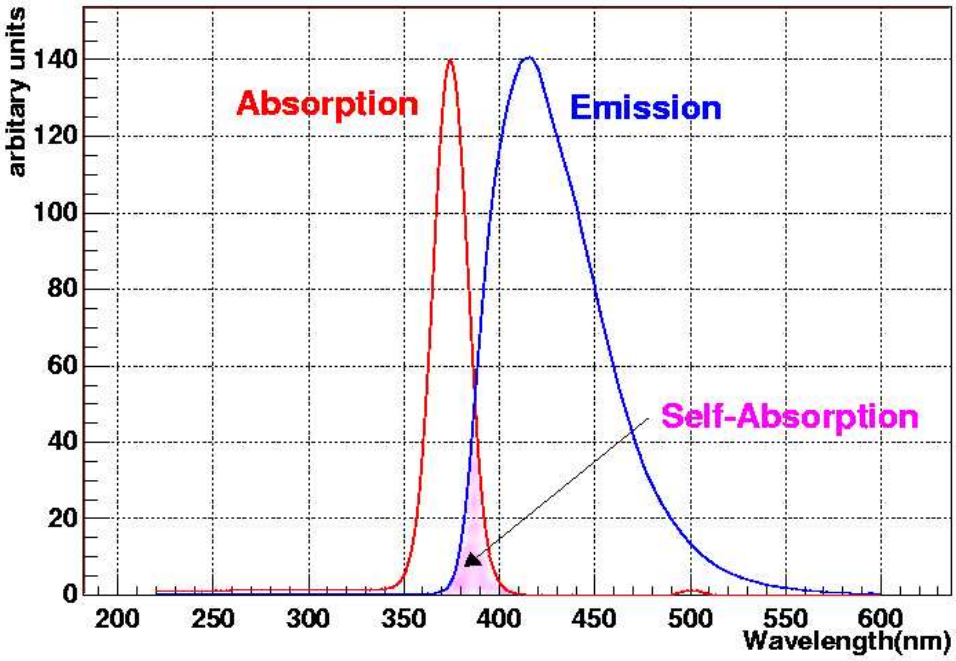

Figure C.3: Emission & Absorption spectrum of PMP(solute).

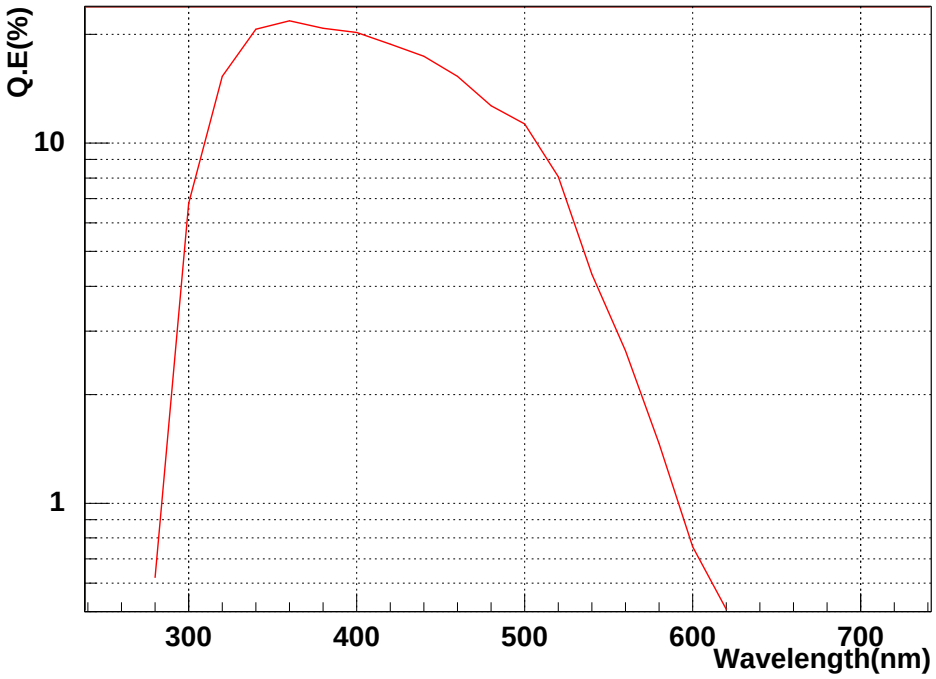

Figure C.4: Quantum Efficiency of PMT

Appendix D

Compton Scattering

The calucuration of the electron kinematic energy on Compton scattering.
From *momentum conservation*,

$$E_\gamma = E_\gamma^{'} \cos\phi + P_e \cos\theta \tag{D.1}$$

$$0 = P_e \sin\theta - E_\gamma \sin\phi \tag{D.2}$$

$$(\quad \because \quad E_\gamma = P_\gamma \leftarrow m_\gamma = 0 \ ) \tag{D.3}$$

Use above two equations,

$$P_e^2 = (E_\gamma - E_\gamma^{'} \cos\phi)^2 + (E_\gamma \sin\phi)^2 \tag{D.4}$$

$$= E_\gamma^2 + E_\gamma^{'2} - 2E_\gamma E_\gamma^{'} \cos\phi \tag{D.5}$$

From *Energy Conservation*,

$$E_\gamma + m_e = E_\gamma^{'} + E_e \quad (E_e = \sqrt{m_e^2 + P_e^2}) \tag{D.6}$$

$$\Rightarrow P_e^2 = (E_\gamma - E_\gamma^{;} + m_e)^2 - m_e^2 \tag{D.7}$$

$$= (E_\gamma - E_\gamma^{;})^2 + m_e(E_\gamma - E_\gamma^{;}) \tag{D.8}$$

From formulas (D.5) and (D.8),

$$E_\gamma^2 + E_\gamma^{'2} - 2E_\gamma E_\gamma^{'} \cos\phi = (E_\gamma - E_\gamma^{;})^2 + m_e(E_\gamma - E_\gamma^{;}) \tag{D.9}$$

$$E_\gamma - E_\gamma^{'} = \frac{E_\gamma E_\gamma^{'}}{m_e}(1 - \cos\phi) \tag{D.10}$$

$$= \frac{2E_\gamma E_\gamma^{'}}{m_e} \sin^2\frac{\phi}{2} \tag{D.11}$$

$$\therefore \quad T_e = \left(\frac{\frac{2E_\gamma}{m_e} \sin^2\frac{\phi}{2}}{1 + \frac{2E_\gamma}{m_e} \sin^2\frac{\phi}{2}} \right) E_\gamma \tag{D.12}$$

Here, T_e is *electron kinematic energy*. When γ-ray is back scattered(ϕ=180°), T_e is maximum.

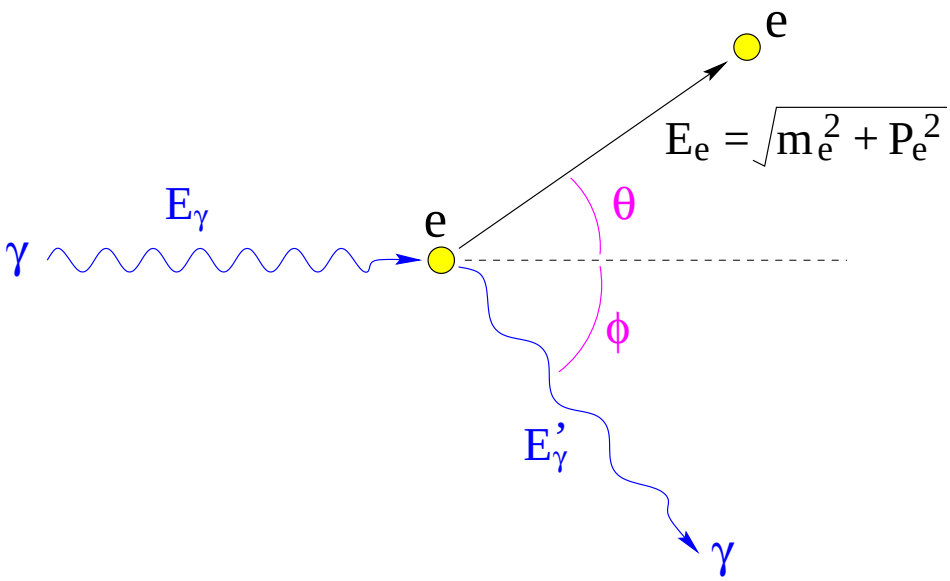

Figure D.1: Compton Scattering

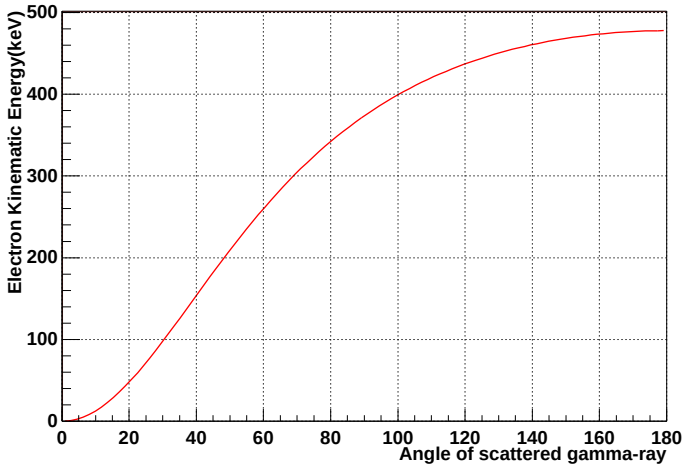

Figure D.2: The kinematic energy of Scattered electron v.s. The angle of scattered γ-ray. Here, E_γ=662keV(^{137}Cs)

Bibliography

[1] John N. Bahcall. *Neutrino Astrophysics*. Cambridge University Press, 1989.

[2] BOREXINO Collaboration. Addendum to the borexino proposals. 1996.

[3] CHOOZ Collaboration. Initial results from the chooz long baseline reactor neutrino oscillation experiment. *Physics Letter B*, Vol. 420, pp. 397–404, 1998.

[4] A.A.Hahn et al. Antineutrino spectra from ^{241}pu and ^{239}pu thermal neutron fission products. *Physics Letters*, Vol. B218, p. 365, 1989.

[5] Ch.Weinheimer et al. High precision measurement of the tritium beta-spectrum near its endpoint and upper limit on the neutrino mass. *Physics Letter*, Vol. B460, pp. 219–226, 1999.

[6] G.Zacek et al. Neutrino-oscillation experiments at the gosgen nuclear power reactor. *Physical Review*, Vol. D34, p. 2621, 1986.

[7] J.Busenitz et al. Proposal for us participation in kamland. proposal, KamLAND collaboration, 1999.

[8] KAMIOKANDE-II Collaboration (K. Hirata et al.). Bservation of a neutrino burst from the supernova sn1987a. *Physical Review Letters*, Vol. 58, pp. 1490–1493, 1987.

[9] K.Assamagan et al. Upper limit of the muon-neutrino mass and charged-pion mass from momentum analysis of a surface muon beam. *Physical Review*, Vol. D53, pp. 6065–6077, 1996.

[10] K.Hirata et al. *Physical Review*, Vol. D44, p. 2241, 1991.

[11] K.Schreckenback et al. Determination of the antineutrino spectrum from ^{235}u thermal neutron fission products up to 9.5mev. *Physics Letters*, Vol. B160, p. 325, 1985.

[12] M.Fukugita et al. Limits on neutrino mass from cosmic structure formation. *hep-ph*, Vol. 9908450, , 1999.

[13] M.M.Lobashev et al. Direct search for mass of neutrino and anomaly in the tritium beta-spectrum. *Physics Letter*, Vol. B460, pp. 227–235, 1999.

[14] P.Fisher et al. Neutrino mass and oscillation. *hep-ph*, Vol. 9906244, , 1999.

[15] Y.Declais et al. Study of reactor anti-neutrino interaction with proton at bugey nuclear power plant. *Physics Letters B*, Vol. 338, pp. 383–389, 1994.

[16] Y.Fukuda et al. Evidence for oscillation of atmospheric neutrinos. *Physical Review Letters*, Vol. 81, pp. 1562–1567, 1998.

[17] Particle Data Group. Review of particle physics. *The European Physical Journal*, Vol. C3, , 1998.

[18] ISHIKAWA Hiroaki. 液体シンチレーション測定法. Nanzandoh, 1977.

[19] Glenn Horton-Smith. Muons, muon spallation, muon tracking, and spallation cut. KamLAND note 99-16, TOHOKU university High Energy Physics Group, 1999.

[20] M.H.Pinsonneault J.N.Bahcall, S.Basu. How uncertain are solar neutrino predictions? *Physics Letter*, Vol. B433, pp. 1–8, 1998.

[21] ISHIHARA Kenji. Study of $\nu_\mu \rightarrow \nu_\tau$ and $\nu_\mu \rightarrow \nu_{sterile}$ neutrino oscillations with the atmosperic neutrino data in super-kamiokande, 1998.

[22] TAGASHIRA Kenji. Cross section and event rate. KamLAND note 98-11, TOHOKU university High Energy Physics Group, 1998.

[23] A.Suzuki M.Fukugita, editor. *Physics and Astrophysics of Neutrinos*. Springer Verlag.

[24] Y. Nagashima. 高エネルギー物理学の発展. 朝倉書店, 1999.

[25] Y. Nagashima. 素粒子標準理論と実験的基礎. 朝倉書店, 1999.

[26] TAJIMA Osamu. Study on spectra of liquid scintillators for kamland. KamLAND note 97-05, TOHOKU university High Energy Physics Group, 1997.

[27] TAJIMA Osamu. A measurement of light attenuation-length of the kamland liquid scintillators. KamLAND note 98-17, TOHOKU university High Energy Physics Group, 1998.

[28] P.Vogel. Analysis of the anti-neutrino capture on protons. *Physcal Review D*, Vol. 29, pp. 1918–1922, 1984.

[29] ENOMOTO Sanshiro. Kamland実験のためのデータ収集システムの開発研究. Master's thesis, Tohoku univ., 1999.

[30] KAWAKAMI Satoko. 大深度地下実験室における環境放射能測定研究. Master's thesis, Tohoku univ., 1999.

[31] IWAMOTO Toshiyuki. Kamland実験における液体シンチレータの発光特性と粒子識別能力の評価. Master's thesis, Tohoku univ., 1998.

[32] IWAMOTO Toshiyuki. Measurements of alpha quenching factor for the kamland liquid scintillator. KamLAND note 99-01, TOHOKU university High Energy Physics Group, 1999.

[33] W.R.Leo. *Techniques for Nuclear and Particle Physics Experiments.* Springer Verlag.

[34] T. Yanagida. *Proceedings of the Workshop on Unified Theory and Baryon Number in the Universe.* KEK, Thukuba, Japan, 1979.

[35] Y.Suzuki. Solar neutrinos : talked at lepton photon international conference. 1999.

[36] Y.Totsuka Y.Suzuki, editor. *Neutrino Physics and Astrophysics, 293-298.* North Holland, 1999.